ISBN 978-82-326-3732-4 (printed version)
ISBN 978-82-326-3733-1 (electronic version)
ISSN 1503-8181

Doctoral Thesis
Carl Werdelin Bergan

Doctoral theses at NTNU, 2019:64

Carl Werdelin Bergan

Dynamic Loads on Francis Turbines

An Experimental Study

NTNU
Norwegian University of
Science and Technology
Faculty of Engineering
Department of Energy and Process Engineering

NTNU
Norwegian University of
Science and Technology

Doctoral theses at NTNU, 2019:64
NTNU

NTNU
Norwegian University of
Science and Technology

Carl Werdelin Bergan

Dynamic Loads on Francis Turbines

An Experimental Study

Thesis for the degree of Philosophiae Doctor

Trondheim, March 2019

Norwegian University of Science and Technology
Faculty of Engineering
Department of Energy and Process Engineering

NTNU
Norwegian University of
Science and Technology

NTNU
Norwegian University of Science and Technology

Thesis for the degree of Philosophiae Doctor

Faculty of Engineering
Department of Energy and Process Engineering

ISBN 978-82-326-3732-4 (printed version)
ISBN 978-82-326-3733-1 (electronic version)
ISSN 1503-8181

Doctoral theses at NTNU, 2019:64

Printed by Skipnes Kommunikasjon as

Til Ingrid

Preface

This work has been conducted at the Waterpower Laboratory, Department of Energy and Process Engineering at the Norwegian University of Science and Technology (NTNU) in Trondheim. The work is presented as a collection of papers written during the project period, August 2014 – October 2018. The work was originally funded by The Norwegian Hydropower Center, which is a collaboration between Norwegian educational institutions, industries and government.

Abstract

There is an increasing need for stable and flexible renewable energy. This calls for better lifetime predictions for Francis runners, which in turn requires more knowledge on the dynamic loads on the runner blades. This thesis outlines an experimental approach to further the understanding of the dynamic loads a Francis runner is subjected to, during off-design operation, transient operation, and during resonance conditions.

The objective of the thesis is to provide verification data for numerical analysis, as well as to quantify how the different operating regimes affect the lifetime of a Francis runner, through dynamic loads on the runner.

Experiments have been performed on a high head Francis model runner, both for deep part load (DPL), and for part load (PL) with a fully developed Rotating Vortex Rope. The measurements show that the DPL condition causes a large region of back flow, and the PL condition has high amplitudes of the Rehinegan's frequency. However, these effects are not significant when compared to the pressure amplitude at the runner blade inlet as a result of Rotor-Stator Interactions (RSI). A transient condition was examined, with the turbine undergoing load rejection from the Best Efficiency Point (BEP) to PL, and the RSI amplitude remained dominant at the turbine blades.

In order to investigate the RSI phenomena more closely, tests were conducted on a simplified runner blade (a hydrofoil with an asymmetric trailing edge), mounted in a square high-speed channel with 0° angle of attack. The tests show that the damping factor of the hydrofoil increases linearly, with a transition in the lock-in region. Particle Image Velocimetry (PIV) measurements showed that the vortex shedding of the hydrofoil exhibited large stream-wise fluctuations in velocity, likely due to wandering of the upper separation point. Further testing on a different

hydrofoil geometry reveal that the damping undergoes the same transition through lock-in, even when the vortex shedding amplitude is minimal. Additionally, the tests showed that the two hydrofoils exhibited the same slope in the damping factor change, when plotted against the reduced velocity, or the inverse Strouhal number. Computational Fluid Dynamics (CFD) matches the experimental data, and indicates that the trend continues up to at least $45\,\mathrm{m/s}$.

A multi-bladed cascade has been tested, for four modes of vibration, and the same transition through lock-in is observed. More interesting, the slope of the damping change coincides with the previously tested hydrofoils, in addition to conforming with the slopes of hydrofoils tested in other works. This suggests that the product of added mass fraction and mode shape integral remains relatively unchanged for fixed-beam hydrofoils. This holds even for blades of differing natural frequencies (one order of magnitude in difference) and for multiple blades with modes coupled through water. The implication of this is that the analysis of a single blade can be extended to a runner, with predictable results.

Keywords: Hydraulic turbines, Francis turbine, Rotor-Stator Interactions, FSI, Pressure Pulsations, Vibration Measurements

Acknowledgements

I would like to extend my sincerest gratitude to my advisors, Ole Gunnar Dahlhaug and Torbjørn Nielsen. You have guided me in my work, heard my concerns when I needed help, and helped me along the way with lots of fruitful discussions. I think I can safely say that without you, this thesis would not have seen the light of day.

I would also like to thank my fellow PhD candidates and the post-docs at the Waterpower laboratory. You have contributed enormously to the social side of my PhD period, as well as being excellent discussion partners to bounce ideas with, to discuss and rediscover the theory that we all somehow forgot from our years as master's students, and to pass Friday evenings with crazy and nerdy projects.

I would also like to thank Michel Cervantes, who in addition to co-authoring papers with me, has served as a advisor for me, bringing in fresh new perspectives to the discussions.

I cannot stress enough how much of this work relies of the contributions of the technical staff at the Waterpower Laboratory:

Joar Grilstad, with you far-reaching expertise in instrumentation and electronics, you always have answers, even when Google comes short, you know how to solve the challenges

Trygve Opland, there is nothing you can't build, there is nothing you can't fix. You were essential for the manufacturing of the test rig that comprises more than half of this thesis, and you have been a continuing resource for support when I ran into challenges, both technical and practical

Halvor Haukvik, whenever there is something that needs to be done that I thought "who would know how to do that?", you always had the answers. You have a

suspiciously thorough knowledge of a surprisingly wide field, and that has been a great support for my work. Your attention to detail, while almost frustrating at times, has been a key feature in getting the measurements done.

I would like to thank PTM, with Åsmund Lerstad in particular, for their support in manufacturing the blade cascade test rig.

I would also like to thank Rainpower, for letting me use their equipment for my measurements.

I also want to thank Statkraft, for giving me a place to work from and finish my thesis, after I left the lab to move south.

I would like to thank my parents, they have been a constant support for me not only through my four years as a PhD candidate. You have nourished my curiosity, and I don't think I would have made it this far if you had not supported me in the way you have done.

Finally, I would like to thank Ingrid, for her patience. For her kindness. For her understanding.

List of Publications

■ This thesis is presented as a collection of papers. Three of the papers investigate how draft tube phenomena affect Franics turbines, while five of the papers deal with RSI and blade vibration.

1. **Bergan, C. W.**, Amiri, K., Cervantes, M. J, Dahlhaug, O. G., "Preliminary Measurements of the Radial Velocity in the Francis-99 Draft Tube Cone", 2012, *IOP Conference Series: Journal of Physics* ***579*** *012014*

2. **Bergan, C. W.**, Goyal, R., Cervantes, M. J., Dahlhaug, O. G., "Experimental Investigation of a High Head Model Francis Turbine During Steady-State Operation at Off-Design Conditions", 2016, *IOP Conf. Ser.: Earth Environ. Sci.* ***49*** *062018*, presented at *28th IAHR Symposium on Hydraulic Machinery and Systems*, Grenoble, France, September 22-26, 2016

3. **Goyal, R.**, Bergan, C. W., Cervantes, M. J., Gandhi, B. K., Dahlhaug, O. G., "Experimental Investigation on a High Head Model Francis Turbine during Load Rejection", 2016, *IOP Conf. Ser.: Earth Environ. Sci.,* ***49*** *082004*, presented at *28th IAHR Symposium on Hydraulic Machinery and Systems*, Grenoble, France, July 4-8, 2016

4. **Bergan, C. W.**, Solemslie, B. W., Østby, P., Dahlhaug, O. G., "Hydrodynamic Damping of a Fluttering Hydrofoil in High-speed Flows", 2018, *International Journal on Fluid Machinery and Systems*, **11**(2):146-153 (2018)

5. **Bergan, C. W.**, Tengs, E. O., Solemslie, B. W., Dahlhaug, O. G., "An Experimental Investigation of the Hydrodynamic Damping of Vibrating Hydrofoils", 2018, presented at *29th IAHR Symposium on Hydraulic Machinery and Systems*, Kyoto, Japan, September 15-20, 2018. Proceedings to be published

6. **Sagmo, K. F.**, Tengs, E. O., Bergan, C. W., and Storli, P. T., "PIV Measurements and CFD Simulations of a Hydrofoil at Lock-in", 2018, presented at *29th IAHR Symposium on Hydraulic Machinery and Systems*, Kyoto, Japan, September 15-20, 2018. Proceedings to be published

7. **Tengs, E. O.**, Bergan, C. W., Jakobsen, K-R., and Storli, P. T., "Numerical Simulation of the Hydrodynamic Damping of a Vibrating Hydrofoil", 2018, presented at *29th IAHR Symposium on Hydraulic Machinery and Systems*, Kyoto, Japan, September 15-20, 2018. Proceedings to be published

8. **Bergan, C. W.**, Tengs, E. O., Solemslie, B. W., Østby, P., Dahlhaug, O. G., "Damping Measurements on a Multi-Blade Cascade with Multiple Degrees of Freedom: a Francis-99 Test Case", 2019, *Submitted to IOP Conference Series: Journal of Physics*

Contents

List of Figures

List of Symbols

Abbreviations

BEP Best Efficiency Point

CFD Computational Fluid Dynamics

DPL Deep Part Load

FRF Frequency Response Function

FSI Fluid-Structure Interactions

HL High Load

MDOF Multiple Degrees of Freedom

NTNU Norwegian University of Science and Technology

PIV Particle Image Velocimetry

PL Part Load

RPM Revolutions Per Minute

RSI Rotor-Stator Interactions

RVR Rotating Vortex Rope

SDOF Single Degree of Freedom

Greek Symbols

α	Angle of rotation	$[^\circ]$
β	Turbine outlet angle	$[^\circ]$
Ω	Speed number	$[-]$
ω	Angular velocity	$[1/\mathrm{s}]$
Φ	Mode shape	$[-]$
σ	Stress	$[\mathrm{MPa}]$
ζ	Damping factor	$[-]$

Latin Symbols

a	Speed of sound in water	$[\mathrm{m/s}]$
c_d	Damping of dashpot	$[\mathrm{N\,s/m}]$
c	Water velocity, absolute	$[\mathrm{m/s}]$
D	Runner diameter	$[\mathrm{m}]$
F	Force	$[\mathrm{N}]$
f	Frequency	$[\mathrm{Hz}]$
H_t	Head	$[\mathrm{m}]$
H	Receptance FRF	$[\mathrm{m/N}]$
k	Spring stiffness	$[\mathrm{N/m}]$
L	Characteristic length	$[\mathrm{m}]$
M	Mobility FRF	$[\mathrm{m/(s\,N)}]$
m	Mass	$[\mathrm{kg}]$
N_{QE}	Specific speed	$[-]$
n	Runner rotational speed	$[1/\mathrm{min}]$
R	Pipe radius	$[\mathrm{m}]$

r	Radial position	$[\mathrm{m}]$
St	Strouhal number	$[-]$
S	Swirl number	$[-]$
t	Time	$[\mathrm{s}]$
u	Runner velocity	$[\mathrm{m/s}]$
v	Surface velocity	$[\mathrm{m/s}]$
w	Water velocity, relative	$[\mathrm{m/s}]$
x	Displacement	$[\mathrm{m}]$
z	Number of vanes	$[-]$
g	Gravitational acceleration	$[\mathrm{m/s^2}]$
N	Number of cycles	$[-]$
Q	Flow rate	$[\mathrm{m^3/s}]$

Indices, superscripts

*	Reduced

Indices, subscripts

B	Bulk
e	Excitation
g	Guide vane
m	Meridional
n	Natural
r	Runner
s	Impulse
u	Tangential

Embellishments, with x as example

$\bar{x}$	Mean value of x
$\Im(x)$	Imaginary part of x
$\|x\|$	Magnitude of x
$\Re(x)$	Real part of x
$\underline{x}$	Reduced value of x
$\dot{x}$	Time derivative of x
$\ddot{x}$	Double time derivative of x

Part I

Chapter I

Introduction

1.1 Motivation

In an ever-evolving energy market, there is an increasing need for renewable power with low regulation time. Increased pervasiveness of intermittent energy sources such as sun and wind power calls for an increase in governing on the power grid, in order to avoid significant fluctuations in voltage and grid frequency [1, 2, 3, 4]. In 2017, hydro power worldwide amounted to $1{,}114\,\mathrm{GW}$, but of newly installed renewable capacity, hydro power accounted for only $11\,\%$, with solar and wind power accounting for $84\,\%$ [5]. With the Paris agreement of 2016, along with more frequent extreme weather incidents, there is an increased pressure to reduce green house gas emission. At the same time, we must maintain stable and available electricity to a growing world population with increasing standards of living. With the price of both wind and solar power dropping dramatically [5], fraction of intermittent energy sources in the market is only expected to increase and it is therefore important to maintain grid regulation capabilities.

Hydro power is a mature technology with a remarkably short regulation time, in some cases at only a few seconds [6], significantly shorter than other available energy sources with the same installed capacity. When compared to other quickly-regulated sources of energy, hydro power emerges as a viable candidate for sustainable power regulation, with significant capacity already installed. However, an increased energy demand worldwide motivates the manufacturing of higher-efficiency turbines in existing power plants[7].

There are great opportunities in flexible operation of hydro power, such as the option to utilize pumped-storage to consume excess energy produced by wind turbines [8], or by operating power plants at off-design load in order to meet the

exact energy demand. At the same time, new challenges, in particular related to resonance, are emerging. In the new age of hydro power, the turbines are made thinner, which, while making them cheaper and more efficient, also leaves the runners more susceptible to high dynamic loads. Fatigue cracking has therefore emerged as a growing concern in new Francis runners [9]. In the last 15 years, several high head Francis runners have failed due to vibrations induced by resonance with the pressure field created by Rotor-Stator Interactions (RSI) [10].

In short, the new age of hydro power places two principal demands on the runners, both with the potential to severely reduce the runner's life time:

1. The turbines are increasingly being operated at off-design conditions, where the turbines are subjected to high cyclic loads.
2. The turbines are made thinner in order to achieve higher efficiency, making them more susceptible to damaging high-frequency loads due to RSI

Both of the conditions mentioned above can lead to increased dynamic loads on the turbine components, with damages ranging from blade fracture, to turbine failure[11].

1.2 Background

The phenomena occurring in a Francis turbine are of varying physical scales, ranging from large vortex structures in the draft tube cone [4, 12, 13, 14], to small acoustic phenomena occurring between the runner and stator blades [14, 15].

Take La Higuera, as an example: La Higuera is a power plant that commenced operation in 2010, and they experienced strong vibrations related to the Rotating Vortex Rope (RVR)[16]. This is a typical draft tube phenomena. On the other hand, several high head Francis runners have failed in the last 15 years due to RSI [10], a problem that is more typical for the distributor.

Due to the varying physical scales of these phenomena, they are difficult, if not impossible to accurately predict using structural simulations and Computational Fluid Dynamics (CFD) simulations. Hydraulic turbines are complicated machines, and to resolve the extent of the turbulent flow within the runner, the current technological limitations means that one would need a supercomputer for several months, and even then, the accuracy of the dynamic loads on the runner is not yet good enough to guarantee safe operation. In addition to this, the effects of Fluid-Structure Interactions (FSI) are notoriously difficult to capture accurately.

The traditional way to evaluate the results from a simulation, is to make comparisons with key features of a measurement performed at the same turbine. If enough of the parameters agree with reasonable margins, one can confidently evaluate the details of the simulations and discover interesting detail that are not readily available experimentally. The key premise here is experimental validation.

1.3 Objectives

This thesis will present an experimental investigation of the dynamic loads that a Francis turbine will be subjected to during on-design and off-design conditions. The experimental data serves as validation for CFD simulations.

The objective is to investigate and quantify the mechanisms that govern how dynamic loads on a Francis runner affect its performance and its lifetime. Additionally, this thesis will outline how the dynamic behavior of high head Francis runners can be estimated at an early stage.

1.4 Activities

In order to answer the objectives laid out in Section 1.3, experimental investigations will be carried out both on a model runner, and on a simplified turbine blade cascade. Pressure and velocity measurements in the model runner will investigate how the vortex structures contribute to dynamic loads on the runner. These measurements will also provide valuable verification data for numerical simulations. In the simplified turbine blade cascade, the natural frequency and damping of the simplified turbine blade (the hydrofoil) will be investigated in detail through vibration measurements and velocity measurements. These results will also provide verification data for numerical simulations.

Chapter II

Theoretical Background

■ This chapter presents the theory behind the main concepts that will be discussed in the paper summery, as well as in the papers.

2.1 A Francis turbine

Figure 2.1 shows a cutout model of a Francis turbine with the names for the main components indicated.

Turbines are typically characterized by reduced values. This is done to make comparisons between model and prototype runners.

The reduced flow rate, $\underline{Q}$, can be calculated by

$$\underline{Q} = \frac{Q}{\sqrt{2gH_t}} \tag{2.1}$$

Where Q is the flow rate at BEP, g is the acceleration due to gravity, and H_t is the turbine head at BEP.

Similarly, the reduced angular velocity, $\underline{\omega}$, is calculated by

$$\underline{\omega} = \frac{\omega}{\sqrt{2gH_t}} \tag{2.2}$$

where ω is the turbine's angular velocity.

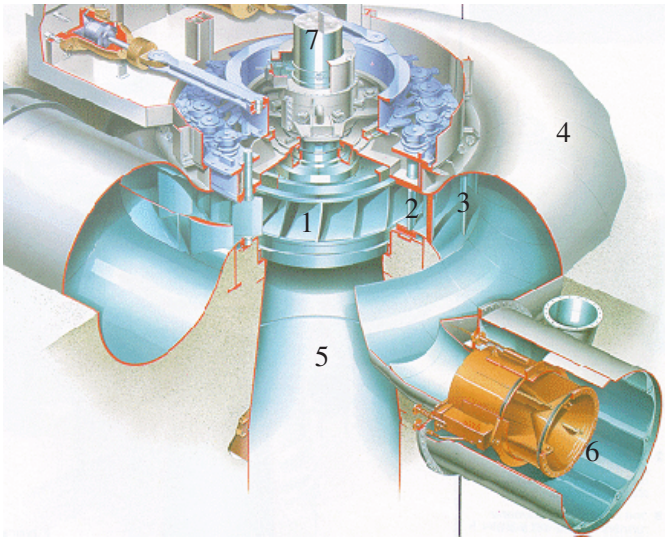

1. Runner
2. Guide vane
3. Stay vane
4. Spiral casing
5. Draft tube
6. Safety valve
7. Shaft

Figure 2.1: Anatomy of a typical Francis Turbine [17]

The terms from Equations (2.1) and (2.2) can be combined to obtain the speed number of the turbine:

$$\Omega = \underline{\omega}\sqrt{\underline{Q}} \tag{2.3}$$

Another widely used constant for classifying turbine runners is the specific speed, defined in IEC60193 [18] as

$$N_{QE} = \frac{n\sqrt{Q}}{(gH_t)^{3/4}} \tag{2.4}$$

The specific speed and the speed number only differ in scale. This is due to the use of revolutions per minute (RPM) in stead of angular velocity, as well as the omission of a factor of 2 in the term in the denominator in Equations (2.1) and (2.2). Both of these values are constant for two geometrically similar turbines of different scales. Their physical interpretation is that a turbine with a low specific speed (or speed number) is a turbine with a relatively high head and a low flow rate, for example a Pelton turbine, while a turbine with a relatively high specific speed (or speed number), is a turbine with a relatively high flow rate and a low head,

for example a Kaplan turbine. In the transition from low to high specific speed, Francis turbines are predominant.

2.2 Dynamic Loads on turbines

To understand how the dynamic loads on a Francis runner affect its lifetime, it is appropriate to review the basic dynamic phenomena that occur in a Francis turbine during operation.

2.2.1 Pressure pulsations

The term **pressure pulsations** refer to the unsteady cyclic pressures that occur within a turbine during operation. These pulsations can have different origins, and different types of pressure pulsations are typical for different types of turbines.

Swirling Flow and Rotating Vortex Rope

The flow in the draft tube cone of a Francis turbine is comprised of several different flow structures. The flow will exhibit some rotation, depending on the turbine's operating point, which can be seen from the velocity triangles of the turbine, shown in Figure 2.2.

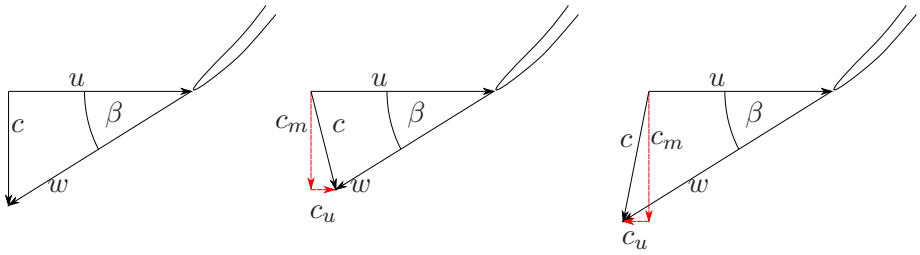

(a) Best Efficiency Point (b) Part load (c) Overload

Figure 2.2: Velocity triangles at the runner outlet for typical operating conditions. Note the tangential component, c_u, that appears when operating in HL and PL.

In Figure 2.2, c denotes the absolute velocity of the water, u denotes the peripheral velocity of the runner and w denotes water's relative velocity with respect to the runner. c_m and c_u denote meridional and tangential components, respectively. As shown in Figure 2.2, there will be a tangential velocity component in the flow when it exits the runner. While some rotation is beneficial for the pressure recovery in the draft tube wall, the tangential velocity component in the draft tube cone

is essentially unused energy, and anything beyond that small rotation needed to facilitate the pressure recovery, is wasted energy. If the tangential component—also known as the swirling component—of the draft tube flow becomes large, the flow in the draft tube cone may exhibit some interesting behaviours.

The **swirl number**, originally proposed by Chigier and Beér [19], and later modified by Sheen et al [20] is a measure of the ratio between swirling momentum and axial momentum. It is defined in Equation (2.5).

$$S = \frac{\int_0^R c_m c_u r^2 dr}{R \int_0^R {c_m}^2 r dr} \tag{2.5}$$

When examining axial flow with varying values for S, it is evident that a swirling velocity component has an adverse effect on the runner's performance. Figure 2.3 shows the expected axial velocity distributions in a swirling flow. Experiments confirm the velocity profiles up to $S = 0.7$ [21].

In Equation (2.5), This back flow is caused by the large pressure gradient towards the draft tube wall, which will force the water towards the center of the cone. From there, the adverse pressure gradient in the axial direction will force the water in the reverse direction. This core region with negative axial flow will effectively reduce the area through which the water can leave the turbine, leading to large velocity and pressure gradients, which incur hydraulic losses.

The swirling flow takes the form of two combined flow regimes: A free vortex on the outer periphery, combined with a solid-body rotation, or forced vortex, towards the center. This type of flow is called a **Rankine vortex**. The tangential velocity profile of a Rankine vortex is shown in Figure 2.4.

In a real flow, the transition from free vortex to solid-body rotation will be smoothed out by the viscous nature of the water. This is a region with high shear stresses, which gives rise to the **rotating vortex rope** (RVR).

For part load conditions, the rotation in the draft tube cone will be in the direction of the runner's rotation, as seen from Figure 2.2b. The transitional region from free vortex to solid-body rotation introduces shear stresses that form a rotating vortex rope. This vortex rope will travel around the region of back-flow, causing fluctuations in the back pressure for the runner. The frequency of this precession

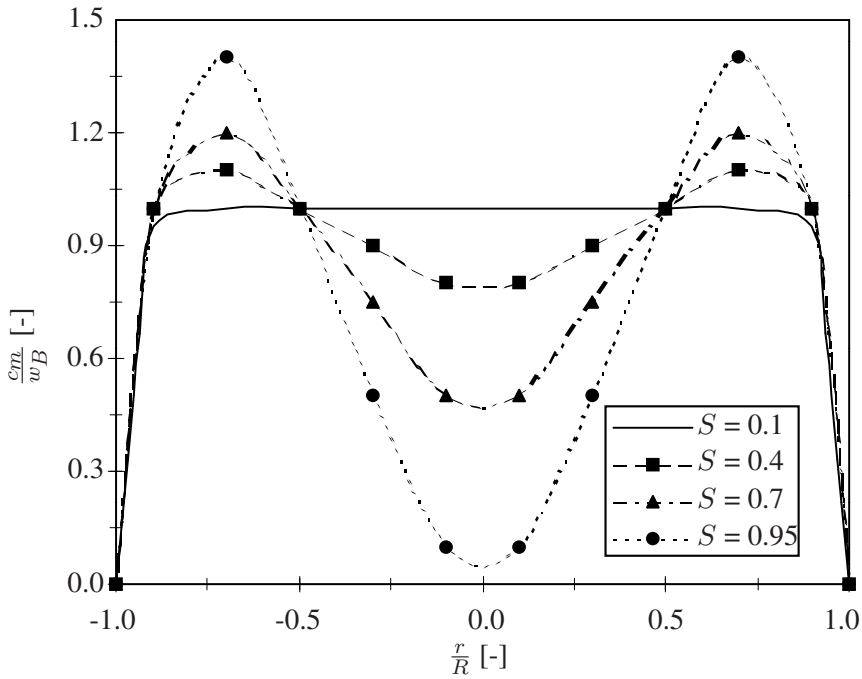

Figure 2.3: Axial velocity profiles for varying values of S [21]

is called the **Rheinegans frequency**, after W.J. Rheinegans, who in 1940 showed that power surges in the electric grid are associated with draft tube surges [22]. The Rheinegans frequency is approx. ⅓ of the runner rotational frequency. The pressure surges in the draft tube cone are comprised of a **rotating component**, i.e. the precession of the RVR, and a **plunging component**. These are commonly referred to as **synchronous** and **asynchronous**, respectively. The plunging component has a more severe impact on the back-pressure for the runner, as it is evenly distributed across the runner outlet. It is also more difficult to scale in frequency between models and prototype runners, as it is not dependent on the runners' rotational speed. The rotating and plunging components can be investigated independently with pressure measurements through the following procedure [23]:

$$A_R = \frac{S_1 - S_2}{2} \qquad (2.6) \qquad\qquad A_P = \frac{S_1 + S_2}{2} \qquad (2.7)$$

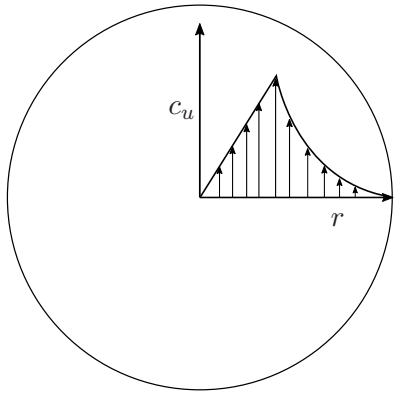

Figure 2.4: Tangential velocity profile of a Rankine vortex

In the context of Equations (2.6) and (2.7), A_R and A_P are the pressure amplitudes of the rotating and plunging components respectively, whereas S_1 and S_2 are two pressure sensors located $180\,^\circ$ apart.

RSI

The effects arising from rotors passing in close proximity to stators is called **Rotor-Stator Interactions**, RSI for short. For a Francis runner, RSI manifest as the runner blades travel through the unsteady pressure field generated by the guide vanes, inducing a pressure transient. Depending on the combination of runner blades and guide vanes, there will be any number of simultaneous pressure transients in the turbine. The simplest one to visualize occurs if the number of runner blades and guide vanes is equal, say 30 runner blades and 30 guide vanes. In that case, all runner blades and guide vanes will interact at the same time, creating one coinciding pressure pulse 30 times per revolution. This is effectively how old air-raid sirens were built, and it goes without saying that the vibrations from such a configuration are considerable.

In 1966, Oftebro and Lønning [24] showed that the combination of runner blades and guide vanes can cause constructive interference. When a runner blade passes a guide vane, a pressure pulse will occur. The next pressure pulse will occur when the runner has rotated an angle α, such that another runner vane aligns with a guide vane.

$$\alpha = 2\pi \left(\frac{1}{z_g} - \frac{1}{z_r} \right) \tag{2.8}$$

In the expression above, z_r is the number of runner blades, and z_g is the number of guide vanes. The time of such a rotation will be

$$t = \frac{2\pi(z_r - z_g)}{\omega_r z_g z_r} \tag{2.9}$$

where ω_r is the angular velocity of the runner. The pressure wave produced by this impulse will propagate at the speed of $a \pm w$—with a as the speed of sound in water, and w as the velocity of the water—and will reach the next impulse point after a time t_s.

$$t_s = \frac{\pi D}{(a \pm w) z_g} \tag{2.10}$$

In the worst case, if $t = t_s$, the pressure pulses add up, and a strong pressure oscillation is produced at the frequency, f, of

$$f = \frac{\omega_r z_r}{2\pi} \tag{2.11}$$

When considering the whole circumference, the cascade of impulses will be perceived as a travelling "impulse wave", which will cause the frequency expressed in Equation (2.12) when observed in the stationary domain.

$$f = \frac{\omega_r}{2\pi} z_r \tag{2.12}$$

Similarly, from a rotating domain, the observed frequency will be as expressed in Equation (2.13)

$$f = \frac{\omega_r}{2\pi} z_g \tag{2.13}$$

The frequency expressed in Equation (2.13) constitutes a constant excitation on the runner blades.

2.2.2 Von Kármán vortex shedding

Von Kármán Vortex shedding, often referred to simply as **vortex shedding**, is a flow instability in the wake of submerged blunt bodies. It is the shedding of

vortices in an oscillating manner, occurring due to unsteady flow separation near the trailing edge of the submerged body. The frequency of the vortex shedding is a function of the Reynolds number and the geometry of the submerged body. Vortex shedding can be observed on many scales, from cloud wakes around islands to small perturbations in the wakes of hydrofoils. Figures 2.5a and 2.5b show two examples of vortex shedding.

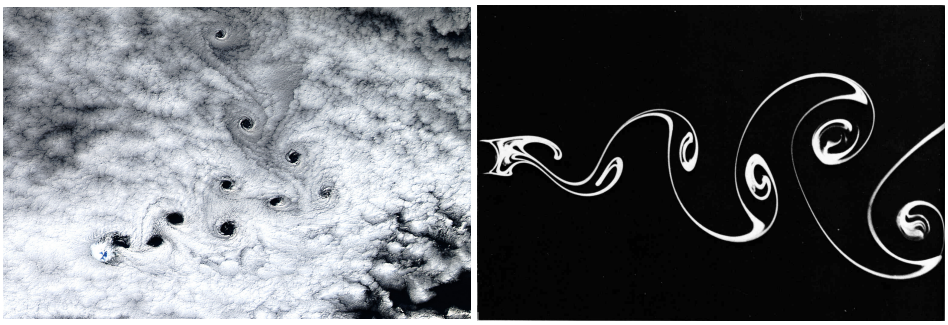

(a) Vortex shedding around the Mawson Peak (2,745 m) in the southern Indian Ocean [25]

(b) Vortex shedding around a cylinder of diameter 1 cm with water flowing at 1.4 cm/s[26]

Figure 2.5: Examples of vortex shedding on different scales

When dealing with oscillating flows, the **Strouhal number** is a relevant dimensionless term. It is defined as

$$St = \frac{fL}{w} \tag{2.14}$$

In Equation (2.14), L is known as the *characteristic length*, and can typically be the diameter of a cylinder, or the thickness of a hydrofoil's trailing edge.

The Strouhal number varies with high Reynolds number, but in a large range, it is fairly constant[27]. Equation (2.14) therefore implies that vortex shedding is dependent on the Reynolds number and consequently, flow velocity.

When the frequency of the vortex shedding is sufficiently close to the natural frequency of the object generating it, **lock-in** will occur.

Consider a cylinder of diameter D and length B. For low velocities, vortices will be shed along its length B at arbitrary phases. As the velocity increases, the frequency of the vortex shedding will increase. When the frequency of the vortex shedding approaches the natural frequency of the cylinder, the oscillation amplitude of the cylinder will increase, which will in turn affect the phase of the vortex shedding.

Subsequently, the phases of the vortex sheddings along the cylinders length will approach the phase of the moving cylinder, until they are all in phase, or "locked-in". This is a self-excitation mechanism, and the amplitude of this excitation can be quite considerable, often causing structures to vibrate audibly, or "sing". In fact, wires "singing" in the wind was the basis for the experiments performed in 1878 by Vincenc Strouhal [28]. If the velocity is further increased, the frequency of the vortex shedding remains at the cylinder's natural frequency for some range.

2.3 The effect of dynamic loads on materials

Although this thesis deals with the consequences of dynamic loads and fatigue, those topics are not the focus of the present work. As such, the following section is a brief summary of the basic concepts of material loading and fatigue, obtained from [29], and the interested reader is encouraged to study more detailed works for a more thorough explanation. In that regard, I recommend the book by William Callister [29].

2.3.1 Deformations and stress

When a material is subjected to a load, it will induce a mechanical stress, denoted by σ. The load will also deform the material, and for reasonable loads, the material deformation, called the strain, is proportional to the stress by a constant called **Young's modulus**. If the stress exceed what is called the **yield strength**, the material will deform permanently. This is typically called **material failure**.

2.3.2 Cyclic Stresses and Fatigue

Fatigue is a type of material failure that occurs in materials that are subjected to a combination of static and dynamic stresses. Fatigue is characterized by a sudden and rapid failure, and can clearly be identified by visual inspection of the breached surface. An example of fatigue failure on a steel shaft is shown in Figure 2.6.

Fatigue is of particular relevance to turbine components. Fatigue failure can occur for stress levels that are considerably lower than the material's yield strength, and is estimated to be the cause of approx. $90\,\%$ of all metallic failures. Figure 2.7 shows the nomenclature used in describing the cyclic stress on a material.

To investigate a material's response to fatigue, experiments are conducted on test samples. A sample is subjected to repeated cycles of a measurable stress, and the number of cycles, N, before failure, is plotted against the corresponding stress amplitude, S, and the S-N curve is produced. For some ferrous and titanium alloys,

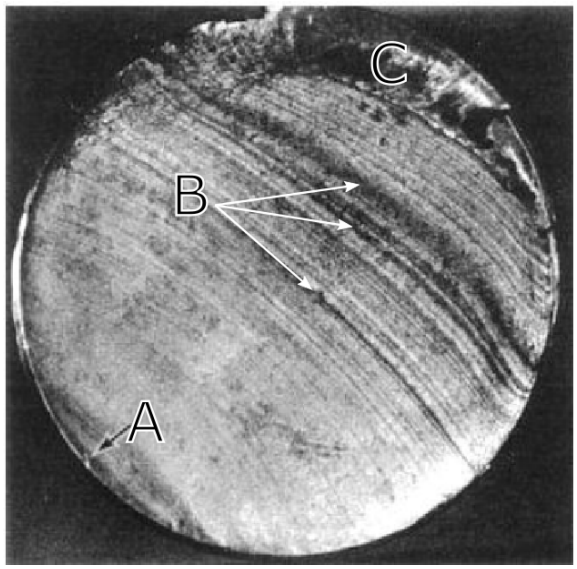

Figure 2.6: Fatigue fracture of a steel shaft [30]. Point A indicates the inception point of the fracture, while point B shows the crack growth lines. Point C is the area where the catastrophic failure occurred, a sudden plastic deformation.

the S-N curve becomes horizontal at high values for N, meaning that there is a limiting stress amplitude where fatigue will not occur. This is called the **fatigue limit**. For steel, the fatigue limit is in the range of 35 to 60 % of the yield strength. Most nonferrous alloys do not exhibit this horizontal behaviour of the S-N curve, and fatigue will therefore inevitably occur regardless of the stress amplitude. In that case, the **fatigue strength** is defined as the permissible stress amplitude for the material to last for a prescribed number of cycles. Conversely, if a predefined stress amplitude is applied, the S-N plot shows how many cycles can occur before the material fails, called the **fatigue life**. Such an S-N plot is shown in Figure 2.8

It should be mentioned that there is considerable uncertainty in such a curve. As such, one typically talks about material life in terms of probabilities. In addition to stress amplitude, the fatigue life is dependent on mean stress; If the mean stress increases, the fatigue life will decrease, even with the stress amplitude remaining constant.

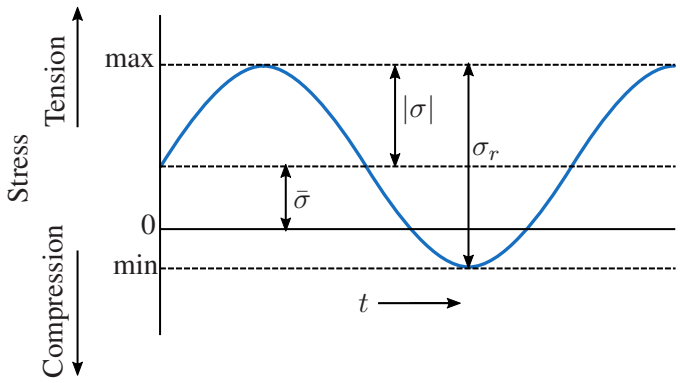

Figure 2.7: Cyclic Stress with annotation [29]. $\bar{\sigma}$ is the mean stress, $|\sigma|$ is the stress amplitude, and σ_r is the stress range

2.4 Experimental vibration analysis

This section will deal with the basics of a vibrating system and the mathematics in an ideal single-degree of freedom (SDOF) system. In addition to this, the basics of experimental vibrational analysis will be outlined, along with methods of modal parameter extraction. The assumptions in transitioning from an ideal to a physical system will also be explained. For a more in-depth course in modal analysis and vibration, the reader is referred to Ewins [31], and to Craig and Kurdila [32].

2.4.1 SDOF systems

A single degree of freedom (SDOF) vibrating system can be described as in Figure 2.9

Here, the mass of the vibrating system is given as m, the spring constant is k. The spring behaves in a way such that the force exerted on it is proportional to its compression, x, as such

$$F = kx \tag{2.15}$$

The dashpot behaves in a way such that the force exerted on it is proportional to its *rate of compression*, $\dot{x}$, as such

$$F = c_d\dot{x} \tag{2.16}$$

With Newton's second law of motion, the structure in Figure 2.9 will be governed by Equation (2.17).

$$m\ddot{x} + c_d\dot{x} + kx = F_e \tag{2.17}$$

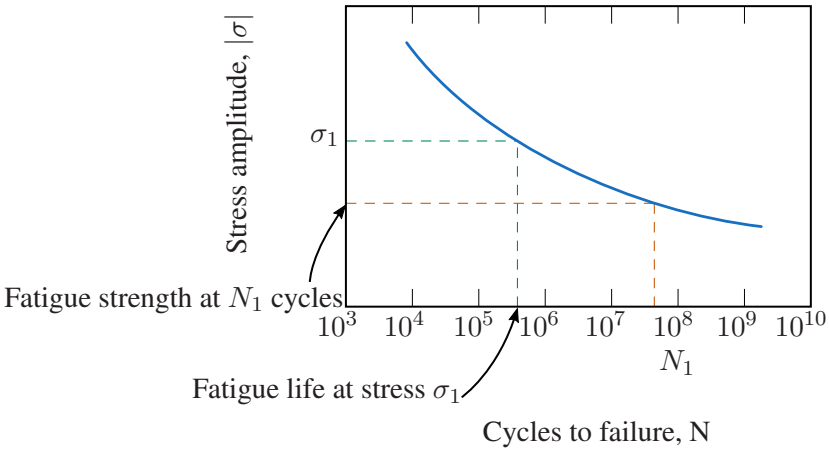

Figure 2.8: S-N curve for a non-ferrous alloy [29]. Note the difference between *fatigue life* and *fatigue strength*

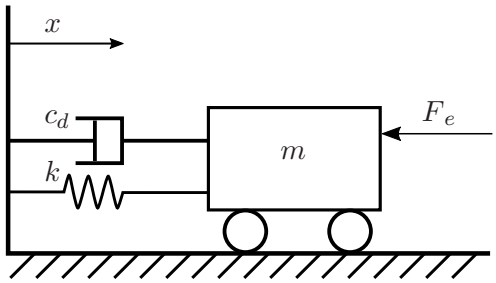

Figure 2.9: a SDOF-system

with $\ddot{x}$ as the acceleration.

Free vibration

For the case of *free vibration*, ie. $F_e = 0$, we assume that there exists a solution in the form of

$$x(t) = Xe^{st} \tag{2.18}$$

where s is a complex number. Equation (2.17) may then be rewritten as

$$\left(ms^2 + c_d s + k\right) = 0 \tag{2.19}$$

which has the two solutions, $s_{1,2}$:

$$\begin{aligned} s_{1,2} &= -\frac{c_d}{2m} \pm \frac{\sqrt{c_d^2 - 4km}}{2m} \\ &= -f_n\zeta \pm if_n\sqrt{1-\zeta^2} \end{aligned} \tag{2.20}$$

where

$$f_n{}^2 = \left(\frac{k}{m}\right) \quad ; \quad \zeta = \frac{c_d}{2\sqrt{km}} \tag{2.21}$$

In Equation (2.21), ζ and f_n denote the damping factor and the natural frequency respectively, and they are important parameters for each vibrational mode They will be at the center of some discussion in Chapter 4. A freely vibrating system with no external forces will vibrate at the frequency f_n and the vibrations will decay at a rate controlled by ζ.

Forced harmonic vibration

If we assume the excitation to be in the following form

$$F_e = Fe^{ift} \tag{2.22}$$

and the response to be in the following

$$x\left(t\right) = Xe^{ift} \tag{2.23}$$

Equation (2.17) can be rewritten as:

$$\left(-mf^2 + ifc_d + k\right) Xe^{ift} = Fe^{ift} \tag{2.24}$$

The **receptance** of the system, is then defined as the displacement per applied force:

$$H(f) = \frac{X}{F} = \frac{1}{\left(k - f^2m\right) + i\left(fc_d\right)} \tag{2.25}$$

By making substitutions from Equation (2.21), Equation (2.25) can be rewritten as the following

$$H(f) = \frac{1/k}{\left(1 - \left(\frac{f}{fn}\right)^2\right) + 2i\zeta\left(\frac{f}{fn}\right)} \tag{2.26}$$

If one considers the velocity per force, it is called the **mobility** and similarly, the acceleration per force is called the **accelerance**.

From Equation (2.23) we can differentiate to get the complex velocity given by:

$$v(t) = ifUe^{ift} \tag{2.27}$$

The *mobility FRF* will therefore have the form of

$$M(f) = if\frac{1/k}{\left(1 - \left(\frac{f}{fn}\right)^2\right) + 2i\zeta\left(\frac{f}{fn}\right)} \tag{2.28}$$

The expressions in Equation (2.28) is called the **frequency response function**, or FRF for the system. It contains phase- and amplitude information on how the system will respond to an external force.

Equation (2.25) can be extended to multiple degrees of freedom (MDOF) by repeating the analysis with x as a vector.

2.4.2 Damping estimation

The behavior of the damping factor, described in Equation (2.21), is central in Paper 4, Paper 5, Paper 7, and Paper 8. As such, a more detailed description on the estimation of damping factor from experimental data is provided here.

There are several available methods of damping estimation. The following section describes some of the more widely used ones. In the following methods, an underlying assumption is that the systems may be treated as SDOF systems. This does not mean that they only have a single degree of freedom, or that multiple modes do not exist, but it means that the modes are spaced widely enough apart to allow an investigation of a single mode without too much interference from neighbouring modes.

Half-power method

The Half-Power Method consists of amplitude measurements near resonance. This is a harmonic response method, not to be confused with the similarly named Half-Amplitude Method, which is a free decay method. In the Half-Power method, we assume that *all* the response at resonance is due to the local mode, and it is therefore only suitable for systems with widely separated modes. In the classic Half-Power Method, one considers two testing points in the vicinity of resonance. The procedure is as follows:

(a) Pick the response peak to consider, it's resonant frequency will be denoted f_n, and its amplitude $|H|$

(b) Find the two nearest frequencies around resonance where the magnitude of the FRF is reduced to $\frac{|H|}{\sqrt{2}}$, this is the *half power point*. Denote the frequencies f_a and f_b

(c) the damping can then be estimated by Equation (2.29)

$$\zeta = \frac{f_a^2 - f_b^2}{2{f_n}^2} \cong \frac{f_a - f_b}{2f_n} \tag{2.29}$$

Although the Half-Power method is simple to use, there are some caveats. First of all, it relies on precise magnitude measurements at resonance. The magnitude at resonance is highly sensitive to the amount of damping, and is therefore quite uncertain. Secondly, the contribution from neighbouring modes cannot be easily dismissed, even if they are widely spaced. This is due to the assumption that the mode of investigation is the sole contributor to the vibration, but even for widely spaced modes, this is rarely the case.

Circle-Fit Method

The Circle-Fit method is also known as method of Kennedy and Pancu [33]. In this method, the assumption is that the contribution of neighbouring modes is independent of frequency in the resonant region of the mode of interest. This assumption produces reliable results even with closely spaced neighbouring modes.

The method consists of plotting the real component of the FRF against its imaginary component. When plotting the receptance FRF in the complex plane, a vibrating system with structural damping will trace out a near-circular arc in a

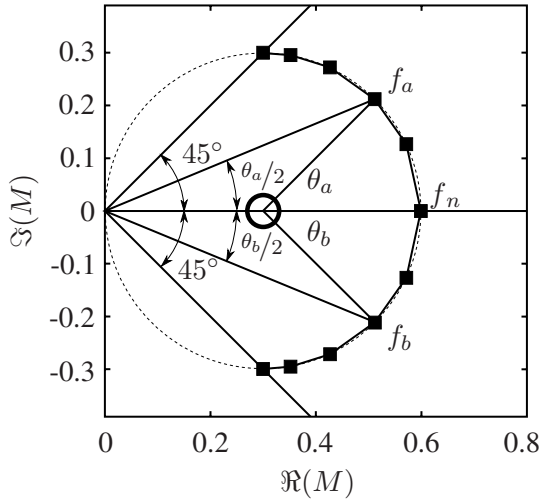

Figure 2.10: Circle fit in the Nyquist diagram. The black squares indicate measurement points.

resonant region. For a system with viscous damping, the mobility FRF will plot out as an exact circle. This type of plot is called a **Nyquist Plot**, and the Circle-Fit method often carries that name as well. The Nyquist plot for a lightly damped SDOF system is shown in Figure 2.10.

Based on the plot shown in Figure 2.10, some geometric properties may be examined. By selecting two angels, θ_a and θ_b on opposite sides of a resonance, the following is true:

$$\tan\frac{\theta}{2} = \frac{|\Im(M)|}{|\Re(M)|} \tag{2.30}$$

From Equation (2.28), we get

$$\tan\frac{\theta_a}{2} = \frac{1-r_a^2}{2\zeta r_a} \quad ; \quad \tan\frac{\theta_b}{2} = \frac{r_b^2-1}{2\zeta r_b} \tag{2.31}$$

with $r_a = \left(\frac{f_a}{f_n}\right)$ and $r_b = \left(\frac{f_b}{f_n}\right)$ for readability. Equation (2.31) can be rewritten as

$$2\zeta = \frac{r_b^2 - r_a^2}{r_a \tan\left(\theta_a/2\right) + r_b \tan\left(\theta_b/2\right)} \tag{2.32}$$

If points a and b are taken at equal frequency spacings around resonance, $r_a + r_b = 2$, the expression above can be simplified to

$$\zeta = \frac{f_b - f_a}{f_a \tan\left(\theta_a/2\right) + f_b \tan\left(\theta_b/2\right)} \tag{2.33}$$

Chapter III

Summary of Papers

■ This chapter presents a short summary of the papers of which this PhD thesis is comprised. The paper summaries also outline the evolution of the project.

Paper 1: *Preliminary Measurements of the Radial Velocity in the Francis-99 Draft Tube Cone*

Papers 1 and 2 deal with the velocity field in the wake of one particular Francis runner, dubbed the Francis-99 runner. In Paper 1, PIV measurements are performed in the draft tube cone's meridional plane, from which axial and radial velocity is obtained. The results show that the draft tube elbow in this particular turbine imposes a strong gyroscopic effect on the velocity profile exiting the runner. In addition, the measurements reveal a large region of negative flow for part load operation. This region of flow recirculation effectively reduces the cross-sectional area for the remaining flow rate through the turbine, and relatively high velocities are observed close to the draft tube wall.

My Contribution: I did the main portion of the writing, and was in charge of conducting the experiments, as well as performing the post-processing of the results.

Paper 2: *Experimental Investigation of a High-Head Model Francis Turbine During Steady-State Operation at Off-Design Conditions*

This paper is comprised of further PIV measurements in the Francis-99 runner

The results from this paper confirm that the flow leaving the runner is heavily asymmetric about the axis of rotation. In addition, the part-load operating point investigated in this paper has a much more pronounced Rotating Vortex Rope, in order to serve as validation for the Francis-99 CFD workshop.

My Contribution: I participated in the experimental setup and measurements, and had the main responsibility for Data Acquisition, in addition to having the main workload in the preparation of the manuscript.

Paper 3: *Experimental Investigation on a High Head Model Francis Turbine during Load Rejection*

This paper is comprised of PIV measurements in the Francis-99 runner for transient operation, moving from the Best Efficiency Point (BEP) to Part Load (PL). Synchronous pressure and velocity measurements were performed. It was observed that the development of the RVR starts in the plunging component, approx. $0.8\,\mathrm{s}$ before the rotating component, observable both in the decomposed pressure data and in the velocity data. The time signals for the rotating and plunging components were found using Equations (2.6) and (2.7). It was also found that the axial velocity only contributes to the plunging mode, and the radial velocity to the rotating mode.

My Contribution: I was responsible for the Data Acquisition, and participated in the experimental setup and measurements. I also participated in the data analysis and discussion of results, in addition to proofreading and reviewing the manuscript.

Paper 4: *Hydrodynamic Damping of a Fluttering Hydrofoil in High-Speed Flows*

This paper focuses on the vibration of a single turbine blade exposed to Rotor-Stator Interaction. A test blade is mounted in a square channel and exposed to flowing water with speeds up to $25\,\mathrm{m/s}$. Modal testing is performed on the blade throughout the velocity range of measurements, and the damping is found to depend on the water velocity. The damping estimates were done using the method described in Section 2.4.2. The results agree with previous findings on similar experimental setups. In addition, the damping behaved quite differently for water velocities below and above that of lock-in. Below lock-in velocity, the slope of the damping increase was very low, to the point that it can be argued that the

damping is more or less unchanged for flows below lock-in velocity. Above lock-in velocity, the slope of the damping increase was much steeper. Moreover, the natural frequency of the hydrofoil increased by $2.5\,\%$ through the lock-in region. The reasons for this are unclear.

My Contribution: I was responsible for the experimental setup and measurement campaign, in addition to the main workload of analyzing the data and preparing the manuscript.

Paper 5: *An Experimental Investigation of the Hydrodynamic Damping of Vibrating Hydrofoils*

This paper presents damping measurements preformed on two separate hydrofoil geometries, and comparisons are made with CFD. The hydrofoils are tested for water velocities up to $28\,\mathrm{m/s}$, and the observed trend is similar to that observed in Paper 3. One of the hydrofoils, F0, had an asymmetric trailing edge with heavy vortex shedding, while the other hydrofoil, F1, had a symmetric trailing edge with minimal vortex shedding. Both F0 an F1 exhibited similar behaviours both below and above lock-in velocity, and the magnitude of the relative increase in natural frequency was the same. By comparing the damping slopes of the hydrofoils using the reduced velocity, the slopes were nearly identical.

My Contribution: I was responsible for the planning and execution of the experimental setup and the measurement campaign, in addition to having the main workload in analyzing the experimental results and preparing the manuscript.

Paper 6: *PIV Measurements and CFD Simulations of a Hydrofoil at Lock-in*

This paper consists of PIV and and vibration measurements of a hydrofoil at lock-in conditions. Large stream-wise fluctuations in the velocity were observed in the hydrofoil's wake, due to the wandering separation point at lock-in conditions. The frequency shift in the hydrofoil's natural frequency through lock-in was also observed here.

My Contribution: I participated in the experimental measurement campaign, as well as in the discussion of the results, and in the review and proofreading of the manuscript.

Paper 7: *Numerical Simulation of the Hydrodynamic Damping of a Vibrating Hydrofoil*

This paper consists of a one-way coupled simulation of a hydrofoil undergoing forced harmonic vibration. The velocities tested in the numerical setup varied from 2.5 to $45\,\mathrm{m/s}$. Two damping regimes were observed, with a near-constant damping for flow velocities below that of lock-in, and a linearly increasing damping for velocities higher than that of lock-in. It was also found that the damping is independent of vibrational amplitude, for sufficiently small deflections. A phase shift in the vortex shedding with respect to the trailing edge movement was observed, but it was not significant enough to be responsible for the change in damping behavior observed at lock-in. The numerical results show good agreement with the experimental results obtained in Paper 5.

My Contribution: I was in charge of the experimental setup, the experimental measurement campaign, as well as the analysis of the experimental result. In addition to this, I has participated in the discussion of the results, as well as proofreading and reviewing the manuscript.

Paper 8: *Damping Measurements on a Multi-Blade Cascade with Multiple Degrees of Freedom: a Francis-99 Test Case*

This paper investigates the dynamic behavior of a three-bladed cascade. Four modes of vibration have been tested for water velocities up to $20\,\mathrm{m/s}$. All modes of vibration showed a similar slope in the damping when plotted against the *reduced velocity*, even conforming to the results from Paper 4 and Paper 5. The results are also compared with those of other authors, and the theory suggests that by estimating the mode shape and added mass, the damping slope may be estimated for an arbitrary hydrofoil by simply knowing its natural frequency. It can also be argued that this can be performed for more complex structures, with blades coupled through water.

My Contribution: I was responsible for the experimental setup and the measurement campaign, as well as analyzing the data. In addition, I had the main workload in preparing the manuscript.

Chapter IV

Discussion

■ In this chapter, the results from all the included papers are discussed together, as one complete work.

As the objective of this thesis is to investigate and quantify the dynamic loads that affect the life time of a Francis runner, the initial focus was on the draft tube phenomena and Part Load (PL) operation. PL operation can cause considerable vibrations on prototypes, as for La Higuera [16]. This thesis investigated two different PL conditions, one with a fully developed RVR, and one where the tangential velocity is too high for a stable RVR, Deep Part Load (DPL). **Paper 1** focused on characterizing the velocity field in the draft tube cone during DPL operation. This was performed as part of the first Francis-99 workshop, in which the aim was to develop more reliable tools for accurately modelling the complex flows in the draft tube. It was found that even though DPL operation imposes significant losses in efficiency, the instability in the rotating vortex makes it an unfeasible operating point for accurate CFD modelling of the flow structures in the draft tube cone. In addition, investigations performed by Trivedi et al. [34] reveal that the unsteady pressure at the blades' leading edge has a larger amplitude of the RSI component than the RVR component. One of the contributing factors for this could be that DPL is an operating point in which the RVR is not stable. The dynamic loads on the runner are suspected to be more significant during a PL operating condition where the RVR is fully developed. In trying the find the most damaging draft tube phenomena for the runner, **Paper 2** focused on the PL condition with fully developed RVR, i.e. largest amplitudes of the Rheinegans

frequency. In this measurement, it was revealed that, although the pressure and velocity fluctuations in the draft tube cone are quite large, they are not particularly large when compared to the RSI amplitudes. In fact, in the vaneless space, the amplitude of the RSI-induced pulsations are approx. 12 times as large as those from the RVR. This is corroborated by Seidel et al. [35], in which it was found that RSI alone contributes to approx. $80\,\%$ of the total dynamic stress, for a runner with low specific speed. It can therefore be concluded with some certainty that PL operation, even with a fully developed vortex rope, is not a leading cause of turbine failure for low specific speed, ie. high head, Francis runners. With regards to dynamic loads from transient operation, **Paper 3** showed that the cyclic pressure amplitudes associated with the RVR and RSI do not amplify through load rejection, and the RSI is dominating the measurements near the turbine blades throughout the transient. Figure 4.1 shows that throughout the load rejection, the dominating frequency is the RSI frequency, and the amplitude is fairly constant.

This does not categorically reject transient operation as a contributing factor to the runner's dynamic loads, and faster transitions may induce higher loads. However, the amplitudes of RSI remained the largest one, and they were relatively unaffected of this load change. The focus was therefore narrowed down to investigate RSI in more detail.

Paper 4 is a close investigation on the loads from RSI. The test specimen is a fixed-beam hydrofoil. This is of relevance, as there are limited case studies of that type of geometry available. The main findings are that the damping increases linearly with velocity, which corroborates previous works in the field [36, 37, 38, 39]. However, Paper 4 found that the natural frequency increased through the lock-in region. This result is corroborated numerically by Nenneman et al. [40], and experimentally in **Paper 6**, where lock-in was investigated in more detail. It is not clear why the natural frequency exhibits this behaviour, and the prevailing theory from Paper 4 is that it is related to the shift in phase of the vortex shedding when passing through lock-in. As discussed in Paper 4, the effects of vortex-shedding and lock-in were significant on the hydrofoil, making it difficult to make general conclusions about the influence of water velocity on the dynamic behaviour of the blade. In order to avoid the effects of lock-in, a new hydrofoil with a symmetric trailing edge was designed for **Paper 5**, where the the vortex shedding amplitude is at a minimum. The results of this paper are compared to the results of the previous paper, and it is evident that the same behaviour in damping is observed, even though the amplitude of the vortex shedding is minimal.

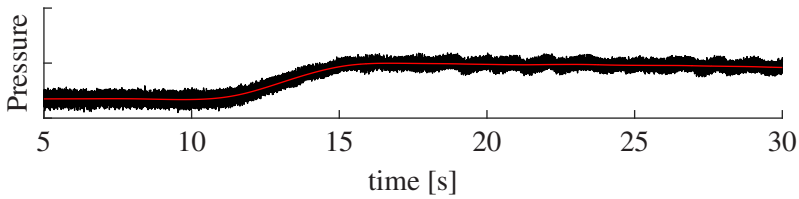

(a) Time series through load rejection

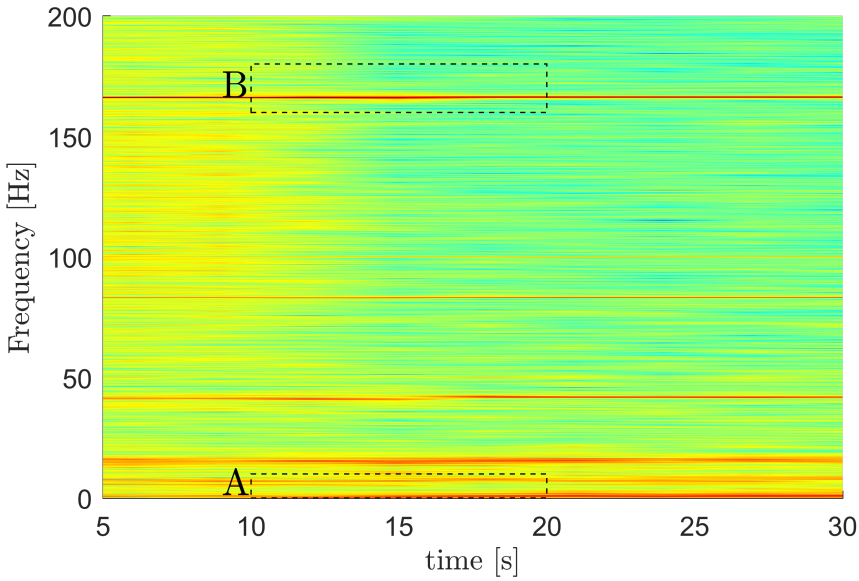

(b) Spectrogram through load rejection

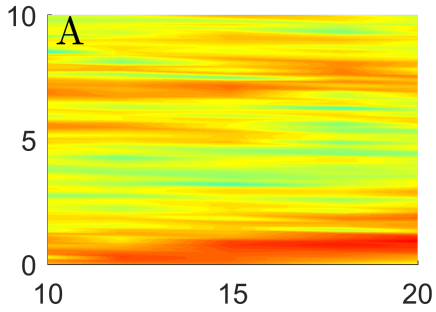

(c) Closeup of section A: RVR frequency range at time of transient

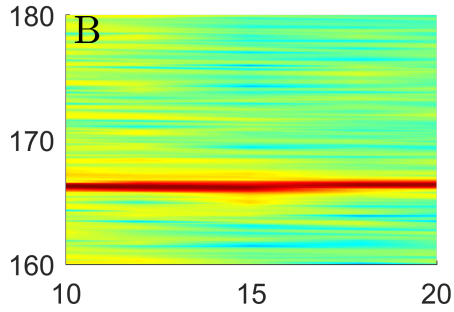

(d) Closeup of section B: RSI frequency range at time of transient

Figure 4.1: Pressure measurements from the vaneless space during load rejection. Note that the RVR frequency cannot be seen in the closeup Figure 4.1c. The RSI amplitude is more or less unchanged throughout the transient, seen in Figure 4.1d.

In this experiment as well, the natural frequency of the hydrofoil was found to increase with water velocity, but the sudden increase through lock-in was not as pronounced as for the case with the asymmetric hydrofoil. This indicates that the increase in natural frequency is related to the lock-in phenomena. This seems to support the previous claim that it is the result of a phase shift in the vortex shedding, but numerical investigations in **Paper 7** contradict this, showing that the phase shift in vortex shedding is minimal.

At this point, it is still unclear how the results will transpose to a turbine runner, for several reasons: There is no rotation in the test case, meaning no gyroscopic or Coriolis forces, there is no rotational symmetry (meaning no complex modes), there are no neighbouring blades, the blades are neither loaded nor double-curved, and the water velocity is the same on both sides. In order to assess some of these discrepancies, **Paper 8** is an investigation on the behaviour of a 3-bladed cascade, where multiple modes of vibration may be examined. Even with four real modes of vibration, with natural frequencies ranging from 250 to $720\,\mathrm{Hz}$, the damping behaviour is similar: small changes up to the velocity at which lock-in occurs, then a linear increase. As **Paper 7** showed, the numerical simulations of this damping behaviour are quite accurate, and the trend is expected to continue up to at least $45\,\mathrm{m/s}$. A question that arises in the comparison with other works on the damping of turbine blades, is how to compare results for different geometries. **Paper 8** showed preliminary evidence that a modified form of the *reduced velocity* can be used to compare the results. It is very similar to the Strouhal number explained in Section 2.2.2, except that geometric parameters are not considered directly. The modified reduced velocity is best defined as the ratio between the water velocity and the blade natural frequency, shown in Equation (4.1).

$$w^* = \frac{w}{f_n} \tag{4.1}$$

$1/f_n$ is the same as the vibration period, and when multiplied by the flow velocity, the resulting term is a unit of length, namely the length that the water will travel during one vibration cycle. This can also be interpreted as a measure of the amount of water that interacts with the moving structure per cycle of vibration. The use of geometric parameters in such comparisons is not straightforward in vibration analysis where FSI is involved. Take as an example, the "characteristic length". Typically, that could be the chord length of the turbine blade. It does not factor in how much of the blade is actually moving. If the chord length is increased, but the movement remains the same, one should expect the relevant non-dimensional

number to remain unchanged, as the change in chord length is not relevant for the interaction with the fluid. By adapting the theory developed by Monette et al [41], we get the damping expressed as in Equation (4.2).

$$\zeta = w^* \left[1 - \left(\frac{f_n}{f_v}\right)^2\right] \frac{\iint \Phi(x,y) \frac{\partial \Phi(x,y)}{\partial x}\, dx\, dy}{\iint \Phi^2(x,y)\, dx\, dy} \tag{4.2}$$

In Equation (4.2), Φ denotes the mode shape, and f_v denotes the structure's natural frequency in vacuum.

Equation (4.2) constitutes three main parts:

1. the "modified reduced velocity", as defined in Equation (4.1)
2. a measure of the added mass, or the thickness of fluid affected by the motion, defined by
$$\widehat{M} = \left[1 - \left(\frac{f_n}{f_v}\right)^2\right] \tag{4.3}$$
3. a measure of the "amount of movement" of the structure, namely the mode shape.
$$\widehat{\Phi} = \frac{\iint \Phi(x,y) \frac{\partial \Phi(x,y)}{\partial x}\, dx\, dy}{\iint \Phi^2(x,y)\, dx\, dy} \tag{4.4}$$

As the results from Paper 8 showed, the product of $\widehat{M}$ and $\widehat{\Phi}$ remained fairly constant for all the hydrofoil tests that comprise this thesis, in addition to conforming with the results of Coutu et al [36]. This suggests one of two things:

- Both $\widehat{M}$ and $\widehat{\Phi}$ remain relatively unchanged
- $\widehat{M}$ and $\widehat{\Phi}$ both change, but the changes cancel each other out

Since $\widehat{\Phi}$ is a normalized numerical representation of how the structure deflects, it is expected that similar geometries—fixed-beam hydrofoils with a tapering trailing edge—exhibit similar traits in the mode shape. In addition, since the deflections are small, added mass per unit area is also expected to remain constant. If this is indeed the case, then one can estimate the damping slope of an arbitrary hydrofoil by simply knowing its natural frequency in water. However, the amount of empirical evidence is limited, and more research is need to make this conclusion.

What is more interesting, is that these parameters remained constant for the transition from a single blade to a multi-blade cascade. This indicates that, since the deformation of each blade is close in resemblance to a single blade's mode of vibration, that the sum of $\widehat{\Phi}$ is the same as for the single blade case, as well as the sum for $\widehat{M}$. This indicates that the inter-blade coupling does not affect the slope of the damping factor.

Chapter V

Conclusion

From the papers that comprise this thesis, the following conclusions can be made:

I: High head Francis runner (with a low specific speed) is much more susceptible to damage from RSI than from draft tube phenomena, even for the case of load rejection.

II: The hydrodynamic damping on the turbine blades increase linearly with water velocity, with differing slopes for velocities below and above that of lock-in. Below lock-in velocity, the damping is nearly constant.

III: There is good agreement between the experimental data obtained in this thesis and numerical simulations of the simplified test geometry. The simulations further show that the linear increase in damping is expected to continue up to at least $45\,\mathrm{m/s}$.

IV: The natural frequency increases with velocity, by about $2.5\,\%$ when going through lock-in.

V: All of the real modes tested on the multi-blade cascade exhibit the same behavior with respect to reduced velocity. This has been extended to compare with other works in the field, through the use of a modified reduced velocity: In this comparison, the damping was found to increase linearly with the water travel distance per vibration cycle, not only within the experiments that comprise this thesis, but also with other experimental works. This suggests that the mode shape integral remains more or less constant for hydrofoils of similar boundary conditions, and that the added mass fraction is unchanged for small perturbances. Consequently, the damping per reduced velocity

will have the same linear slope for an arbitrary hydrofoil of these boundary conditions.

VI: The damping slope does not change when multiple blades were considered. This suggests that the damping slope for the runner blades of a turbine can be estimated using a single-blade approach by integrating the mode shape and estimating the added mass and natural frequency of the blade. However, the effect of complex modes and nodal diameters of the runner structure have not been assessed.

Chapter VI

Further Work

■ In the final stages of the presented work it was revealed that general assertions can be made about the behaviour of geometrically simple hydrofoils, even if they are not geometrically similar. However, there is some work to be done before the same can be said for turbine runner blades, and the following is a list of suggested expansions to this thesis.

6.1 Complex modes and Inter-Blade Phase Angles

A key feature of turbine runners that the experiments in this thesis were unable to assess, is the effects of rotational symmetry. For a structure with rotational symmetry, there will be complex modes of vibration, which will appear as "travelling waves". This was impossible to test in the experiments with multiple blades in a cascade configuration. It is of particular relevance, as the combination of rotor and stator blades will prescribe a pressure field on the runner, which in turn will excite a complex mode of vibration, where the phase angle between two neighbouring blades is neither 0° or 180°. This will couple with the nodal diameters in the hub and shroud, and one cannot, from the findings in this thesis, conclude that the behaviour of a turbine runner will be the same as for a blade cascade.

In order to investigate this phenomenon in particular, a simplified axial turbine is suggested. An inner-tube (shaft) with welded-on blades distributed evenly around the periphery, which in turn is welded onto an outer-tube. In this manner, the boundary condition of a fixed beam is maintained for the blades, while achieving

rotational symmetry. This simplified axial turbine need not rotate, and the blades may be loaded or unloaded, depending on the chosen angle of attack at the time of welding. Such a test rig will have many advantages over a full model runner, such as

1. **No rotation:** Without rotation, optical access to individual blades is made significantly simpler
2. **Simple blades:** The blades may be flat, curved or double curved, depending on the desired complexity. In addition, it is possible to chose whether or not the blades should be loaded
3. **Predictable boundary conditions:** Without the distributor, it is much easier to control the flow conditions entering the test section, such as with a honeycomb flow straightener
4. **Low cost:** Compared to a turbine runner, this simplified runner is very simple to design and manufacture. Even the surrounding test rig need only consist of a piping system and a pump.

6.2 Blades with double curvature

As the blade experiments in this thesis were performed on two-dimensional blades, they exhibited, to some degree, plate-like vibration: vibration on both the leading edge and trailing edge. For a high head Francis runner, such vibrations may not be strictly relevant, as they have long and twisted blades of short width, and most of the vibration will therefore be limited to the trailing edge. Although the findings in this thesis indicate that the behaviour in different blades should be the same, it cannot be categorically denied that blades of double curvature may behave differently.

This can be tested, with a simplified blade channel in a (round) pipe. The blade will span the diameter of the pipe, and the blade will then twist in the stream wise direction, always spanning the diameter of the pipe. If desired, this can be built into a pipe of whether increasing or decreasing diameter, to make the blade more "turbine-like".

6.3 Loaded blades

Blade loading will supply the turbine blades with a pre-stress, which in turn will affect their natural frequency. This raises the question: How will this affect the

damping slope? The findings of this thesis, is that the change in damping per reduced velocity is constant, regardless of natural frequency of the blades, but in that regard, the natural frequency of the blades is only a measure on a combination of material properties and blade geometry, **not** a measure of the loads from the water. This can be verified experimentally through a test rig in which it is possible to vary the angle of attach on the installed blade. It is of particular relevance, as the blades in a runner are loaded, and their natural frequency will thus vary with their load.

References

[1] C. Trivedi, B. Gandhi and C. J. Michel. 'Effect of Transients on Francis Turbine Runner Life: A Review'. In: *Journal of Hydraulic Research* 51.2 (Apr. 2013), pp. 121–132.

[2] Bo Yang et al. 'On the Use of Energy Storage Technologies for Regulation Services in Electric Power Systems with Significant Penetration of Wind Energy'. In: *2008 5th International Conference on the European Electricity Market*. Lisboa, Portugal: IEEE, May 2008, pp. 1–6.

[3] C. Fernandes et al. 'A Long-Term Prospective for the Spanish Electricity System'. In: *2010 7th International Conference on the European Energy Market*. Madrid, Spain: IEEE, June 2010, pp. 1–6.

[4] H. Wang et al. 'Analysis and Control of the Part Load Vortex Rope in the Draft Tube of a Pumpturbine'. In: *Proceedings of the 6th IAHR International Meeting of the Workgroup on Cavitation and Dynamic Problems in Hydraulic Machinery and Systems*. Ljubljana, Slovenia, Sept. 2015.

[5] A. Zervos, C. Lins and Canadian Electronic Library (Firm). *Renewables 2018 Global Status Report*. 2018.

[6] J. I. Pérez-Diaz et al. 'Dynamic Response of Hydro Power Plants to Load Variations for Providing Secondary Regulation Reserves Considering Elastic Water Column Effects'. In: *Przeglad Elektrotechniczny* 88 (Jan. 2012).

[7] I. E. Agency. *World Energy Outlook 2017*. 2017.

[8] I. Graabak and M. Korpås. 'Balancing of Variable Wind and Solar Production in Continental Europe with Nordic Hydropower – A Review of Simulation Studies'. In: *Energy Procedia* 87 (Jan. 2016), pp. 91–99.

[9] H. Bjørndal, T. Moltubakk and G. Hydro. 'Strain Gauge Measurements in an Operating Plant and Comparison with Finite Element Analysis'. In: *IAHR-AIRH Work Group on the Behaviour of Hydraulic Machinery under Steady Oscillatory Conditions, 10th International Meeting*. Trondheim, Norway: NTNU, June 2001, p. 11.

[10] P. T. K. Østby et al. 'Dynamic Stresses In High Head Francis Turbines'. In: *International journal on hydropower and dams* 23.3 (2016), p. 11.

[11] U. Seidel et al. 'Dynamic Loads in Francis Runners and Their Impact on Fatigue Life'. In: *IOP Conference Series: Earth and Environmental Science*. Sept. 2014, p. 9.

[12] L. R. J. Sundström et al. 'LDA Measurements in the Francis-99 Draft Tube Cone'. In: *IOP Conference Series: Earth and Environmental Science* 22.2 (Mar. 2014), p. 022012.

[13] G. D. Ciocan et al. 'Experimental Study and Numerical Simulation of the FLINDT Draft Tube Rotating Vortex'. In: *Journal of Fluids Engineering* 129.2 (2007), p. 146.

[14] D. N. Konidaris and J. A. Tegopoulos. 'Investigation of Oscillatory Problems of Hydraulic Generating Units Equipped with Francis Turbines'. In: *Energy Conversion, IEEE Transactions on* 12.4 (1997), pp. 419–425.

[15] P. Dörfler, M. Sick and A. Coutu. *Flow-Induced Pulsation and Vibration in Hydroelectric Machinery: Engineer's Guidebook for Planning, Design and Troubleshooting*. London ; New York: Springer, 2013.

[16] P. J. Gogstad and O. G. Dahlhaug. 'Experimental Investigation of Air Injection in High Head Francis Turbines'. In: *International journal on hydropower and dams* 24 (2017), pp. 70–74.

[17] E. Kobro. 'Measurement of Pressure Pulsations in Francis Turbines'. Doctoral Thesis. Trondheim, Norway: NTNU, 2010.

[18] IEC 60193. *Hydraulic turbines, storage pumps and pump-turbines: Model acceptance tests*. Tech. rep. 2831849934. 3, rue de Varembé, PO Box 131, CH-1211 Geneva 20, Switzerland. 16 November: International Electrotechnical Commission, 1999, p. 578.

[19] J. M. Beér and N. A. Chigier. *Combustion Aerodynamics*. Fuel and energy science series. London: Applied Science Publishers Ltd, 1972.

[20] H. Sheen et al. ‘Correlation of Swirl Number for a Radial-Type Swirl Generator’. In: *Experimental Thermal and Fluid Science* 12.4 (May 1996), pp. 444–451.

[21] O. G. Dahlhaug. ‘A Study of Swirl Flow in Draft Tubes’. Doctoral Thesis. NTNU, Dec. 1997.

[22] W. J. Rheinegans. ‘Power Swings in Hydroelectric Power Plants’. In: *Trans. ASME* 62.3 (1940), pp. 171–184.

[23] A. I. Bosioc et al. ‘Unsteady Pressure Analysis of a Swirling Flow with Vortex Rope and Axial Water Injection in a Discharge Cone’. In: *Journal of Fluids Engineering* 134.8 (2012), p. 081104.

[24] I. Oftebro and A. Lønning. ‘Paper 2: Pressure Oscillations in Francis Turbines’. In: *Proceedings of the Institution of Mechanical Engineers, Conference Proceedings*. Vol. 181. SAGE Publications, 1966, pp. 119–124.

[25] *Going with the Flow*. https://earthobservatory.nasa.gov/images/88005/going-with-the-flow. Text.Article. May 2016.

[26] M. Van Dyke, ed. *An Album of Fluid Motion*. 4th ed. OCLC: 845916635. Stanford, Calif: Parabolic Press, 2008.

[27] H. Schlichting and K. Gersten. *Boundary-Layer Theory*. Trans. by K. Mayes. Ninth edition. OCLC: 951636190. Berlin Heidelberg: Springer, 2017.

[28] V. Strouhal. ‘Ueber eine besondere Art der Tonerregung’. In: *Annalen der Physik und Chemie* 241.10 (1878), pp. 216–251.

[29] W. D. Callister. *Materials Science and Engineering: An Introduction*. 7th ed. OCLC: ocm61463872. New York: John Wiley & Sons, 2007.

[30] A. S. Yasir. ‘Study the Effect of Cooling Rate on Fatigue Strength and Fatigue Life of Heated Carbon Steel Bars’. In: *Mechanical Engineering Research* 3.2 (July 2013).

[31] D. J. Ewins. *Modal Testing: Theory, Practice, and Application*. 2nd ed. Mechanical engineering research studies 10. Baldock, Hertfordshire, England ; Philadelphia, PA: Research Studies Press, 2000.

[32] R. R. Craig, A. Kurdila and R. R. Craig. *Fundamentals of Structural Dynamics*. 2nd ed. Hoboken, N.J: John Wiley, 2006.

[33] Charles C. Kennedy. ‘Use of Vectors in Vibration Measurement and Analysis’. In: *Journal of the Aeronautical Sciences* 14.11 (Nov. 1947), pp. 603–625.

[34] C. Trivedi et al. 'Experimental and Numerical Studies for a High Head Francis Turbine at Several Operating Points'. In: *Journal of Fluids Engineering* 135.11 (Aug. 2013), pp. 111102–111102.

[35] U. Seidel et al. 'Evaluation of RSI-Induced Stresses in Francis Runners'. In: *IOP Conference Series: Earth and Environmental Science* 15.5 (Nov. 2012), p. 052010.

[36] A. Coutu et al. 'Damping Measurements in Flowing Water'. In: *IOP Conference Series: Earth and Environmental Science* 15 (2012), p. 062060.

[37] S. Roth et al. 'Hydrodynamic Damping Identification from an Impulse Response of a Vibrating Blade'. In: *Proceedings of the 3rd IAHR International Meeting of the Workgroup on Cavitation and Dynamic Problems in Hydraulic Machinery and Systems*. Vol. 1. Brno, Czech Republic: Brno University of Technology, 2009, pp. 253–260.

[38] Z. Yao et al. 'Effect of Trailing Edge Shape on Hydrodynamic Damping for a Hydrofoil'. In: *Journal of Fluids and Structures* 51 (Nov. 2014), pp. 189–198.

[39] M. C. Reese. 'Vibration and Damping of Hydrofoils in Uniform Flow'. MA thesis. The Pennsylvania State University, 2010.

[40] B. Nennemann, C. Monette and J. Chamberland-Lauzon. 'Hydrodynamic Damping and Stiffness Prediction in Francis Turbine Runners Using CFD'. In: *IOP Conference Series: Earth and Environmental Science* 49 (Nov. 2016), p. 072006.

[41] C. Monette et al. 'Hydro-Dynamic Damping Theory in Flowing Water'. In: *IOP Conference Series: Earth and Environmental Science* 22.3 (Dec. 2014), p. 032044.

Part II

Papers

Paper 1

Preliminary Measurements of the Radial Velocity in the Francis-99 Draft Tube Cone

Bergan, C. W., Amiri, K., Cervantes, M. J, Dahlhaug, O. G.

IOP Conference Series: Journal of Physics vol. 579, 2015

Preliminary Measurements of the Radial Velocity in the Francis-99 Draft Tube Cone

Carl Bergan[1], Kaveh Amiri[2], Michel J Cervantes[1,2] and Ole G Dahlhaug[1]

[1] Department of Energy and Process Engineering, Waterpower Laboratory, Norwegian University of Science and Technology, Trondheim, Norway

[2] Department of Engineering Science and Mathematics, Luleå University of Technology, Luleå, Sweden

E-mail: carl.w.bergan@ntnu.no

Abstract. Two-dimensional particle image velocimetry (PIV) measurements in the draft tube cone of the Francis-99 model have been performed to complete the actual experimental data set with radial velocity data. The velocity profiles obtained presented some variation, which reason has not yet been identified. The presented results are therefore presented as preliminary until the reason is assessed. The axial velocity profiles corroborate well with the ones previously measured with laser Doppler velocimetry (LDV) for all operating points investigated. The radial velocity measured is small in magnitude for all operating points compared to the axial velocity. A gyroscopic effect induced by the swirl leaving the runner and the draft tube bend seems to induce an asymmetry in the draft tube cone.

1. Introduction

Francis-99 is a series of upcoming workshops aiming at determining the state-of-the-art in simulation of high head Francis turbines. For that purpose, the geometry, meshes and experimental results of a high Francis model, the Tokke turbine, were made available to the public at three different operating points: best efficiency point (BEP), part load (PL) and high load (HL), see www.francis-99.org and Chirag et al [1] for more information. The goal of the workshop is to promote the development of numerical tools for the design of high head Francis turbines. The experimental results made available to validate the numerical results comported efficiency, time dependent pressure measurements and velocity measurements. The velocity measurements were acquired in the draft cone at two different locations with laser Doppler velocimetry (LDV), see Figure 3. The measurements comported the axial and the tangential velocities, Sundström et al. [2]. The radial velocity component in high head draft tube cone is small but none the less of importance to assess correctly eventual separation regions. Its determination with optical instrument such as LDV and particle image velocimetry (PIV) is delicate.

PIV and LDV are well-established methods for velocity measurement and have been applied in several turbine-related applications in recent years. PIV is not yet as widespread as LDV, due to its high demand for optical access. PIV has some substantial advantages over LDV, especially for transient phenomena, due to its ability to simultaneously capture a large velocity field with a high data rate. Furthermore, the radial velocity is easily obtained with PIV compared to

LDV. Several set-up configurations of 3D spectroscopic PIV have been investigated by Ciocan [3], with extensive investigation of the data to correct for optical distortion, overlapping of two cameras and set-up for data synchronization. Inter-channel flows in propeller turbines have been investigated by Aeschlimann et al. [4] by the use of stereoscopic PIV in order to obtain 3-component velocity fields. The flow in a Francis turbine draft tube has been investigated by Iliescu et al. [5] using a combination of 3D PIV and LDV.

In the present paper, PIV measurements performed on the Francis-99 test case are presented to complete the actual data set available to validate the numerical simulations. The objectives are to determine the radial velocity in the draft tube cone at the location where the axial and tangential velocities were determined by Sundström et al. [2] with the help of LDV. The axial velocity is also measured with the radial velocity allowing investigating the repeatability of the measurements. Furthermore, contour plots of the meridional velocity are made available for qualitative comparisons.

2. Experimental Setup

The experiment was carried out on a 1:5.1 model Francis turbine of a prototype found at a Norwegian hydropower plant called Tokke. The prototype runner has an inlet diameter of 3.22 m, outlet diameter of 1.78 m, a nominal head of 377 m, and a nominal power output of 110 MW. The distributor is composed of a spiral casing with 14 stay vanes and 28 guide vanes. The runner has 15 full-length blades, and 15 half-blades, also known as splitter blades.

2.1. Test rig

The test rig was operated in a closed-loop configuration, where the pressure and the flow rate are controlled by setting the speed of the pump. The system is fitted with a high-pressure water reservoir upstream the turbine, and a low-pressure reservoir downstream the draft tube. The gauge pressure in the low-pressure reservoir can be independently controlled from 0 down to approximately −9 m, to trigger or prevent cavitation. The experiments were performed under cavitation free conditions. A sketch of the test rig is shown in Figure 1

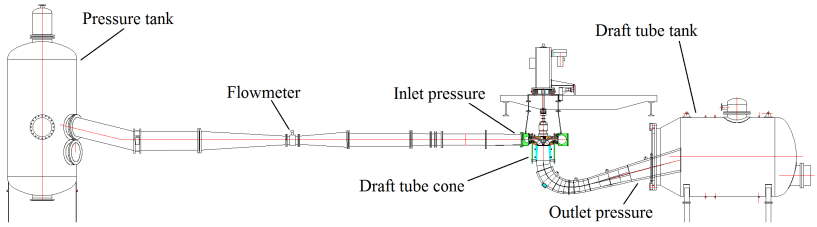

Figure 1. The Francis test rig when operated in closed loop configuration.

The measurements were performed in the draft tube cone. This section is made of Plexiglas for optical access. The draft tube cone was fitted with an index-matching box made of glass and filled with water, to reduce optical distortion.

The operating conditions investigated by Trivedi [1] are listed in Table 1. The specific speed and the specific flow listed in Table 1 are dimensionless numbers defined by Equation 1 and Equation 2.

$$n_{ED} = \frac{n \cdot D}{\sqrt{g \cdot H}} \tag{1}$$

$$Q_{ED} = \frac{Q}{D^2 \cdot \sqrt{g \cdot H}} \tag{2}$$

Table 1. Operating conditions as provided by Trivedi [1].

Operating Point -	Head m	Flow Rate m^3/s	Runner frequency Hz	n_{ed} -	Q_{ed} -	Hydraulic efficiency -
BEP	11.91	0.203	5.59	0.18	0.15	92.6
HL	11.84	0.221	6.16	0.20	0.17	90.6
PL	12.29	0.071	6.77	0.22	0.05	71.7

However, upon reaching the proposed operating points, a small but clearly visible instability in the generator torque was detected. The operating conditions were slightly shifted while maintaining the values for n_{ed} and Q_{ed}, see Sundström et al. [2], giving the operating conditions listed in Table 2.

Table 2. Operating conditions used in this paper.

Operating Point -	Head m	Flow Rate m^3/s	Runner frequency Hz	n_{ed} -	Q_{ed} -	Hydraulic efficiency -
BEP	12.77	0.208	5.74	0.18	0.15	92.4
HL	12.61	0.228	6.34	0.20	0.17	91.0
PL	12.30	0.072	6.77	0.22	0.05	72.5

In order to assess the variation on the velocity profiles of these new operating conditions, a sensitivity analysis was performed, by measuring the time-averaged velocity profiles for the given BEP and the shifted BEP (see Sundström et al. [2]). The velocities are scaled with the bulk velocity leaving the runner, for comparison purposes. These are presented in Figure 2. The velocity difference between the two operating heads is considered relatively small.

2.2. LDV and PIV setup

The LDV used is composed of a Spectra-Physics Model 177G, equipped with a Burst Spectrum Analyzer (BSA) from Dantec Dynamics. The LDV probe was mounted on a traverse table with the probe perpendicular to the glass wall of the index matching box [2]. The perpendicularity was checked with optical methods with an accuracy of 0.2°. The measurement positions are presented in Figure 3. The front lens had a focal length of 310 mm. The seeding particles used were of the type Expancel 46 WU 20 with an average diameter of 6 µm. The axial end tangential velocities were recorded at each coordinate for 720 s, resulting in 70 000-2 000 000 samples, depending on the measurement point location and the operating point. Each velocity profile was investigated with 16 measurement points along the radius for BEP and HL, and at 26 points for PL. The large number of measurement points at PL was necessary to capture the high velocity gradients. The recording time was reduced to 600 s for the last measurements.

A 2D PIV system from TSI was used to measure the axial and radial velocity components in the draft tube cone. Pulse light sheets with a thickness of about 3 mm were generated by

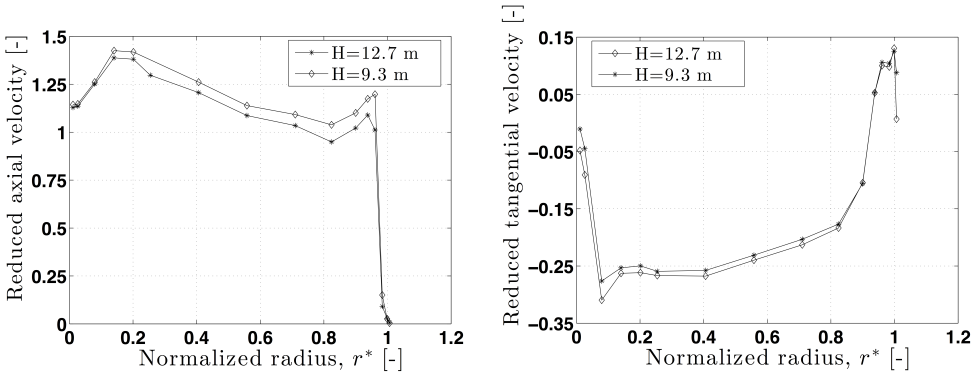

Figure 2. Sensitivity analysis for axial velocity (left) and tangential velocity (right). The velocities are reduced by the bulk velocity leaving the runner.

a Litron Laser NANO L100-50PIV. The illuminated field was recorded by a 4 Mpixel camera (VC-4MC-M180). TSI seeding particles, with a density of 1.016 g/cc, refractive index of 1.52 and mean diameter of 55 µm were used during the measurements. The PIV measurements were performed with an acquisition frequency of 40 Hz. 750 paired images with a time difference of 200 µs were recorded at each measurement section. The velocity profiles measured by PIV were measured in a near-perpendicular direction to the measurement direction of the LDV system, as shown in Figure 3. The axial velocity profiles measured by the PIV and LDV systems can therefore be used to evaluate the flow asymmetry. The PIV system was calibrated using a 2D calibration target. The calibration was performed ex-situ due to the practical limitations associated with the in-situ calibrations.

The velocity profiles measured with the LDV system were measured at two axial positions, as indicated in Figure 3. The PIV system measured velocity in a zone including these two axial coordinates. Note that the measurement axis of the LDV measurements is not parallel with the inlet pipe axis, see Figure 3. The repeatability of the PIV measurements were checked along the radius at a third axial position, indicated as section III in Figure 3.

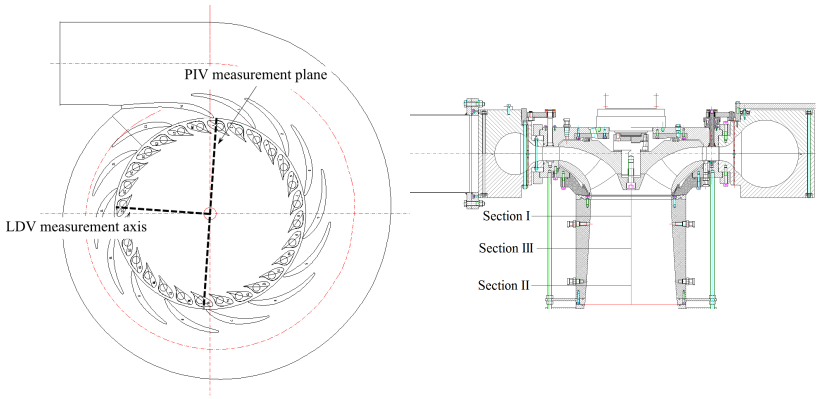

Figure 3. Measurement positions for PIV and LDV as seen from above (left) and from the side (right). Note that the LDV measurement axis is not parallel to the inlet pipe axis. In the right figure, section I, II and III are taken at 57, 377, and 188 mm below the draft tube inlet, respectively. Section I and II are the axial positions of the LDV measurements, while section III is used to test the repeatability of the PIV measurements.

3. Data Analysis

The velocity measurements from the LDV were time-averaged in each measurement point to give a velocity profile. The velocity was then made dimensionless with the bulk velocity downstream the runner for the given operating point, for comparison purposes. The values for the bulk velocity were 0.75 m/s for PL, 2.18 m/s for BEP, and 2.39 m/s for HL. The radial coordinate was made dimensionless with the runner outlet diameter. For the contour plot, the y-coordinate was made dimensionless with the runner outlet diameter, and the zero value was set to the runner outlet. In the results, the radial velocity (u_r^*) is positive in the direction away from the draft tube center, and the axial velocity (u_z^*) is positive in the stream wise direction.

The commercial PIV software, DynamicsStudio, from Dantec dynamics was used for image processing and PIV data analysis. Adaptive correlation scheme with two refinement steps and 50% overlap between the adjacent windows was applied on the acquired data after performing the 2D calibration. The averaged velocity vector maps at each operating point are presented in this paper. The velocities for the PIV were measured in two overlapping sections. In reconstructing these, each data set was re-sampled at uniform intervals in the non-overlapping sections. The overlapping sections were re-sampled using data from both set, before they were weight-averaged using a sine half-wave distribution weighing, giving a transition from the upper window to the lower window. In doing this, the data from the upper window will dominate the overlap close to the upper window, while the data from the lower window will dominate the overlap close to the lower window. The weighing method was chosen on qualitative assessment of the velocity contour plots.

4. Repeatability of the measurements

In order to evaluate the repeatability of the measurements, axial and radial velocity profiles in section III, at the overlapping region of the two measurement windows, are investigated. The velocity profiles at the BEP are presented in Figure 4. The measurements were performed three times at each window. Some discrepancy exists between the upper and lower window measurements, both in axial and radial velocities. The measurements for each window were

performed on different days while the test rig was operating continuously. The highest level of discrepancies in both components is found close to the central part of the draft tube where the velocity is higher than close to the wall region. The measurements performed by Sundström et al. [2] indicate the presence of a free vortex in the central region rotating in the opposite direction of the runner. The vortex seems sensible to initial conditions.

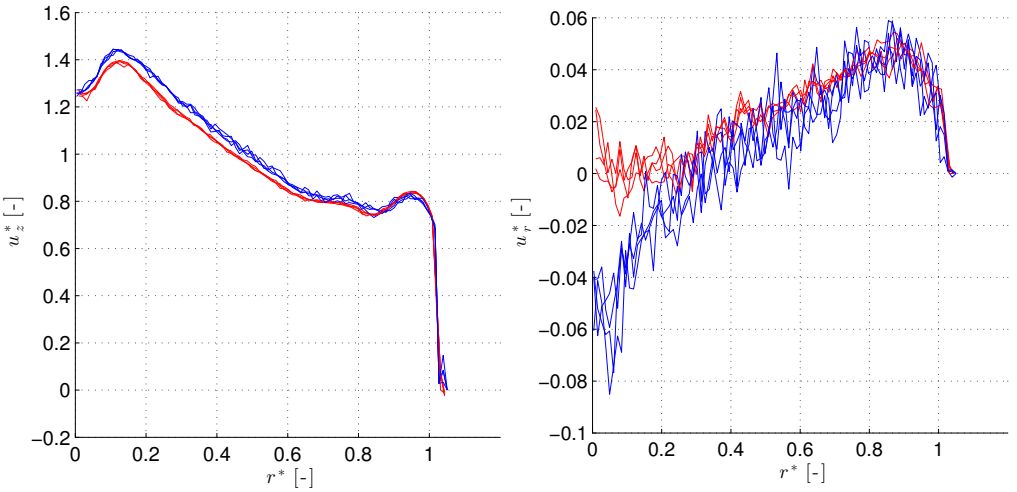

Figure 4. Mean axial (left) and radial (right) velocity profiles at section III for BEP operation. The red lines are data from the lower measurement window and the blue lines are data from the upper measurement window.

Figure 5 presents the velocity profiles at section III for HL operation. The velocity profiles are similar to the BEP case. A larger discrepancy appears in the central region of the draft tube. At this operation point, the swirl leaving the runner is larger than at the BEP point, see Sundström et al. [2].

Figure 6 presents the velocity profiles at section III for PL operation. In this figure, the measurements obtained with the full measuring window are included. At this operating point, a large recirculation region appears below the runner in the central region of the draft tube. The axial velocity, as well as the radial velocity, are subject to a large gradient in the radial direction. Furthermore, the magnitude of the radial velocity is significantly larger than for the two other operating points. The discrepancies appear in the region of high axial velocity coinciding with region of large swirl. At this operation condition, the ratio of the tangential to the axial velocity is above 1.5, see Sundström et al. [2].

The difference in measured velocities can stem from either a difference in operating conditions, errors in the PIV calibration, or a physical phenomenon. The experimental conditions are controlled by the flow rate (Q), the guide van opening angle (α), the turbine rotational speed, and the turbine head (H). Dimensionless parameters n_{ED} and Q_{ED} are used to characterize the turbine operation. The maximum deviation of these parameters is shown in Table 3. The deviations are considered to be too small to cause the observed differences in the velocity profiles. The complete results from the comparison given in Table 3 can be found in tabular form in appendix A.

An index matching box filled with water was used to decrease the light aberration during the PIV measurements. A 2D calibration target was used to compensate for the light aberration

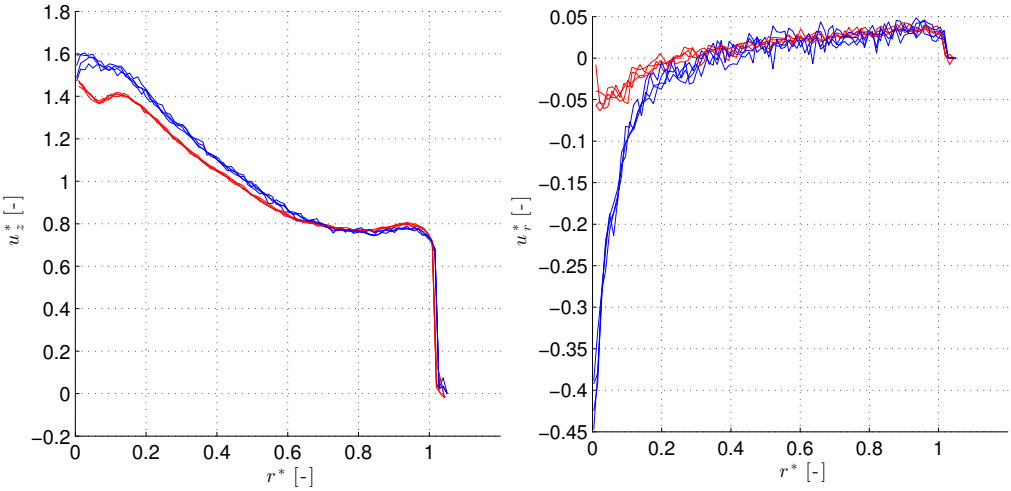

Figure 5. Mean axial (left) and radial (right) velocity profiles at section III for HL operation. The red lines are data from the lower measurement window and the blue lines are data from the upper measurement window.

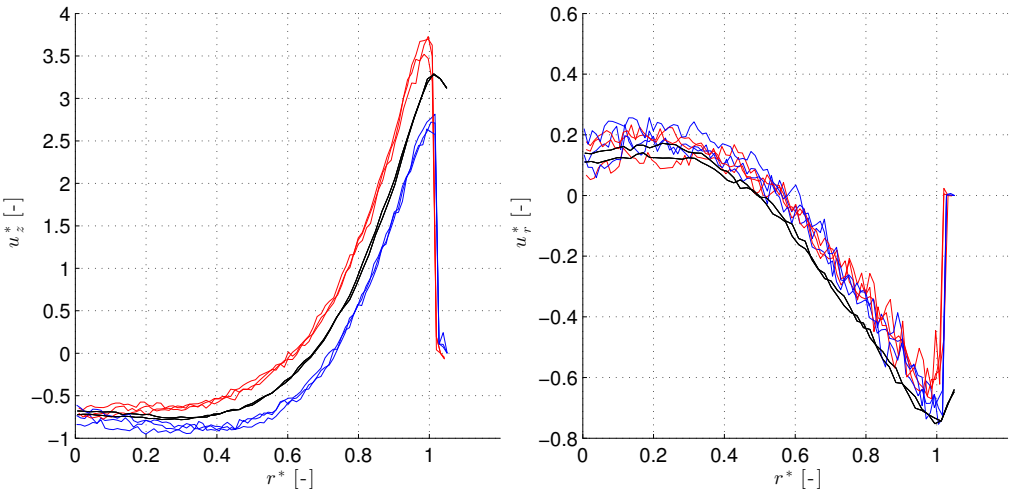

Figure 6. Mean axial (left) and radial (right) velocity profiles at section III for PL operation. The red lines are data from the lower measurement window, the blue lines are data from the upper measurement window, and the black lines are data from the full window measurement.

which still exists close to the areas of high curvature, i.e., close to the draft tube wall. Figure 7 presents a picture of the calibration target in the Plexiglas draft tube cone. Seen in the figure, there is a distance between the draft tube wall and the first calibration point. Hence, the calibration results are extrapolated close to the wall. Moreover, the picture is warped

Table 3. Maximum deviations in operating conditions. The deviations are given as maximum percentage variation from the mean value over the different measurements of the given condition.

	PL	BEP	HL
Q_{ed}	0.37 %	0.14 %	0.14 %
n_{ed}	0.03 %	0.01 %	0.03 %
H	0.05 %	0.05 %	0.05 %
Q	0.36 %	0.12 %	0.12 %
α	0.00 %	0.00 %	0.00 %

significantly close to the wall but unaffected along the draft tube cone centerline. Thus, the calibration matrix calculated may be subject to some uncertainties close to the wall, i.e., in the region $r^* > 0.85$. Consequently, the axial velocity profiles cannot be affected by the calibration process all along the radius. The calibration uncertainty in the radial direction may result in variation in the radial velocity magnitude and not its direction. However, the results showed that the uncertainty in the radial direction is too small to cause the observed differences in the velocity profiles. If calibration has some effects on the velocity profiles, it should be restricted near the wall region and just in the radial velocity profile, while, as shown in Figure 4, the discrepancies can be seen in the high velocity region close to the draft tube center in this case.

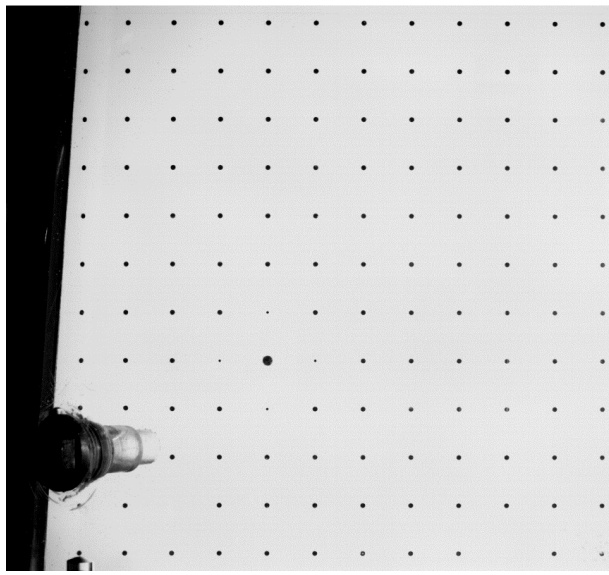

Figure 7. 2D calibration target inside the draft tube cone.

The discrepancies appear only between profiles obtained after restarting the test rig. The discrepancies in the measured profiles are mostly significant in region of high swirl and axial velocities. It may be argued that the swirl encountered in the draft tube cone is sensitive to initial conditions. As a matter of fact, the swirl living the runner creates an asymmetrical flow

in the draft tube after the elbow through gyroscopic effects. The flow is divided into a low and high velocity region which extend may be sensible to initial condition. The question needs to be further addressed and the following measurements are considered as preliminary as long as the matter is not completely addressed.

5. Results and discussion

The axial and radial velocity profiles obtained at section I and II with the PIV system are presented in this section. The axial velocity is compared with the LDV measurements of Sundström et al. [2]. Velocity contours at each operating point are also included.

5.1. BEP results

Figure 8 shows the dimensionless axial and radial velocity profiles at section I for BEP operation. The trend captured by the LDV and PIV measurements is similar. There are some differences between the results especially in the wake region of the runner hub. A probable asymmetry at the runner outlet may be the reason, since the PIV and LDV measurements were not performed at the same azimuthal position as presented in Figure 3. Such an asymmetry may stem from the asymmetric flow distribution at the spiral casing distributor as reported by some researchers, see Amiri [6], but also from the gyroscopic effect as previously mentioned. The PIV measurements show slightly lower axial velocities in the middle part of the graph ($0.2 < r^* < 0.8$) and higher velocities in the region affected by the runner hub wake. An integration of the velocity profiles results in comparable flow rate for the two measurements assuming a symmetrical flow at the runner outlet, in agreement with the flow rate measurements. The axial velocity shows a linear decrease with the radius in the middle part of the graph ($0.2 < r^* < 0.8$). The axial velocity decreases again towards the centerline of the draft tube due to the runner hub wake. The axial velocity slightly increases close to the wall. This may be due to the design criteria to energize the boundary layer on the draft tube cone or may be related to the tip clearance. Illustrated in Figure 8, the radial velocity is increasing with the radius at the draft tube inlet. The results show that the radial velocity is positive close to the draft tube wall as expected for a diffuser. The flow at the draft tube cone centerline is expected to be purely axial for symmetric flow at the runner outlet. However, the negative radial velocity indicates an asymmetrical flow that may also be the source of the discrepancies between the PIV and LDV measurement results, as discussed before.

Figure 9 presents the velocity distribution at section II. The agreement between the LDV and the PIV results is much better. The axial velocity profile is similar to the velocity profile captured at section I. Surprisingly, the radial velocity is somewhat lower close to the centerline. The negative radial velocity at the draft tube center will move water into the other side of the draft tube, causing a higher velocity in that window, than in the one presented here. This is due to the gyroscopic effect induced by the draft tube bend. The LDV measurement results presented by Sundström et al. [2] showed that the flow at the runner outlet counter-rotates with respect to the runner rotation at the BEP. The rotating flow leaving the runner together with the draft tube bend produces a gyroscopic force resulting in an asymmetric flow in the draft tube cone. The asymmetry effect may propagate upstream resulting in some asymmetry at section I as presented in Figure 8.

Figure 10 presents the contour plot of the meridional velocity inside the draft tube cone. The results indicate a well-distributed flow in the draft tube cone. The figure shows the flow development along the draft tube cone. The velocity smoothly decreases in the stream wise direction without separation. The presence of the hub is seen in the upper center of the draft tube cone, where the velocities are lower. The hub effect can also be seen in Figure 9, where the radial velocity shows a sharp change at $r^* = 0.19$, the radial position of the runner hub cone. A visible boundary layer can also be seen in the axial velocity component in Figure 9, where the

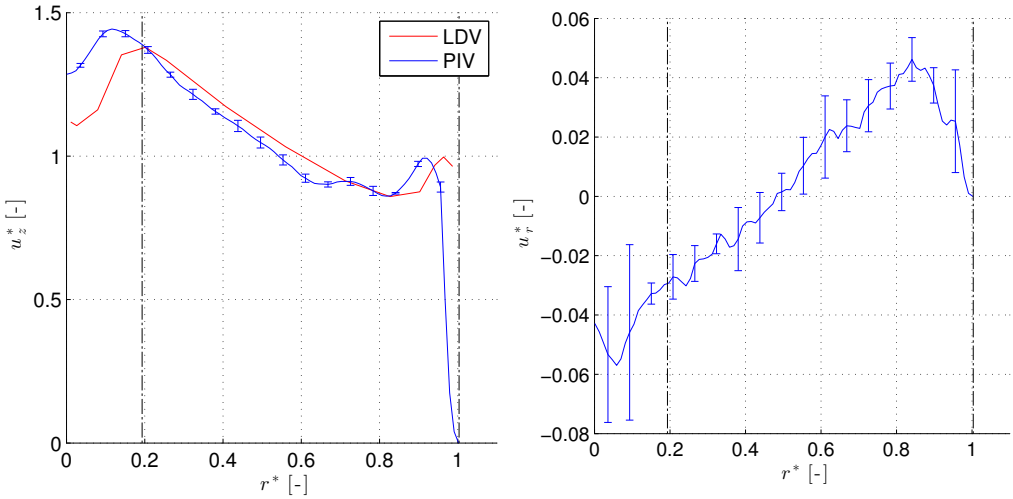

Figure 8. Axial (left) and radial (right) velocities at section I for BEP operation. The red line shows the LDV result obtained by Sundström et al. [2] and the blue line shows the mean PIV results. The error bars indicate a 95% confidence interval. The dashed lines at $r^* = 0.19$ and $r^* = 1.00$ indicate the radial position of the runner hub corner and the draft tube entrance, respectively. Note the difference in scale on the ordinate axis.

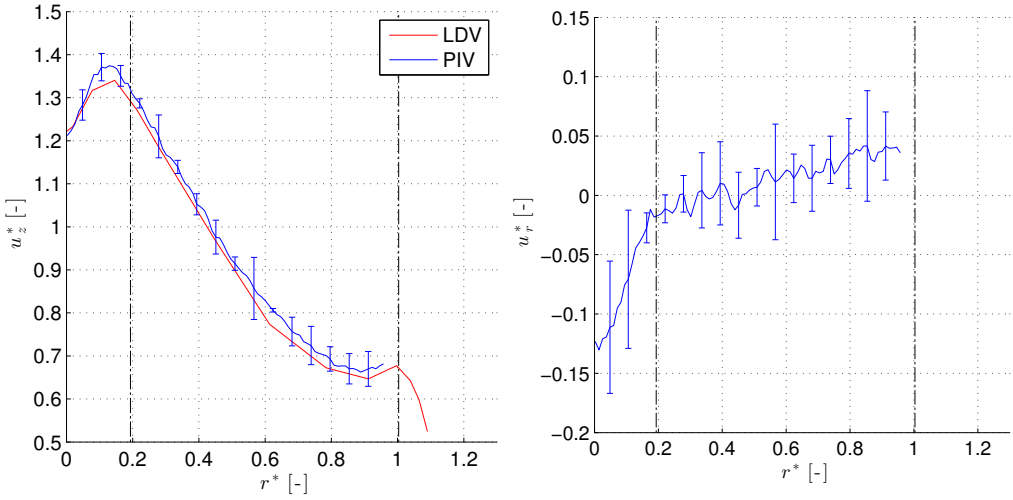

Figure 9. Axial (left) and radial (right) velocities at section II for BEP operation. The red line shows the LDV result obtained by Sundström et al. [2] and the blue line shows the mean PIV results. The error bars indicate a 95% confidence interval. The dashed lines at $r^* = 0.19$ and $r^* = 1.00$ indicate the radial position of the runner hub corner and the draft tube entrance, respectively. Note the difference in scale on the ordinate axis.

velocity shows a visible reduction at $r^* = 1$. This is only visible in the LDV measurements, since one of the lower pressure bolts prevents optical access.

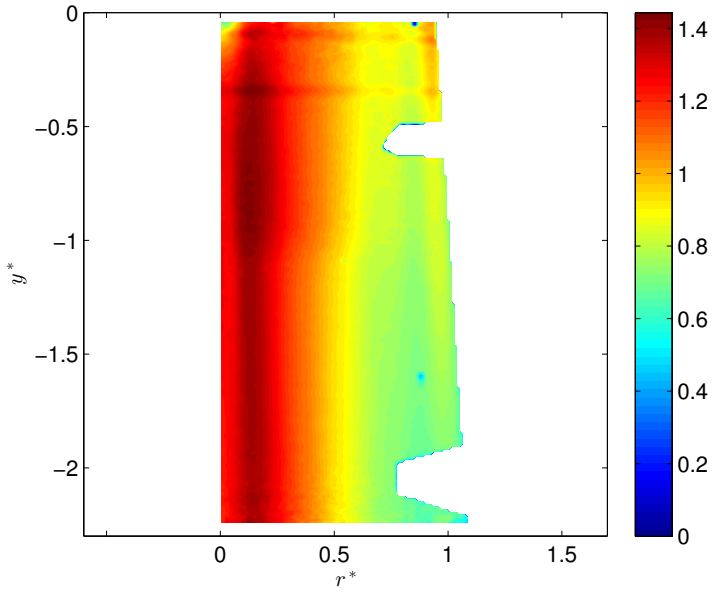

Figure 10. Contour plot of the meridional velocity within the PIV plane at BEP. Pressure bolts in the draft tube cone are seen in both the upper and lower part of the cone. The maximum velocity is obtained at $r^* = 0.15$

5.2. HL results

Axial and radial velocity profiles at section I are presented in Figure 11 while the turbine operates at HL. The low velocity region in the wake of the runner hub, presented in the BEP case, does not exist anymore and the axial velocity decreases with the radius all along the draft tube. The radial velocity shows the same profile as the one at the BEP: monotonically increasing with the radius. The flow direction is towards the draft tube wall at $r^* > 0.5$ and towards the draft tube centerline at $r^* < 0.5$. The radial velocity shows a sharp decrease in the middle of the draft tube, at the radial position of the runner hub corner. Sundström et al. [2] showed that the swirl exiting the runner at the HL is higher than the one at the BEP. Hence, the gyroscopic effect is expected to be higher for HL, resulting in a larger decrease in the radial velocity in the middle of the draft tube cone. The radial velocity at section II (Figure 12) is three times larger close to the draft tube bend compared with section I, supporting the hypothesis of an asymmetry imparted by the gyroscopic effect induced by the draft tube bend. The axial velocity profile at section II is similar to the profile captured at section I, but with a lower magnitude, as expected. The draft tube cone decreases the axial velocity, allowing for the recovery of pressure.

Figure 13 shows the contour plot of the meridional velocity at the HL operating point. The contour plot is altered along two horizontal lines of $y^* = -0.09$ and $y^* = -0.34$. It may be due to the change in draft tube angle at those positions resulting in different light aberration at the position that the angle is changed.

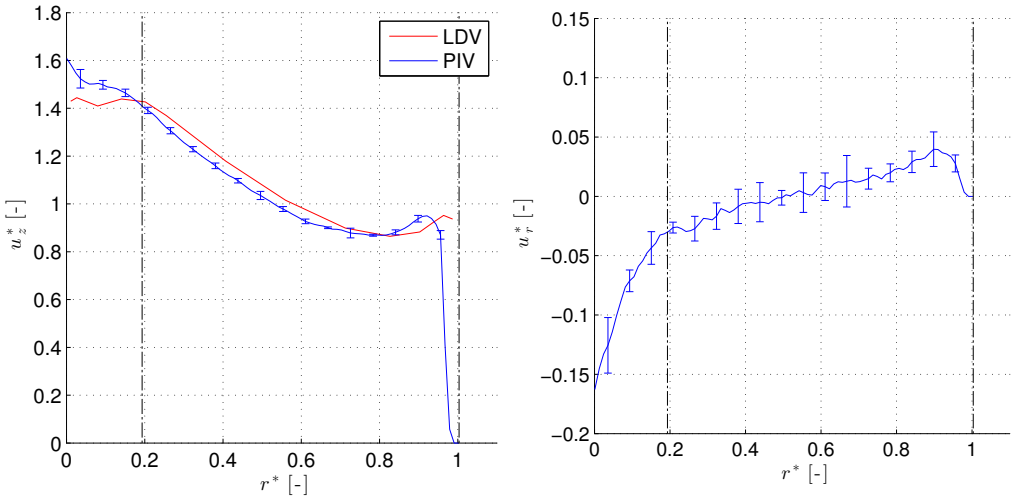

Figure 11. Axial (left) and radial (right) velocities at section I for HL operation. The red line shows the LDV result obtained by Sundström et al. [2] and the blue line shows the mean PIV results. The error bars indicate a 95% confidence interval. The dashed lines at $r^* = 0.19$ and $r^* = 1.00$ indicate the radial position of the runner hub corner and the draft tube entrance, respectively. Note the difference in scale on the ordinate axis.

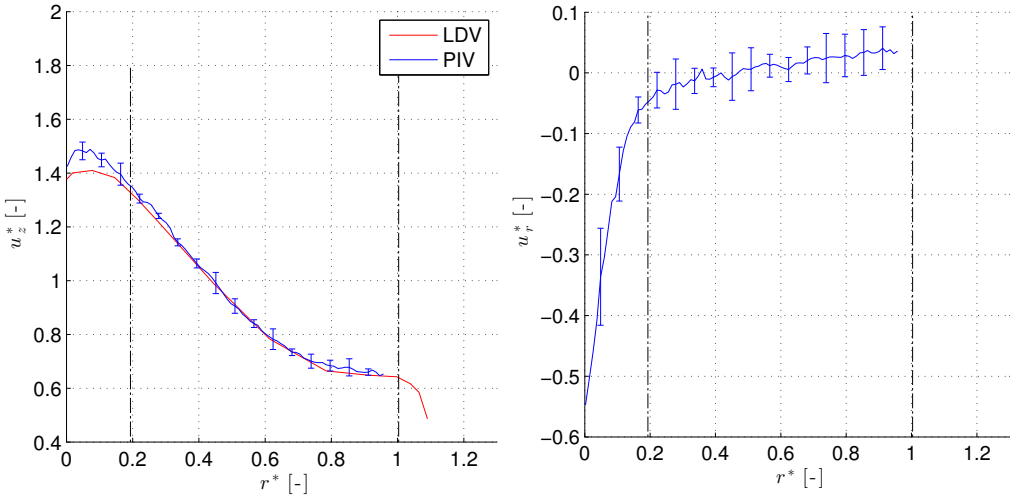

Figure 12. Axial (left) and radial (right) velocities at section II for HL operation. The red line shows the LDV result obtained by Sundström et al. [2] and the blue line shows the mean PIV results. The error bars indicate a 95% confidence interval. The dashed lines at $r^* = 0.19$ and $r^* = 1.00$ indicate the radial position of the runner hub corner and the draft tube entrance, respectively. Note the difference in scale on the ordinate axis.

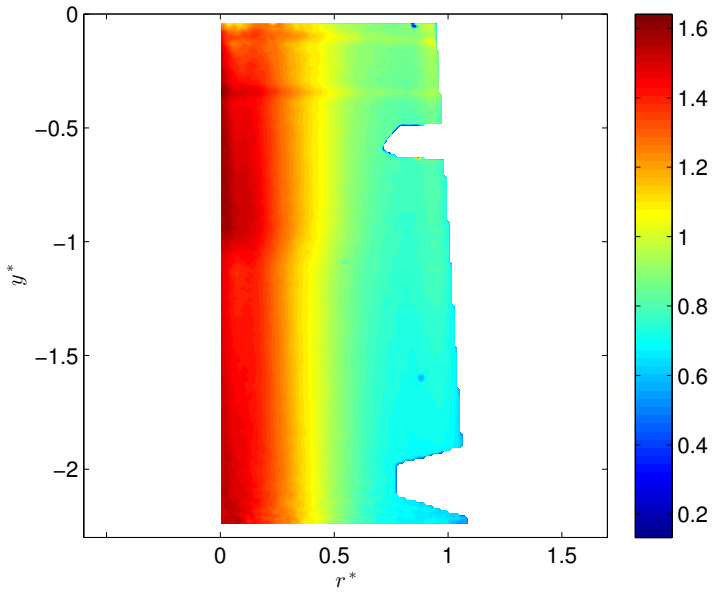

Figure 13. Contour plot of the meridional velocity within the PIV plane at HL. Pressure bolts in the draft tube cone are seen in both the upper and lower part of the cone.

5.3. PL results

Figure 14 shows the velocity profiles captured at section I while the turbine operates at the PL. The larger error-bars compared to the other operating points is attributed to the presence of the rotating vortex rope (RVR) formed in the draft tube at this operating point. The axial velocity profile at section I shows backward flow for $r^* < 0.7$. This is due to the recirculation bubble formed in the middle of the draft tube cone at this operating point. The low guide vane angle and the runner inability to extract the swirl generated by the guide vanes result in high swirl flow exiting the runner, see Sundström et al. [2]. The swirl results in a centrifugal force exerted on the flow. Hence, the axial velocity is significantly increased in the outer part of the draft tube cone for $r^* > 0.7$. The radial velocity at section I decreases with the radius. The positive radial velocity for $r^* < 0.5$ can be explained by the shape of the recirculation bubble region formed in the draft tube cone. The fact that the radial velocity is negative at $r^* > 0.5$ indicates that the flow does not follow the draft tube wall. The large pressure gradient in the radial direction close to the wall cause a negative radial velocity at this position, but it should be symmetric, i.e., the negative radial velocity should be seen close to the wall on the other side of the draft tube. This is not the case, as seen in Figure 17. This asymmetry could be caused by a local flow separation, which will propagate due to the high tangential velocity, see Sundström et al. [2]. Such a localized flow separation was not measured, but it could be the cause of the asymmetry in the radial velocity.

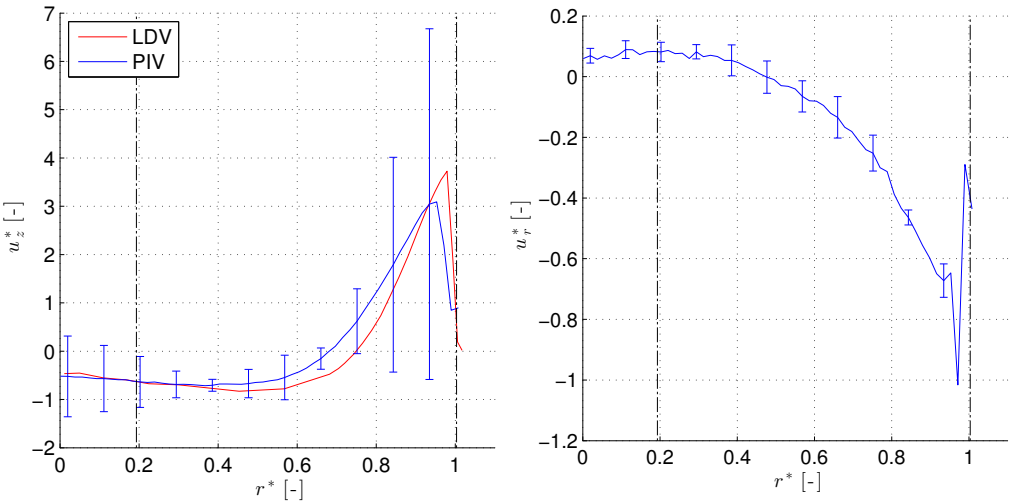

Figure 14. Axial (left) and radial (right) velocities at section I for PL operation. The red line shows the LDV result obtained by Sundström et al. [2] and the blue line shows the mean PIV results. The error bars indicate a 95% confidence interval. The dashed lines at $r^* = 0.19$ and $r^* = 1.00$ indicate the radial position of the runner hub corner and the draft tube entrance, respectively. Note the difference in scale on the ordinate axis.

The axial and radial velocity profiles at section II are presented in Figure 15. The main features of the velocity profiles are similar to the ones captured at section I. The axial velocity is monotonically increasing with the radius while the flow direction is downward for $r^* > 0.7$ and is upward for $r^* < 0.7$. The radial velocity decreases with the radius. Although the radial velocity is not measured close to the draft tube walls, the curve shows that the velocity should

be negative close to the wall, i.e., the flow does not follow the draft tube wall. It is expected that this will vary in the azimuthal position, as seen in Figure 17.

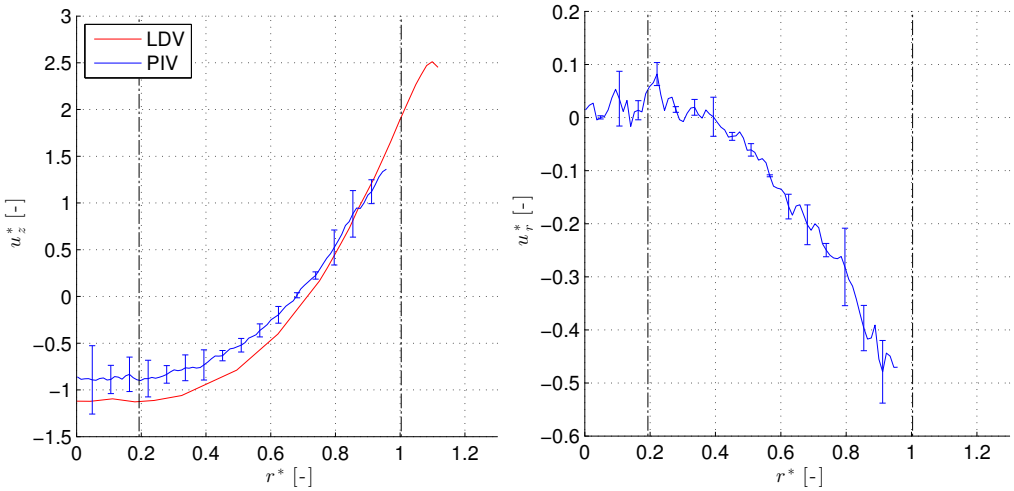

Figure 15. Axial (left) and radial (right) velocities at section II for PL operation. The red line shows the LDV result obtained by Sundström et al. [2] and the blue line shows the mean PIV results. The error bars indicate a 95% confidence interval. The dashed lines at $r^* = 0.19$ and $r^* = 1.00$ indicate the radial position of the runner hub corner and the draft tube entrance, respectively. Note the difference in scale on the ordinate axis.

Figure 16 presents the meridional velocity in the draft tube cone. Note the distinct dark blue lines of zero velocity at $r^* = 0.6$. Since the meridional velocity in this figure is a scalar value, the velocity will not be negative, but the zero-lines give an indication of the recirculation bubble in the draft tube cone.

Figure 17 presents contour of the axial velocity at PL. The figure shows the large recirculation region formed inside the draft tube cone. This recirculation region decreases the effective area of the draft tube cone affecting the turbines overall efficiency. Presented in Table 2, the turbine efficiency is decreased by about 20% at this operating point compared with the one at the BEP. The flow rate is about 1/3 of the one at BEP.

Figure 18 presents the contour plot of the radial velocity in the draft tube cone. The figure shows the asymmetry in the radial velocity distribution inside the draft tube cone. Moreover, the flow does not follow the right wall of the draft tube all along the draft tube cone as discussed before. The clear vertical line visualizes the asymmetry of the flow.

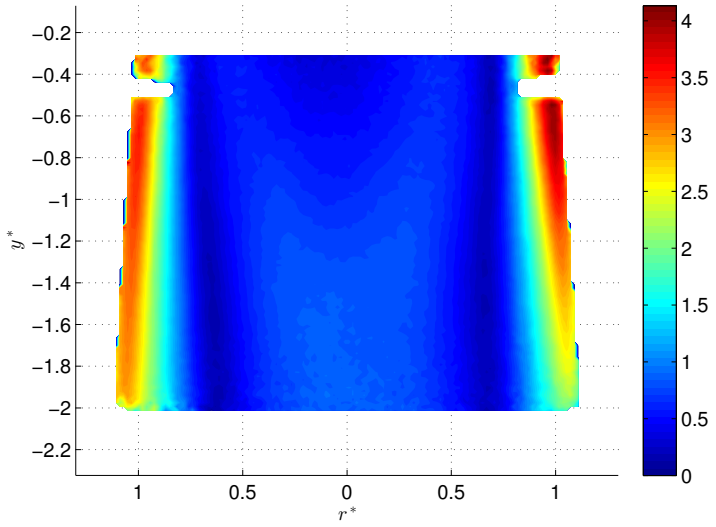

Figure 16. Contour plot of the meridional velocity within the PIV plane at PL operation. Pressure bolts in the draft tube cone are seen in both the upper part of the cone.

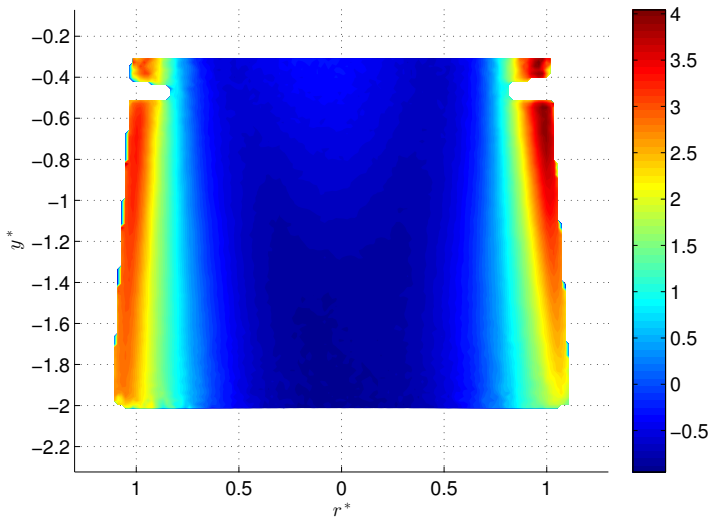

Figure 17. Contour plot of the axial velocity within the PIV plane at PL operation. Pressure bolts in the draft tube cone are seen in both the upper part of the cone.

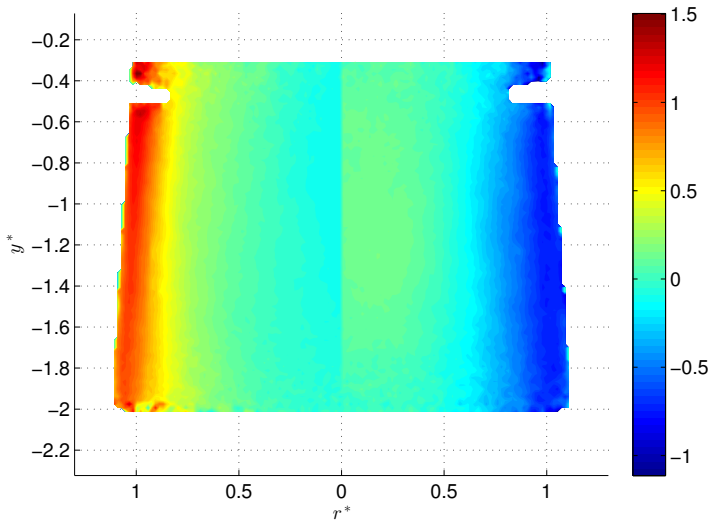

Figure 18. Contour plot of the radial velocity within the PIV plane at PL operation. Pressure bolts in the draft tube cone are seen in both the upper part of the cone.

6. Conclusions

PIV measurements have been performed on the francis-99 model turbine at the Waterpower Laboratory at the Norwegian University of Science and Technology. The results show good agreement with previously performed LDV measurements.

The measurements show discrepancies in the overlapping region between the measurement windows. Further measurements in the draft tube are needed in order to fully understand the reason. The non-zero radial velocity at the centerline of the draft tube cone indicate an asymmetry in the flow certainly due to a gyroscopic effect induced by the draft tube elbow on the swirl leaving the runner.

Appendix A. Operating point repeatability

Table A1. Maximum deviations in operating parameters for all operating points investigated.

	PL	**BEP**	**HL**
Axial Force	1.15 %	0.82 %	1.80 %
Axial force prototype	1.16 %	0.82 %	1.79 %
Differential Pressure	0.04 %	0.05 %	0.05 %
Dimensionless Axial force	1.16 %	0.80 %	1.77 %
Dissolved Oxygen	0.00 %	0.03 %	0.00 %
Flow	0.36 %	0.12 %	0.12 %
Flow prototype	0.37 %	0.14 %	0.13 %
Friction Torque	35.87 %	27.63 %	28.14 %
Generator Speed	0.01 %	0.02 %	0.01 %
Generator Torque	1.27 %	0.22 %	0.43 %
Guide Vane Opening Degree	0.00 %	0.00 %	0.00 %
Hydraulic Efficiency	0.25 %	0.14 %	0.17 %
Hydraulic efficiency prototype	0.24 %	0.14 %	0.17 %
Hydraulic Energy	0.38 %	0.08 %	0.10 %
Kinematic Viscosity	0.00 %	0.00 %	0.00 %
Mechanical Energy	0.13 %	0.12 %	0.21 %
Mechanical Effect prototype	0.12 %	0.12 %	0.20 %
n_{11}	0.03 %	0.01 %	0.03 %
n_{ED}	0.03 %	0.01 %	0.03 %
Nominal hydraulic efficiency model	0.25 %	0.14 %	0.17 %
NPSE	2.37 %	3.31 %	1.72 %
P_{11}	0.12 %	0.08 %	0.18 %
P_{ED}	0.13 %	0.08 %	0.18 %
Pressure Inlet	0.69 %	0.93 %	0.46 %
Pressure Inlet Sensor	0.63 %	0.79 %	0.52 %
Pressure inlet sensor abs	0.62 %	0.84 %	0.41 %
Pressure Outlet	1.95 %	2.75 %	1.38 %
Prototype Head	0.05 %	0.02 %	0.05 %
Q_{11}	0.37 %	0.15 %	0.14 %
Q_{ED}	0.37 %	0.14 %	0.14 %
Reynolds Number Model	0.63 %	0.63 %	0.65 %
Scalable loss	0.00 %	0.00 %	0.00 %
T_{11}	0.12 %	0.09 %	0.17 %
T_{ED}	0.13 %	0.10 %	0.18 %
Thoma number	2.38 %	3.30 %	1.75 %
Vapor Pressure	1.60 %	1.58 %	1.64 %
Water Density Inlet	0.01 %	0.01 %	0.01 %
Water Density Mean	0.01 %	0.01 %	0.01 %
Water Density Outlet	0.01 %	0.01 %	0.01 %
Water Head Model	0.05 %	0.05 %	0.05 %
Water Temperature	1.34 %	1.34 %	1.38 %

References

[1] Trivedi C, Cervantes M J, Gandhi B K and Dahlhaug O G 2013 *Journal of Fluids Engineering* **135** 111102–111102 ISSN 0098-2202

[2] Sundstrom J, Amiri K, Bergan C, Cervantes M J and Dahlhaug O G 2014 LDA measurements in the francis-99 draft tube cone *Proceedings of IAHR2014*

[3] Ciocan G D and Iliescu M S 2012 PIV measurements applied to hydraulic machinery: Cavitating and cavitation-free flows *The Particle Image Velocimetry - Characteristics, Limits and Possible Applications* ed Cavazzini G (InTech) ISBN 978-953-51-0625-8

[4] Aeschlimann V, Beaulieu S, Houde S, Ciocan G D and Deschênes C 2013 *European Journal of Mechanics - B/Fluids* **42** 121–128 ISSN 09977546

[5] Iliescu M S, Ciocan G D and Avellan F 2002 3d PIV and LDV measurements at the outlet of a francis turbine draft tube *ASME 2002 Joint US-European Fluids Engineering Division Conference* (American Society of Mechanical Engineers) pp 311–316

[6] Amiri K 2014 *An experimental investigation of flow in a Kaplan runner steady-state and transient* Licentiate Luleå University of Technology

---

Paper 2

Experimental Investigation of a High Head Model Francis Turbine During Steady-State Operation at Off-Design Conditions

Bergan, C. W., Goyal, R., Cervantes, M. J., Dahlhaug, O. G.

IOP Conference Series: Earth and Environmental Science vol. 49, 2016

Experimental Investigation of a High Head Model Francis Turbine During Steady-State Operation at Off-Design Conditions

Carl Bergan[1], Rahul Goyal[2,3], Michel J Cervantes[1,3] and Ole G Dahlhaug[1]

[1] Department of Energy and Process Engineering, Waterpower Laboratory, Norwegian University of Science and Technology, Trondheim, Norway
[2] Department of Mechanical and Industrial Engineering department, Indian Institute of Technology, Roorkee 247667
[3] Department of Engineering Science and Mathematics, Luleå University of Technology, Luleå, Sweden

E-mail: carl.w.bergan@ntnu.no

Abstract. Francis-99 is a set of workshops aiming to determine the state of the art of high head Francis turbine simulations (flow and structure) under steady and transient operating conditions as well as promote their development and knowledge dissemination openly. The first workshop (Trondheim, 2014) focused on steady state conditions. Some concerns were raised regarding uncertainty in the measurements, mainly that there was no clear vortex rope at the Part Load (PL) condition, and that the flow exhibited relatively large asymmetry. The present paper addresses these concerns in order to ensure the quality of the data presented in further workshops.

To answer some of these questions, a new set of measurements were performed on the Francis-99 model at Waterpower Laboratory at the Norwegian University of Science and Technology (NTNU). In addition to PL, two other operating conditions were considered, for further use in transient measurements, Best Efficiency (BEP) and High Load (HL). The experiments were carried out at a head of 12 m, with a runner rotational speed of 333 revolutions per minute (rpm). The guide vane opening angle were 6.72°, 9.84° and 12.43° for PL, BEP and HL, respectively. The part load condition has been changed from the first workshop, to ensure a fully developed Rotating Vortex Rope (RVR). The velocity and pressure measurements were carried out in the draft tube cone using 2D PIV and six pressure sensors, respectively. The new PL condition shows a fully developed rotating vortex rope (RVR) in both the frequency analysis and in the phase resolved data. In addition, the measurements confirm an asymmetric flow leaving the runner, as was a concern in the first Francis-99 workshop. This asymmetry was detected at both design and off-design conditions, with a stronger effect during off design.

1. Introduction

Hydropower, being a regulated renewable energy source, is put under increasing demand to ensure a stable supply of energy. Large quantities of intermittent power sources (sun, wind, ocean wave etc.) calls for a larger amount of regulated power, while the environment calls for more renewable energy. This drives the turbines to be operated outside of their design range [1]. This operation leads to undesirable flow phenomena, which can be difficult to predict.

Phenomena such as power swings, caused by low-frequency pressure pulsations, vibration which leads to shorter lifetime for the runner, flow recirculation which lowers the runner's hydraulic efficiency. These phenomena can be difficult to predict at the design stage, and it is desirable to understand the cause and full consequences of these issues in order to mitigate them. For this, better tools in CFD are required. In performing CFD, it can be difficult to know if the results are indeed correct, particularly at part load operation, where turbulent phenomena become quite dominating [2]. While providing ample results to analyse further, CFD still lacks validation in hydropower. Francis 99 is a workshop aiming at providing the validation needed to see if the CFD provides the correct results. During the first workshop, many of the participants were able to reproduce measured phenomena with their simulations. However, there were some phenomena which the participants were unable to capture with CFD, which require experimental revaluation. Additionally, several concerns have been raised about the experimental work submitted to the previous Francis-99 workshop, so the goal of this paper is to assess those concerns, while providing supplementary experimental data.

2. Materials and Methods

The measurements were performed in the Waterpower Laboratory at NTNU, on the Francis-99 runner. The Francis-99 runner is a 1:5.1 scaled model of a prototype in a Norwegian power plant called Tokke. The turbine consists of a spiral casing with 14 stay vanes, 28 guide vanes, and a runner with 15 full-length blades and 15 splitter blades, for a total of 30 runner blades. The measurements were performed at three operating points: Part Load (PL), the Best Efficiency Point (BEP) and High Load (HL). The specifics of these operating points are given in table 1

Table 1: Description of the operating points

Operating Point	Head H [m]	Flow Rate Q [m^3/s]	Specific speed n_{ED} [-]	Specific flow Q_{ED} [-]	Hydraulic efficiency η [-]
PL	11.87	0.140	0.179	0.106	0.901
BEP	11.94	0.200	0.179	0.152	0.924
HL	11.88	0.242	0.179	0.184	0.917

The operating conditions are inspired by the operating conditions presented in Francis99(I) [3], but with some changes. Since the goal is to perform realistic transient measurements, the operating points have been changed to have the same RPM for all operating conditions. Additionally, the part load operating condition has been changed in order to capture a more fully developed Rotating Vortex Rope. In order to maintain some similarity to the operating points presented in Francis 99 (I), the value for n_{ED} was maintained constant for the BEP condition. The measurements were performed in an open loop configuration, shown in figure 1

The measurements with PIV is based on the analysis of two successive images of the target area seeded with micro-sized particles that follow the flow and that are illuminated with a laser sheet provided by double-pulsed laser [4]. The PIV measurements have been performed in the draft tube with a TSI 2-D system. Draft tube are made of transparent Plexiglas's to allow the laser sheet and to capture the successive images in the flow domain. The pulsed light sheet with a thickness of approximately 3 mm, is generated by two Nd:YAG PIV laser (Maximum frequency=50 Hz) with dual cavity performing 100 mJ by pulse. The wavelength is 532 nm.

The lightning field is visualized by a low noise digital CCD camera (VC-4MC-M180) of 2400x2400 pixel resolution, with a succession of paired images at 300 µs to 400 µs. The camera

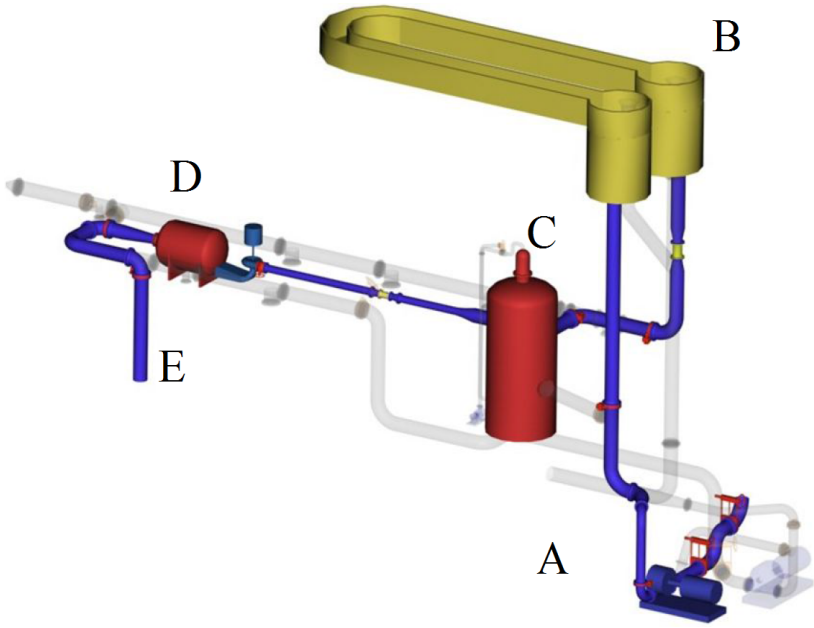

Figure 1: Open loop test rig. The water is pumped from the lower reservoir (A) to the upper reservoir (B). The channel between the two overhead tanks in (B) ensure that the pump and turbine are hydraulically separated. The overhead tanks are fitted with overflow pipes, to ensure a constant upstream water level. The water then enters the pressure tank (C), which will act as an air cushion chamber. The water then passes through an electromagnetic flowmeter before entering the turbine. After leaving the turbine, the water enters the draft tube tank, where an overflow wall maintains the downstream water level. Finally, the water leaves the downstream tank, returning to the lower reservoir (E)

resolution is 2032 x 2048 pixels for a 276.0 x 278.0 mm^2 spatial domain.

TSI seeding particles with a density of 1.016 g/cm^3, refractive index 1.52 and mean diameter of 55 µm were used for the measurements. Since the camera is capable to capture the image in pixel displacement, a magnification factor (α) or mathematical constant is required to covert the pixel imaging chip to a physical distance in real space. Due to the conical shape of the draft tube and coupled different angle of refraction a correction in optical distortion is required. To minimize the optical distortion, an index matching box (refractive index 1.52) made of glass filled with water, was used during the calibrations and measurements to decreases the light aberration during the PIV measurements. The ex-situ calibration was performed in the draft tube due to practical limitations associated with the in-situ calibrations. A specially designed 2-D target plate with the dots having the diameter of 2 mm and space between the dots is 20 mm was placed inside the draft tube to compensate the light aberration as shown in Figure 2.

The aberration will still exists close to the areas of high curvature i.e., close to the draft tube wall. As seen in the figure 2 (left) there is distance between the draft tube wall and the first calibration point. Hence, the calibration results are extrapolated close to the wall. Moreover, the picture is warped significantly close to the wall but unaffected along the cone centerline. Thus, the calibration matrix calculated may be subject to the some uncertainties close to the

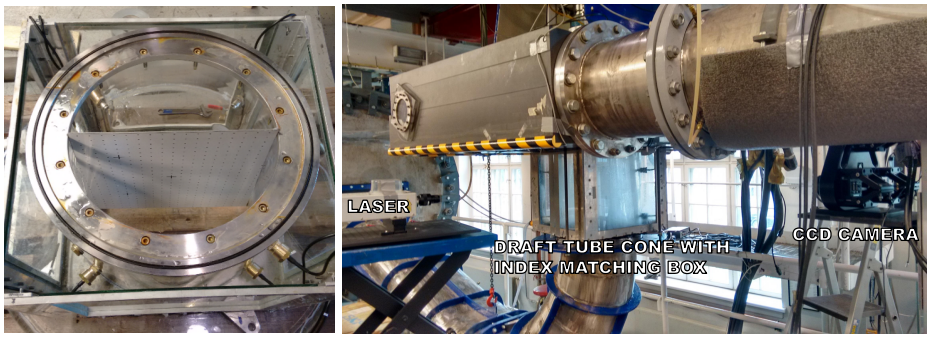

Figure 2: Calibration setup

wall. Therefore, calibration and measurement plane was selected few mm away from the draft tube walls to avoid the aberration as shown in Figure 3. The target plate was placed in the respective measurement plane and photographed by the camera of the PIV system. During the calibration the camera is exactly at the same position as later in the measurements. The images were recorded at a rate of 40 Hz. 2400 paired images for 60 s were captured at the measurement section. Number of images were selected on the basis of required convergence images for steady-state operation. So that the complete convergence in steady-state data before and after the transition in transient operation can be achieved.

The measurement section, along with the pressure sensor placement is shown in Figure 3.

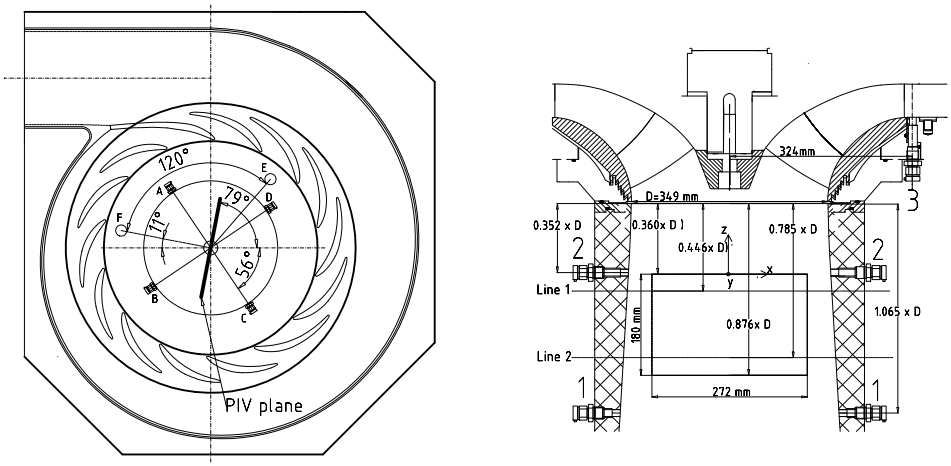

Figure 3: Sensor placement as seen from top (left) and from the side (right). The sensors corresponding to the numbers are shown in table 2

The position of the individual pressure sensors is shown in Table 2.

The pressure measurements were recorded using a National Instruments (NI) Compact Reconfigurable Input/Output (cRIO) Model 9074 with a 24 bit analog to digital converter (ADC). The data was recorded at 5 kS/s with a separate ADC for each channel. The regular

Table 2: Position of the draft tube pressure taps

Sensor	Placement	Type
DT1	1A	Kistler
DT2	1B	Kistler
DT3	1C	Kistler
DT4	1D	Kistler
DT5	2B	Kistler
DT6	2D	Kistler
VL1	3E	Kulite
VL2	3F	Kulite

test rig instrumentation yields values for flow, head, generator torque and runner frequency. In addition to the base instrumentation of the test rig, six pressure taps were mounted on the draft tube cone, and two in the vaneless space as shown in Figure 3.

3. Results and Discussion

As mentioned before, the PL operating condition used in the first Francis-99 workshop was infeasible to perform simulations on. The participants called for a different PL operating point, with a more clearly defined vortex rope.

Figure 4 shows the Fast Fourier Transform (FFT) results from the draft tube pressure sensors at PL operation.

A new operating condition was therefore chosen for part load, with the restriction of having the same rotational speed as the BEP and HL operating conditions. The amplitude of the RVR frequency was used as a guide for choosing a suitable part load operating point. The results show a strong rotating vortex rope at 1.633 Hz (corresponding to $0.294 f_n$), with both the 2nd and 3rd harmonic present. In addition, some noticeable oscillations can be observed at 15.8 Hz and 41.8 Hz, for all the sensors. Assuming the speed of sound in the pipe system to be 1100 m/s, the estimated frequency for a standing wave is approximately 15.6 Hz between the runner and the pressure tank, and 39.3 Hz between the runner and the draft tube tank. Due to the uncertainty in estimating the speed of sound in the pipe system, it is reasonable to assume that the signals at 15.8 Hz and 41.8 Hz are standing waves. Decomposing the pressure signals from the draft tube cone into its rotating and plunging components yields the results shown in Figure 5

Since the 15.8 Hz and 41.8 Hz frequencies are present only in the synchronous portion of the signal, they are considered to be standing waves.

3.1. Phase resolved vortex rope

The data can be reduced into three components using Reynolds triple decomposition: the time-averaged velocity, $\overline{\phi}(x)$; oscillatory part, $\widetilde{\phi}(x,t)$; and the random fluctuations, $\phi'(x,t)$. This decomposition is shown in Equation 1 [5]

$$\phi(x,t) = \langle \phi(x,t) \rangle + \phi'(x,t) = \overline{\phi}(x) + \widetilde{\phi}(x,t) + \phi'(x,t) \tag{1}$$

By phase resolving the signal for a chosen frequency, and placing the data in phase-averaged bins, cyclic phenomena which may even be of higher frequency than the measurement's Nyquist frequency become evident. This is shown in Figure 6, where the PIV measurement during Part load is sampled at one point in the measurement section, and phase resolved with the runner

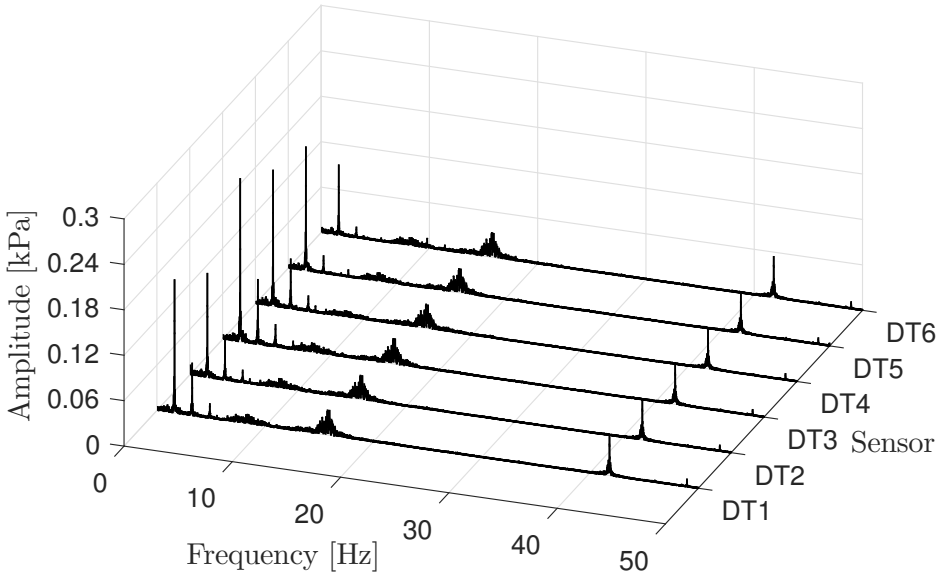

Figure 4: Waterfall diagram of the PL operation. Note the small peak at 16 Hz, and the sharper peak at 42 Hz. These are thought to be standing waves in the inlet and outlet pipe, respectively.

frequency. Applying this method for multiple points along the radius yields the figure shown in Figure 6, right.

Phase resolving the data with respect to the RVR frequency clearly shows that there is indeed a fully developed rotating vortex rope in the flow, shown in Figure 7.

The new part load condition can therefore be used for further measurements and simulations on the Francis 99 workshops.

3.2. Velocity profiles

The axial velocity profiles for BEP and PL are shown in Figure 8. Both operating points show signs of asymmetry, which can also be seen in the radial velocity profile. This point was raised at the first Francis-99 workshop. Multiple repetitions were performed for each operating point in order to firmly establish the measurement uncertainty.

Both the axial and the radial velocities show signs of asymmetry. This is most likely due to the gyroscopic effect introduced by the draft tube elbow, in addition to an uneven distribution of water in the spiral casing. The measurements were performed near the middle of the draft tube cone, in order to better capture the asymmetric flow.

The asymmetry at BEP is shown in Figure 9. The difference in mean axial velocity over the centerline of the draft tube cone varies with operating point and with vertical position in the draft tube cone. For BEP, the difference in axial velocity is 3.7% in the upper line, and 10.7% in the lower line. For PL, the difference is 64.2% in the upper line, and 67.1% in the lower line. The relative difference in PL appears to be very large, but this is due to the bulk velocity being quite low at this operating condition. Nevertheless, it shows that the flow is

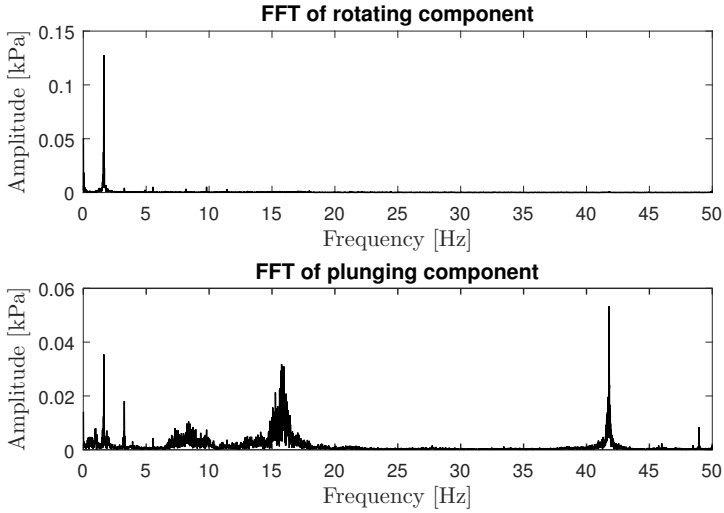

Figure 5: FFT analysis of the rotating and plunging components at the PL operating condition

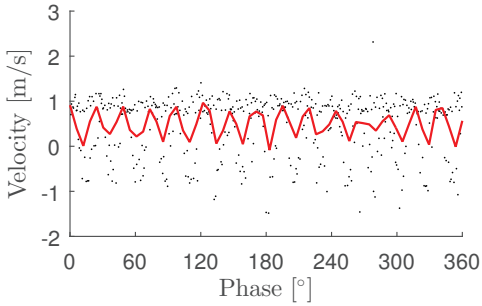

(a) Phase resolved velocity for one point in space r^* =0.51. The bin size is 6 degrees, and the number of samples per bin is approximately 100. The red line indicates the mean value within each phase bin, while the black dots are all the measured velocities.

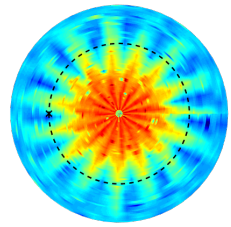

(b) Phase resolve performed for the whole measured cross section. The location of the point investigated in the left figure is indicated with the black marker.

Figure 6: Velocity measurements phase resolved with respect to the runner frequency, sampled at PL operation. The velocity is sampled at 0.59xD downstream the draft tube inlet. The velocity component shown in this figure is the axial velocity.

becoming increasingly asymmetric in the flow direction. The asymmetry is large, and increasing in the stream direction for all operating conditions. This indicates that the asymmetric flow is indeed originating from the gyroscopic effect of the draft tube elbow. In addition to exhibiting significantly asymmetric flow, the PL operating condition shows signs of a recirculation zone with negative axial velocity. In the PL velocity profile, shown in figure 8, the axial velocity is nearly zero close to the draft tube center, even though this is some distance downstream the draft tube inlet. In addition to that, the RVR exhibits a large internal region of negative

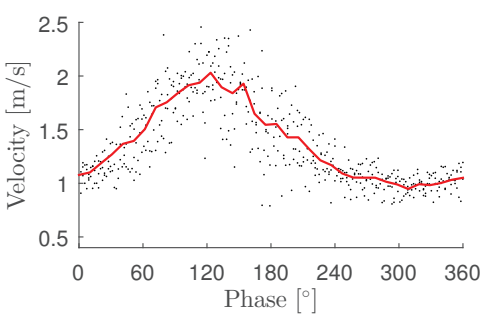

(a) Phase resolved velocity for one point in space r^* =0.22. The bin size is 10 degrees, and the number of samples per bin is approximately 100. The red line indicates the mean value within each phase bin, while the black dots are all the measured velocities.

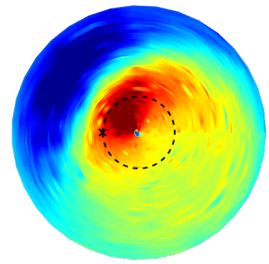

(b) Phase resolve performed for the whole measured cross section. The location of the point investigated in the left figure is indicated with the black marker.

Figure 7: Velocity measurements phase resolved with respect to the RVR frequency, sampled at PL operation. The velocity is sampled at 0.59xD downstream the draft tube inlet. The velocity component shown in this figure is the axial velocity.

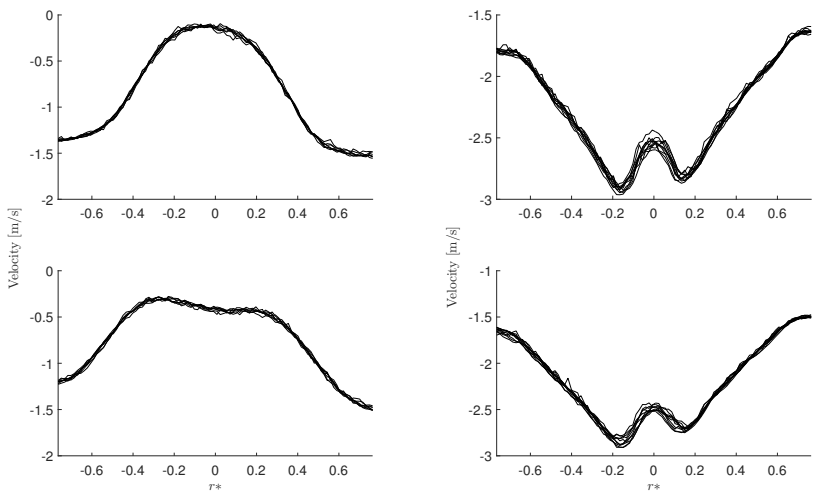

(a) PL axial velocity

(b) BEP axial velocity

Figure 8: Axial velocity profiles. The upper graphs depict the velocity at Line 1, while the lower graphs depict the velocity at Line 2, as shown in Figure 3. r^* is the dimensionless radius, obtained by reducing the radius at the measurement location with the radius at the draft tube inlet. Note that the velocity is not symmetric about the centerline, and that this asymmetry gets relatively larger for the lower graphs.

axial velocity, indication a large internal recirculation in the RVR. These effects combined are significant in reducing runner efficiency at PL operation.

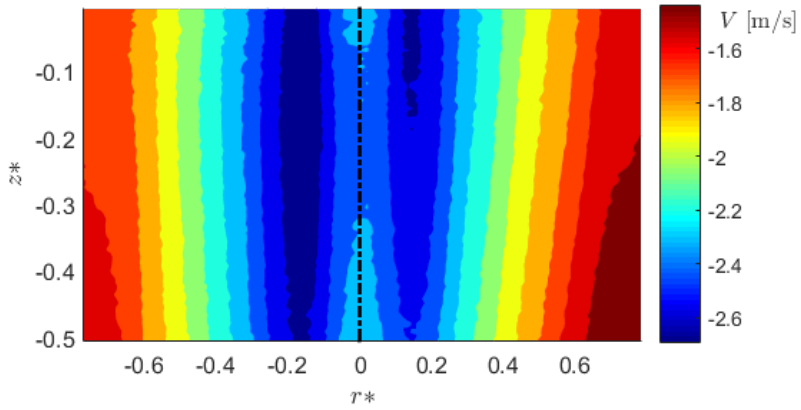

Figure 9: BEP asymmetry. The dashed line indicates the centerline of the draft tube cone. In this measurement, the mean difference in axial velocity over the centerline is approx. 7.6%, with a higher axial velocity on the left side of the centerline. r^* is the dimensionless radius, obtained by reducing the radius at the measurement location with the radius at the draft tube inlet.

4. Conclusions

The new part load condition exhibits a clear vortex rope with internal recirculation, and is therefore considered to be appropriate for further simulation during the coming Francis 99 workshops. The Vortex rope can be seen in the velocity data through both frequency analysis and phase resolving. Additionally, the runner blade wakes are clearly visible in the phase resolved results, but the splitter blades are not evident in the velocity data. This indicates a good mixing of the channel flows in the runner downstream the splitter blades. The results show that the part load condition has a strongly developed rotating vortex rope, consisting of both rotating and plunging components. The FFT also reveals a clear standing wave in the results, something that could be captured with CFD, if desired. The flow exhibits a relatively high degree of asymmetry, yielding a difference in axial flow of 10.7% for BEP and 67.1% for PL. The asymmetry is increasing in the flow direction, becoming more significant near the draft tube elbow.

References

[1] C. Trivedi, B. Gandhi, and C. J. Michel. "Effect of transients on Francis turbine runner life: a review". en. In: *Journal of Hydraulic Research* 51.2 (Apr. 2013), pp. 121–132.

[2] Z. Yaping et al. "Performance study for Francis-99 by using different turbulence models". In: *Journal of Physics: Conference Series* 579 (Jan. 2015), p. 012012.

[3] C. Bergan et al. "Preliminary Measurements of the Radial Velocity in the Francis-99 Draft Tube Cone". In: *Journal of Physics: Conference Series* 579 (Jan. 2015), p. 012014.

[4] M. Raffel et al. *Particle Image Velocimetry A Practical Guide*. English. Berlin, Heidelberg: Springer-Verlag Berlin Heidelberg, 2007.

[5] K. Amiri. "An experimental investigation of flow in a Kaplan runner steady-state and transient". Licentiate. LTU, 2014.

Paper 3

Experimental Investigation on a High Head Model Francis Turbine during Load Rejection

Goyal, R., Bergan, C. W., Cervantes, M. J., Gandhi, B. K., Dahlhaug, O. G.

IOP Conference Series: Earth and Environmental Science vol. 49, 2016

Experimental investigation on a high head model Francis turbine during load rejection

R Goyal[1, 3], C Bergan[2], M J Cervantes[2, 3], B K Gandhi[1] and O G Dahlhaug[2]

[1] Indian Institute of Technology Roorkee, Roorkee, 247667 Roorkee, India

[2] Waterpower Laboratory, Norwegian University of Science and Technology, Alfred Getz vei 4, 7034 Trondheim, Norway

[3] Department of Eng. Sci. and Math, Luleå University of Technology, 97187 Luleå, Sweden

E-mail: goel.rahul87@gmail.com

Abstract. Francis-99 is a set of workshop aiming to determine the state of the art of high head model Francis turbine simulations (flow and structure) under steady and transient operating conditions as well as to promote their development and knowledge dissemination openly. The first workshop (Trondheim, 2014) was concerned with steady state operation. The second workshop will focus on transient operations such as load variation and start-stop. In the present work, 2-D particle image velocimetry (PIV) with synchronized pressure measurements performed in the draft tube cone of the Francis-99 test case during load rejection is presented. Pressure sensors were mounted in the vaneless space and draft tube cone to estimate the instantaneous pressure fluctuations while operating the turbine from the best efficiency point (9.8°) to part load (6.7°) with the presence of a rotating vortex rope (RVR). The time-resolved velocity and pressure data are presented in this paper showing the transition in the turbine from one state to another.

1. Introduction

The penetration of the electricity generated from the solar and wind has raised significant concern about the grid stability [1]. The hydropower power plant is used to balance the grid parameters because of the speedy and smooth response to grid network of the hydraulic turbines. Therefore, turbines have to sustain transient phenomena's such as load variation and start-stop. This leads to the unsteady pressure pulsation and development of complex flow in the runner, vaneless space, and draft tube [2- 3]. Reduced scale mode testing and computational fluid dynamics (CFD) are the main tools for design and analysis of turbine. Increased computational capacities and coupling of flow parameters have given more importance to CFD in order to investigate the complexity of the flow in the turbine [4, 5]. The extensive amount of measurements on both prototype and reduced-scale model Francis turbine had been performed to investigate these instability [2, 6-9]. A set of workshops (Francis-99) have been planned to provide an open access of the complete design and data of model Francis turbine during steady and transient operations. The main objective of the workshop was to evaluate the numerical techniques applied to investigate the hydraulic turbines and develop an open platform to the researchers for conducting numerical studies in high head turbines. The first workshop (Trondheim, 2014) was concerned with steady operation [10]. A total of 14 research papers were presented. The second workshop will be a continuation of the first workshop with new steady state operating conditions. There will also be a focus on the simulation of the flow during transient operation such as load variation and start-stop. In order to prepare the second workshop, 2-D particle image velocimetry (PIV) and pressure measurements were performed in the draft tube cone of the Francis-99 test case during load rejection (best efficiency point to part load), load acceptance (best efficiency point to high load), and start-stop. These data are available on the workshop website (https://www.ntnu.edu/nvks/francis-99). In the present work, detailed investigation of load rejection will be presented. The aim of the present study is to investigate the unsteady flow pattern and pressure pulsation inside the draft tube during load rejection. The motivation behind the study is to create a good quality data base in order to understand the consequence of the transient operations and validate future transient simulations of the investigated

model. This may allow with time to develop new guide vanes operating strategy to minimize the dynamic instability in the Francis turbine.

2. Material and Method

2.1. Model test rig

A scale (1:5.1) model of a prototype Francis turbine has been selected for the present investigation. The model turbine is installed at the Water Power Laboratory, Norwegian University of Science and Technology (NTNU), Norway. The prototype turbine (Head =377 m, Power =110 MW, and Runner diameter =1.779 m, Discharge = 31 m^3s^{-1}, Specific speed=0.27) is in operation at Tokke power plant, Norway. A schematic of the test rig is presented in Fig.1. Water from the basement was pumped to the overhead tank which flowed down to the upstream pressure tank connected to the turbine inlet. A uniform level of the water was maintained in the overhead tank. The draft tube was connected to the downstream tank, which was open to the air, and the water was released back to the basement. The model is integrated with 14 stay vanes conjoined inside the spiral casing, 28 guide vanes, a runner with 15 splitters and 15 full length blades, and an elbow-type draft tube. At the inlet pipeline, two pressure transmitters, PTX1 and PTX2 were mounted at 4.87 m and 0.87 m upstream of the turbine inlet, respectively. A magnetic flow meter was used to measure the turbine discharge and a differential pressure transducer was used to acquire the pressure difference across the turbine.

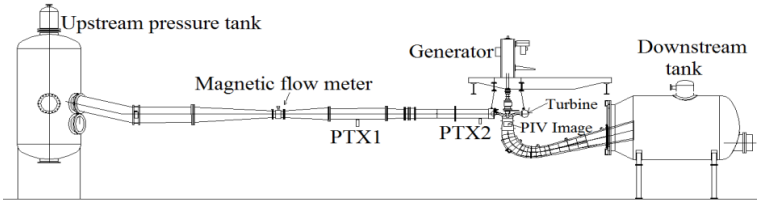

Figure.1 Test rig of the model Francis turbine

2.2. Pressure and velocity measurements , Instrumentation, and Calibration

The instrumentation, calibration, measurements procedure, and data analysis were carried out according to the guidelines available in IEC 60041[11], IEC 60193[12], and ASME PTC 18 [13]. The pressure measurements were recorded using a National Instruments (NI) Compact Reconfigurable Input /Output (cRIO) Model 9074 with a 24 bit analog to digital converter (ADC). The data were sampled at 5 kHz for each channel. The operating and flow parameters such as discharge, turbine inlet and differential pressure, atmospheric pressure, the angular speed of the runner, shaft torque to the generator, bearing friction torque, turbine axial force, and guide vanes angular position were acquired through the same acquisition system. In addition to the base instrumentation of the test rig, six pressure sensors (Kistler-701A, 0-25 bar) were mounted in the draft tube cone and two pressure sensors (Kulite-Druck PTX 1830, 0-10bar) were mounted in the vaneless space, one near the beginning of the spiral casing and one near the end as shown in Fig. 2 and Table 1. The estimated uncertainties were below 0.01%, for the vaneless space sensors (VL1 and VL2), and draft tube sensors. The estimated uncertainties were below 0.02% for the inlet pipe transducer (PTX1 and PTX2). The total estimated uncertainty was ± 0.15% for the hydraulic efficiency under the steady-state operating condition of BEP.

PIV measurements have been performed in the draft tube with a 2-D PIV system (TSI). The draft tube cone is made of transparent Plexiglas to allow optical access to the flow domain. The pulsed light sheet with a thickness of ~3 mm, was generated by two Nd: YAG PIV laser (maximum frequency=50 Hz) with dual cavity performing 100 mJ by the pulse. The wavelength was 532 nm. The laser was placed on a hydraulic table, in order to provide the vertical movement with minimal horizontal and lateral shift. The lightning field was visualized by a low noise digital charge coupled device (CCD) camera (VC-4MC-M180) of 2048 x 2048 pixel resolution, with a succession of paired images at 300-400 µs. The

camera resolution is 2032 x 2048 pixels for a 276.0 x 278.0 mm^2 spatial domain. The camera was placed on a lightweight traverse table (Dantec), in order to provide a reliable and repeatable camera movement. Seeding particles (TSI, polyamide 12) were used: particle density of 1.016 g/cc, refractive index 1.52 and mean diameter of 55 µm. To minimize the optical distortion, an index matching box (refractive index 1.52) made of glass filled with water, was used for the calibrations and measurements to decrease the light aberration during the PIV measurements. The ex-situ calibration was performed in the draft tube due to practical limitations associated with the in-situ calibrations. A specially designed 2-D target plate with dots having a diameter of 2 mm and spaced every 20 mm was placed inside the draft tube for calibration. During the calibration, the camera is at the same position as during the measurements. A sensitivity analysis test with different sampling rate was performed. It was found that at an acquisition frequency of 40 Hz, the light intensity inside the cone was enough for capturing clear images with CCD camera. 2400 paired images were captured for 60 s at the measurement section.

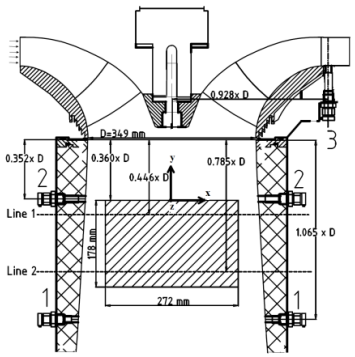

Figure 2 (a). Drawing of the model Francis turbine from side

Table1. Position of pressure sensors

Senso	Placemen	Type
DT1	1A	Kistle
DT2	1B	Kistle
DT3	1C	Kistle
DT4	1D	Kistle
DT5	2B	Kistle
DT6	2D	Kistle
VL1	3E	Kulite
VL2	3F	Kulite

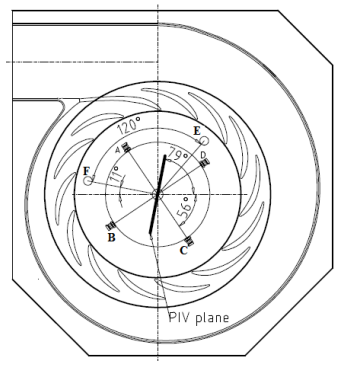

Figure 2(b). Drawing of the model Francis turbine from top

Figure 2. Sensor placement as seen from above Fig. 2(a) from side and Fig. 2(b) from the top. Note that the vaneless sensor taps are 120 degrees apart. All dimensions are in mm. The sensor denomination and their placement are shown in Table 1.

2.3. Measurement program

Both steady-state and transient measurements were performed on the model Francis turbine. The operating conditions were inspired by the operating conditions presented in Francis 99 workshop-I, but with some changes. Since the aim was to perform realistic transient measurements, therefore, the new operating points have the same runner revolutions per minute (RPM) at all operating conditions to achieve the realistic condition as of prototype. The maximum hydraulic efficiency of 92.4 % was found under the steady state condition at α = 9.8°, n_{ED} = 0.18, and q_{ED} = 0.15, marked as best efficiency point (BEP). Additionally, the part load (PL) operating condition has been changed in order to obtain a clear rotating vortex rope (RVR) pulsation in the draft tube. All the measurements were performed in an open loop configuration to get realistic conditions without significant variation of the effective head available to the turbine inlet similar to prototype. The specification of steady-state operating points is presented in Table 2.

Table 2. Operating points

Operating Point	Guide-vane angle (°)	Head (m)	Flow rate (m^3/s)	Hydraulic efficiency (-)
PL	6.7	11.87	0.140	0.90
BEP	9.8	11.94	0.200	0.93

The transient measurement was carried for load rejection by changing the angular position of the guide vanes from 9.8° (BEP) to 6.7° (PL). The maximum angular movement of the guide vanes is 14° (Full Load). Guide vanes are always operating against the acting pressure or hydrodynamic forces. Hence, there may be some difference between the angular position recorded and the actual position of about ±0.044°. The angular position of 6.7° (48%) is the lowest guide vanes angle for the load variation and 14° (100%) is the maximum opening (PM ≈ 30 kW) for the head of 12.5 m used in this study. The generator was operated at n_{ED} = 0.18 during the transient measurements, where flow rate and output power were managed by operating the guide vanes.

2.4. Data analysis for synchronized pressure and velocity measurements

There was a variable time delay for the PIV between receiving a trigger signal, and starting acquisition. In order to determine this time delay, a small light-emitting diode (LED) was placed on the edge of the PIV image frame, and the powering signal for this LED was recorded on the cRIO. The first image with LED-off was recorded manually in all the PIV measurements. A Matlab function was created in order to calculate the time delay between pressure and PIV measurements. The variation of the time delay was the order of seconds, verifying the need for the LED as a synchronization mechanism. Later, the LED was masked out in the processing of the images. The guide vanes movement was operated by a computer-controlled relay, taking both the guide vanes angle and the runner positions from transistor – transistor logic (TTL) as inputs. This ensured that the guide vanes movement began at the same runner position for all the transient repetitions. The commercial PIV software, INSIGHT 4G, from TSI was used for image processing and PIV data analysis. Cross-correlation scheme with smaller (32x32 pixels) spots with two refinement steps and 50 % overlap between the adjacent windows was applied on the acquired data after performing the 2-D calibration. A masking was applied in the processing to remove the unilluminated portion of the image from the processing step. Therefore, 272 x 178 mm^2 area was processed for obtaining the velocity vector field in the draft tube cone. Spectral analysis of the pressure and velocity data were performed to find out the dominant frequencies of the flow and their physical sources. The spectral analysis was performed with Welch's method and applying the Hanning window on the fluctuating part (see Eq.1) of the pressure and velocity data after applying the calibration results to the raw signals.

$$\hat{S}(t) = S(t) - \bar{S} \tag{1}$$

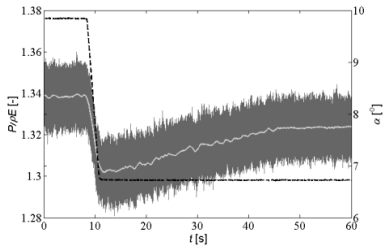

(a) VL1

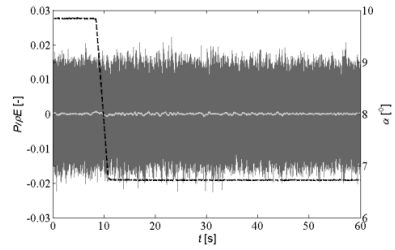

(b) VL1 fluctuating part

Figure 3 (a). Raw and mean pressure signal from the sensor mounted in the vaneless space (VL1) during load rejection from BEP to PL, **3(b).** The fluctuating part of the vaneless sensor (VL1) signal during load rejection from BEP to PL (grey lines: instantaneous pressure , white line : smoothed pressure signal, black dashed line : guide vane angle).

The smoothing of the transient data was carried out using Savitzky-golay filter in Matlab [2]. Subtraction of the smoothed signal from the original one gives the fluctuating part of the signal during the transition; it is used for the frequency analysis. A polynomial of order 2 with a frame size of 1 s was selected as the input parameters for the smoothing function. Figure 3 (a) shows the variation in the signal

of the pressure sensor located at vaneless space (VL1) together with the guide vanes angle variation during load rejection from BEP to PL. Figure 3 (b) shows the fluctuating part of the pressure signal after subtraction of the smoothed pressure signal from the original one. The same smoothing process was applied on the head (H), discharge (Q), and generator torque (T_{GEN}), the results are presented in the next section.

3. Results and Discussion

3.1. Repeatability of the measurements

To ensure the repeatability, the transient measurements were performed twenty times. Synchronized pressure and velocity measurements were performed for all the transient repetitions. In this section, a statistical analysis for discharge (Q), head (H), generator torque (T_{GEN}), and guide vane angle (α) are performed and discussed for all the repetitions during load rejections to estimate the uncertainties involved. All the data were normalized between the minimum value 0 (0%), and the maximum value 1 (or 100%) taking the uniform length of the signal using Eq.2.

$$X[-] = \frac{X - X_{Min}}{X_{\max} - X_{Min}} \tag{2}$$

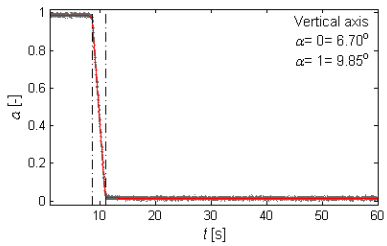

4 (a). Guide vane angle (α)

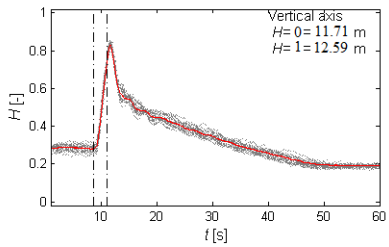

4 (b). Head (H)

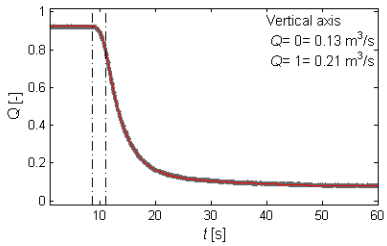

4 (c). Discharge (Q)

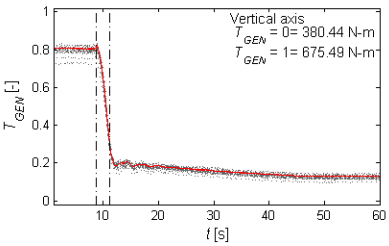

4 (d). Generator Torque (T_{GEN})

Figure 4. Repetitions for load rejection (BEP to PL), **4 (a)** Guide vane angle (α), **4 (b).** Head (H), **4 (c).** Discharge (Q), and, **4 (d).** Generator Torque (T_{GEN}), grey dot lines: repetitions for load rejection; red line: mean of all the repetitions; black dashed lines: start and end of the transient process.

Figure 4 shows the percentage variation in guide vane angle (α), head (H), discharge (Q), and generator torque (T_{GEN}) for all the repetitions of the load rejection (BEP to PL) operation. The vertical axis (y-axis) represents the variation in the corresponding property. The corresponding steady state values before and after the transient are presented in Fig. 4(a-d). The estimated maximum uncertainties were ±0.08°, ±0.09 m, ±0.003 m^3/s, and ± 4.40 N-m for the guide vanes angle (α), head (H), discharge (Q), and generator torque (T_{GEN}), respectively. The repeatability for the transient operation was found to lie in a certain and acceptable band. Therefore, a single measurement can be trusted and selected for the further investigations. Up to 8.45 s, the turbine was operated at the BEP (9.8°). At 8.45 s, the movement of guide vanes is started and hit at PL (6.7°) operating condition at t=10.90 s (Fig 4). The

torque variation is almost following the guide vanes movement. The flow rate is changing decreasing gradually and become stabilize at around *t*=48 s. The head is determined by measuring the differential pressure across the turbine and is the most affected parameter due to the development of high-peak pressure pulsations during guide vanes closure.

3.2. Instantaneous high frequency variation in the vaneless space and draft tube

The fluctuating signals from the transient pressure and velocity data were used for spectral analysis. Spectrograms are used to present the transient spectral analysis. The function uses the Goertzel algorithm to analyze the data. The window size of 4.09 s with 95% overlap was selected after a sensitivity analysis on the pressure. Similarly, the spectral analysis of the velocity data was presented after extracting the fluctuating velocity along two points on the PIV plane. The coordinates in millimeters for the two points are P1 (-87.50,-30, 0) and P2 (87.50, -30, 0) according to axis system shown in Fig. 2 (a). The window size of 2 s with 95% overlap was selected after a sensitivity analysis on the velocity. The frequencies in the figure were normalized using the runner rotational frequency (f_n=5.55 *Hz*).The color bar in the spectrogram shows the power spectral density (PSD) of the frequency analysis in logarithmic scale. The following equation was used for the PSD, presented in the spectrogram:

$$PSD_{log} = 10 \times \log(10 \times PSD) \quad (3)$$

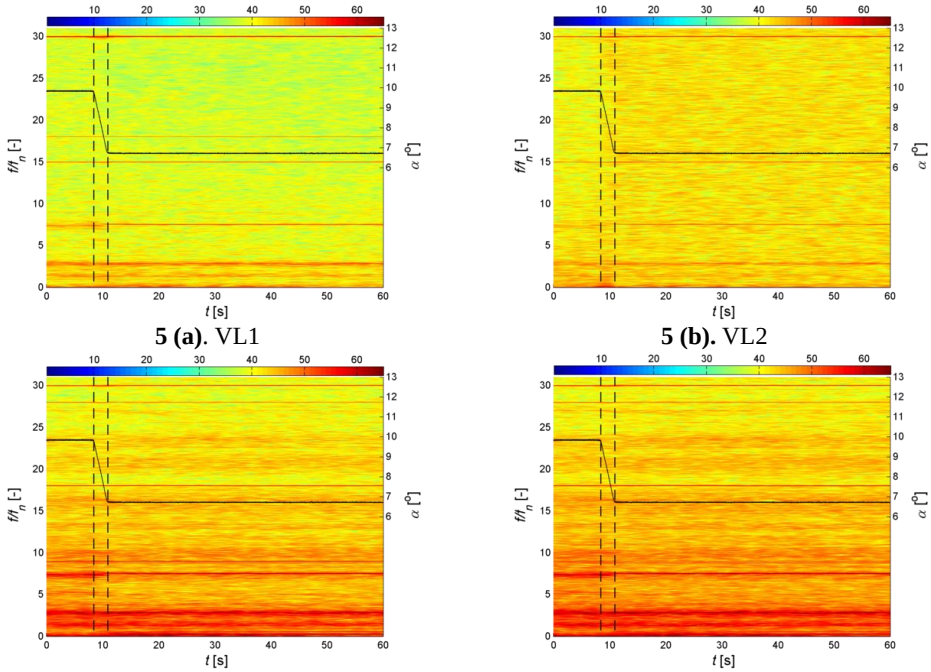

5 (a). VL1 **5 (b).** VL2

5 (c). DT5 **5 (d).** DT6

Figure 5. Spectrogram of the pressure sensor located in the vaneless space and draft tube during load rejection from BEP to PL, **5(a).** VL1, **5(b).** VL2, **5(c).** DT5, and **5(d).** DT6. Black solid line: guide vanes angle ($\alpha°$); dashed line: start and stop of the guide vanes movement.

The resulting spectrogram of the sensor located at VL1, VL2, DT5, and DT6 during load rejection from BEP to PL are presented in Fig. 5 with a focus on the high frequency region 2-30.f_n. The y axis on the right-side of the spectrogram represents the guide vanes angular movements ($\alpha°$). For all the sensors,

the blade passing frequency (30.f_n) is present in the pressure signal as expected. The harmonics of the runner frequency (15.f_n) are also present in the vaneless space sensors. Seen in the spectrogram, during transient operation, there is a significant level of fluctuation in the blade passing frequency and its amplitudes. There is a simultaneous change in normalized blade passing frequency from 29.96.f_n to 30.02.f_n. Similar behavior for the blade passing frequency are noticed at all the pressure sensors (VL2, DT5, and DT6) during the transition from BEP to PL but the maximum influence is at the sensor (VL1) near to the spiral casing inlet. The amplitudes of guide vane pass frequency (28.f_n) are also noticed in the draft tube sensors because the frequency is not completely dampened while traveling downstream to the runner.

In the pressure signals, other dominating frequencies are 18.f_n, 7.5.f_n, and 2.9.f_n. The normalized frequency of 18.f_n (100 Hz) was observed in the vaneless space sensor (VL1). This frequency might be attributed to the one–third harmonics of the three phase rectifier and second harmonics of the grid frequency. It is assumed that this frequency will not be available in the system with generator off. The normalized frequency of 7.5.f_n (41.62 Hz) and 2.9.f_n (15.96 Hz) are observed in all pressure sensors. These frequencies might be the standing wave of the system due to the length from the exit of the runner to downstream tank water level (5.6 m) and inlet pipe length to the turbine (14.6 m). Because the sound speed was not experimentally determined, it is assumed to vary between the speed of sound in still water (~1450 m/s) and speed of sound in air (~340 m/s). The amount of air entrapment may vary the speed of sound in the system [14-15]. In the present work, measurements were performed in open loop, increasing the occurrence of entrapped air. Assuming a sound wave velocity of 932 m/s, frequencies are calculated for the upstream and downstream lengths using Eq. 4.

$$f_{sv} = \frac{a}{4L} \tag{4}$$

Where a= sound wave velocity in the system, L = downstream and upstream length

3.3. *Instantaneous low frequency level variation in the draft tube for pressure and velocity signal*
Figures 6-7 show the spectrograms for the low frequencies available in the draft tube for the pressure and velocity data, respectively. The axial (v) and radial (u) velocities data are extracted from the two points P1 and P2 on the PIV plane. The instantaneous recorded pressure and velocity data present the appearance of a low frequency of 0.29.f_n (1.63 Hz) after the transition. This is attributed to the presence of the rotating vortex rope (RVR) in the pressure and velocity data. The harmonics of the RVR frequency are also present in the spectrograms.

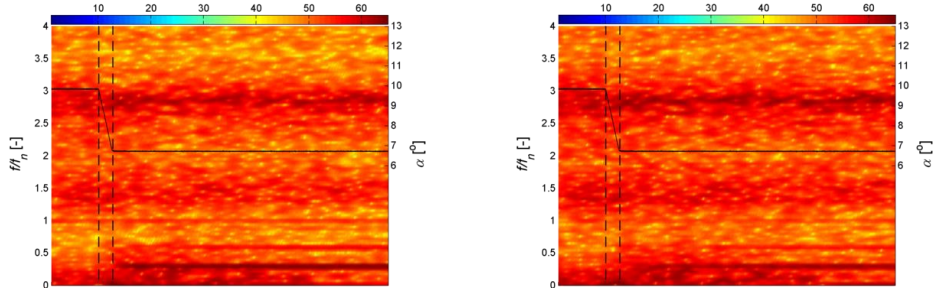

6 (a). DT5 **6 (b).** DT6

Figure 6. Spectrogram of the pressure sensor located in vaneless space and draft tube during load rejection, **6(a).** DT5, **6(b).** DT6, Black solid line: guide vanes angle (α°); dashed line: start and stop of the guide vanes movement

From the spectrograms of the axial and radial velocities for two points P1 and P2 (Fig.7), the time of appearance of the RVR is different for the axial and radial velocities. The velocity spectrograms show

the significant background noise levels (vertical broadband) at some random time intervals with the phenomenal frequencies available in the system. This may be attributed to the low sampling rate (40Hz) of measurement. Usually, noise level is higher from the PIV measurements if the sampling rate is lower than the maximum frequency available in the system [16]. A detailed investigation has been carried out by assuming that there is the existence of a plunging mode of the RVR. These signals are decomposed using the procedure given by Bosioc et al. (2012) [17]. The synchronous (RVR plunging) and asynchronous (RVR rotating) components are determined as below;

$$\frac{(A_1 + A_2)}{2} = \text{Synchronous component}, \quad \frac{(A_1 - A_2)}{2} = \text{Asynchronous component}$$

Where A1 and A2 are the pressure and velocity signals at points P1 and P2, respectively.

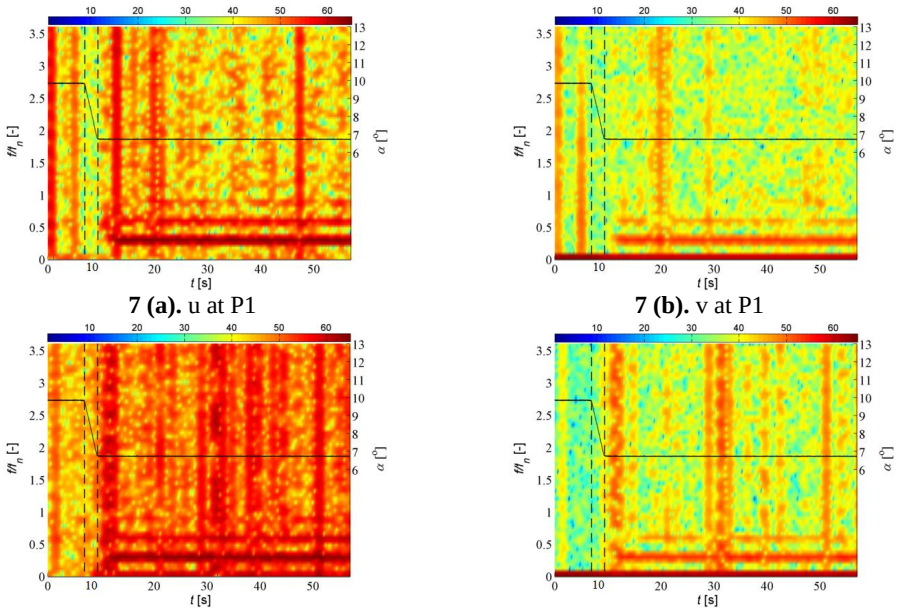

7 (a). u at P1 **7 (b).** v at P1

7 (c). u at P2 **7 (d).** v at P2

Figure 7. Spectrograms of the radial and axial velocities for two points (P1 and P2) data extracted from the PIV vector field, Black solid line: guide vanes angle (α°); dashed line: start and stop of the guide vanes movement

The dimensional amplitudes variation of the RVR for the plunging and rotating modes during load rejection (BEP to PL) are presented in Fig.8. The RVR plunging mode appears 0.8 s before the rotating mode**.** The amplitude of the RVR rotating mode is larger than the plunging mode as shown in Fig. 8 (a) for the draft tube pressure sensors. The amplitudes of the RVR in the plunging mode appear to be stronger at the end of the transient. The same procedure to resolve the RVR rotating and plunging mode is applied to the radial (u) and axial (v) velocities separately for the two points (P1 and P2) which are extracted from the PIV vector field. Fig. 8 (b) and Fig. 8(c) present the time of appearance of the RVR rotating mode and plunging mode in the draft tube for the radial and axial velocities, respectively. In Fig. 8(b) and Fig. 8(c), the amplitude of the plunging mode does not appear in the radial velocity and the amplitude of rotating mode does not appear in the axial velocity for the two radially apart points P1 and P2. Therefore, the radial velocity is only involved in the RVR rotating mode and the axial velocity in the RVR plunging mode.

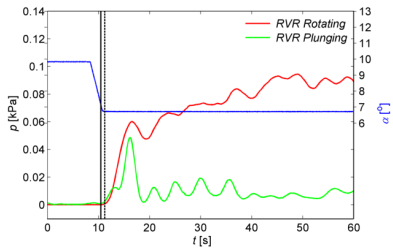

8(a). RVR rotating and plunging mode for draft tube pressure sensors (DT5 and DT6)

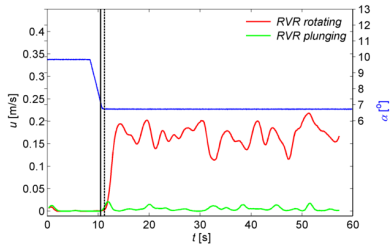

8(b). RVR rotating and plunging mode of the radial velocity assuming point P1 and P2

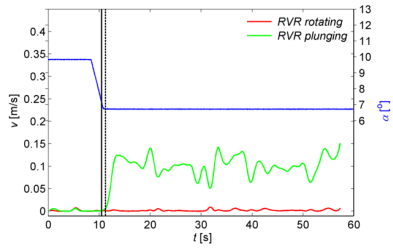

8(c). RVR rotating and plunging mode of the axial velocity assuming point P1 and P2

Figure 8. Time of appearance of RVR rotating and plunging mode in the pressure and velocity data, **8(a).** At DT5 and DT6, **8 (b).** At P1 and P2 for radial velocity, and **8(c).** At P1 and P2 for axial velocity, black solid line: appearance of the plunging mode; black dashed line: appearance of the RVR

Conclusions

Unsteady synchronized pressure and velocity measurements were performed in the high head model Francis turbine during load rejection from BEP to PL. The aim of the study was to investigate the dominating frequencies available and developed in the system before, in between, and after the transition. The results showed the blade passing frequency is available in the complete flow domain of the system as presented by the spectrograms of the vaneless space and draft tube sensors. The significant level of variation in blade passing frequency level was noticed during the transition phase because flow becomes unstable in the runner blade passage due to mismatch of flow angle between the guide vanes outlets and runner inlet. The standing waves frequencies for downstream and upstream length to the runner are presented and discussed with the assumption of sound-wave velocity available in the laboratory. The frequencies are available in a synchronous mode that indicates these frequencies are independent of the runner frequency. The variation in downstream standing wave frequency after transient have noticed due to change in the downstream tank level with discharge to the turbine. The closing of guide vanes during load rejection (BEP to PL) are causing the swirl in the draft tube and formation of RVR. The RVR frequency was further decomposed into two modes, RVR rotating and RVR plunging. It was observed that the RVR plunging appears 0.8 s before the rotating mode. However, the rotating mode was observed with higher amplitudes in comparison to plunging modes. The RVR rotating and plunging modes were further decomposed with the velocity data and it was observed that the axial velocity only contributes to the development of the plunging mode and radial velocity contributes to rotating mode. The transition (BEP to PL) was performed for the time 8.4 s to 10.9 s. The plunging mode appears in the system in between transition phase at 10.5 s, and rotating mode appears after 0.8 s of plunging mode. The time of appearance of RVR rotating and plunging was found same from the pressure and velocity data.

Acknowledgement

Rahul Goyal and Prof. Michel Cervantes are grateful to the Swedish water power center (SVC) for the financial support. The authors would like to thank the Norwegian Hydropower Centre (NVKS) for the financial support. The measurements have been carried out in collaboration between LTU, Sweden (NTNU, Norway) and IIT Roorkee. The author's gratitude also goes to the staff of water power laboratory, NTNU, Norway.

References

[1] Trivedi C, Gandhi B K, and Cervantes M J 2013 *J. of Hydraulic Research* **51 (2)** 121

[2] Trivedi C, Gandhi B K, Cervantes M J and Dahlhaug O G 2014 *J. of Hydraulic Research* **52 (2)** 283

[3] Amiri K, Mulu B, Raisee M and Cervantes M J 2015 *J. of Hydraulic Research* **54 (1)** 56

[4] Keck K and Sick M 2008 *ActaMech* **201** 211

[5] Cervantes M J, Andersson U and Lövgren H M 2010 *IOP Conf. Series: Earth and Environmental Science*, **12(1)**, 012014

[6] Vekve T and Skåre P E 2002 Velocity and pressure measurements in the draft tube on a model Francis turbine *Proc. of the XXI Int. Conf. on Hydraulic Machinery and Systems (Lausanne)*

[7] Vekve T 2004 An experimental investigation of draft tube flow *Ph.D. thesis* (Norway: Norwegian University of Science and Technology)

[8] Korbo E, Dahlhaug O G and Nielsen T K 2008 On board pressure measurement in Francis model Runner *Proc. of the XXIV Int. Conf. on Hydraulic Machinery and Systems (Brazil)*

[9] Korbo E 2010 Measurement of pressure pulsation in Francis turbine *Ph.D. thesis* (Norway: Norwegian University of Science and Technology)

[10] Cervantes M J, Trivedi C, Dahlhaug O G and Nielsen T 2015 *J. of Phys.* **579** 011001

[11] IEC 60041 1991-11 Field acceptance tests to determine the hydraulic performance of hydraulic Turbines, storage pumps and pump-turbines *International Electrotechnical Commission* (*Geneva, Switzerland*)

[12] IEC 60041 1991-11 Hydraulic turbines, storage pumps and pump turbines- model acceptance test *International Electrotechnical Commission* (*Geneva, Switzerland*)

[13] ASME-PTC18 2011 Hydraulic turbines and pump-turbines performance test codes *ASME New York*

[14] Nielsen T 1990 Transient characteristics of high head Francis turbines *Ph.D. thesis* (Norway: Norwegian University of Science and Technology)

[15] Knudsen H 2008 Study of the speed of sound in pipes and pulse reflections for open and closed boundary conditions and non-return valve *Ph.D. thesis* (Norway: Norwegian University of Science and Technology)

[16] Koschatzky V, Boersma B J, Scarano F and Wasterweel J 2011 High speed PIV applied to aerodynamics noise investigation *VIII International symposium on particle image velocimetry-PIV09* (*Melbourne, Victoria, Australia*)

[17] Bosioc A L, Resiga R S, Muntean S and Tanasa C 2012 *J. of Fluids Eng.* **137** 081104-1

Paper 4

Hydrodynamic Damping of a Fluttering Hydrofoil in High-speed Flows
Bergan, C. W., Solemslie, B. W., Østby, P., Dahlhaug, O. G.
The International Journal of Fluid Machinery and Systems vol. 11, 2018

International Journal of Fluid Machinery and Systems
Vol. 11, No. 2, April-June 2018

DOI: http://dx.doi.org/10.5293/IJFMS.2018.11.2.146
ISSN (Online): 1882-9554

Original Paper

Hydrodynamic Damping of a Fluttering Hydrofoil in High-speed Flows

Carl W. Bergan[1], Bjørn W. Solemslie[1], Petter Østby[2,3] and Ole G. Dahlhaug[1]

[1]Waterpower Laboratory, Norwegian University of Science and Technology
Alfred Getz v. 4, 7034 Trondheim, Norway,
carl.w.bergan@ntnu.no, bjorn.w.solemslie@ntnu.no, ole.g.dahlhaug@ntnu.no
[2]Department of Mechanical and Industrial Engineering Norwegian University of Science and Technology
Richard Birkelands vei 2B, 7034 Trondheim, Norway
[3]Rainpower AS Instituttveien 8, 2027 Kjeller, Norway, petter.oestby@rainpower.no

Abstract

A hydrofoil resembling a high head Francis runner blade was submerged in a rectangular channel and attached to the walls in a fixed-beam configuration. The hydrofoil was excited by piezoelectric Macrofiber composite actuators (MFCs), and the vibration was measured at the trailing edge with Laser Doppler Vibrometry (LDV) and semiconductor strain gauges. The hydrofoil was exposed to water velocities ranging from 0 to 25 m/s. Lock-in occurred at approx. 11 m/s. The damping increased linearly with the water velocity, with a slope of 0.02 %/(m/s) below lock-in, and 0.13 %/(m/s) above lock-in. The natural frequency of the foil increased slightly with increasing water velocity below lock-in, due to the added stiffness of the passing water. Additionally, the natural frequency increased significantly when passing through lock-in, due to the vortex shedding phase shift.

Keywords: FSI, Damping, Francis, FRF

1. Introduction

In the current energy market, there is a push towards higher power concentration in turbines, causing them to be more susceptible to problems caused by Fluid Structure Interactions (FSI), such as fatigue cracking, vibration and resonance [1, 2]. Pressure pulsations and vibrations can cause devastating structural damage, due to the high number of cycles a turbine blade can experience within a day [3]. The key to prevent this, is to be able to predict a runner's dynamic properties in the design phase.

The dynamic response of a Francis runner is, in addition to the hydraulic excitation, dependent on two components: the natural frequency of the runner, and the fluid damping [4]. The present work takes an experimental approach to determine the damping factor in an open reference case, to be used as validation for simulation.

The vibrational magnitudes close to resonance of any vibrating system is strongly dependent of the damp- ening factor of the system [5]. In the design of a Francis runner, it is important to predict which frequencies will cause the runner blades to resonate. It is also important to be able to predict the magnitude of vibration in these frequency domains, in order to understand how the turbine will perform if exposed to those conditions. Most of the work that has been performed on vibrating hydrofoils in flowing water has dealt with relatively low velocity ranges. The highest velocities seen in earlier measurements were 25 m/s[3], and most of the previous work is below 15 m/s. For a high head Francis runner, typical velocities are in the range of 35 to 45 m/s, so high-velocity damping measurements are of particular interest.

The damping appears to be linear with respect to velocity, from both experimental and theoretical work [3, 4, 6, 7], but the experimental uncertainty grows in the high velocity range [3]. The literature is inconclusive with respect to the effect on natural frequency. Coutu found that the natural frequency remained unchanged with respect to water velocity well above lock-in, but the large uncertainty band leaves some ambiguity in the conclusion[3]. Yao found that the natural frequency increased through the lock-in region [6]. However, the experiments performed by Yao were on a hydrofoil constrained in a cantilever fashion, which are prone to vibrational modes not strictly relevant for a Francis runner. In fact, most of the work performed with submerged hydrofoils employs a cantilever hydrofoil[7, 8, 9].

Received June 23 2017; revised September 28 2017; accepted for publication December 23 2017: Review conducted by Yoshinobu Tsujimoto. (Paper number O17043J)
Corresponding author: Carl W. Bergan, carl.w.bergan@ntnu.no

2. Materials and Methods

The tests were performed in a straight Ø300 mm pipe section available at the Waterpower Laboratory at the Norwegian University of Science and Technology (NTNU). The length of the pipeline is approx. 28 m, and the test section was placed close to the middle of this stretch. The test section is shown in Fig. 1.

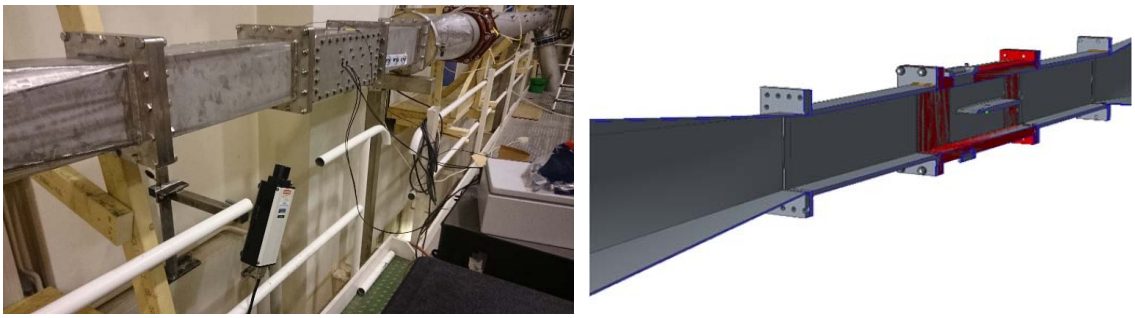

(a)Picture of test rig (b) Sliced CAD model of test rig

Fig. 1 Test section placed in the straight pipeline. The 300 mm circular cross section is changed to a 150x150 mm2 rectangular cross section.

The test section was designed to ensure a sufficient stiffness, in order to provide a grounded support for the test structure, i.e. the hydrofoil, as is good practice for modal testing [10]. This also enables the assumption of stiff walls for boundary conditions when performing structural simulations.

The hydrofoil geometry was long and slender, with a thickness of 12 mm and a cord length of 250 mm. After 150 mm, the thickness was tapered down to 4.5 mm at the trailing edge, before being chamfered and rounded on one side, as is normal for runner blades. The hydrofoil was milled from a single piece of aluminium alloy, and grooves were milled for instrumentation and cables. A cord wise cross section of the foil is shown in Fig. 2.

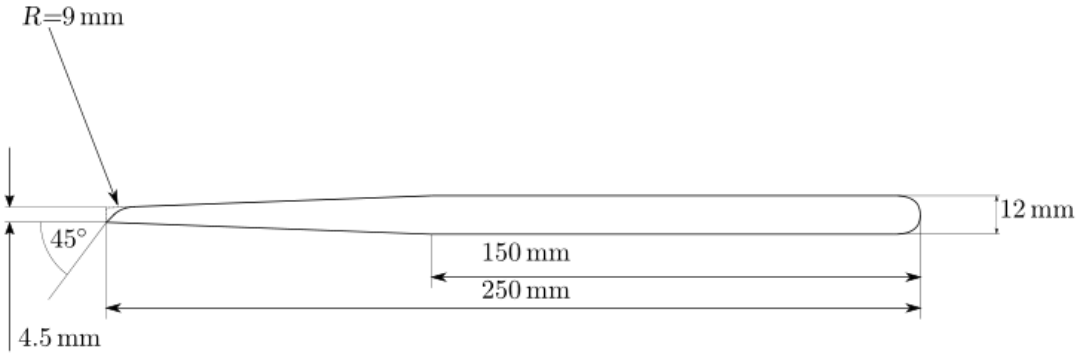

Fig. 2 2D view of the hydrofoil with dimensions

The hydrofoil was mounted without any angle of attack, and was then excited using piezoelectric Macrofiber composite (MFCs) actuators from PI Ceramic. Two MFCs were mounted on each side of the foil at the width wise center, close to the trailing edge. By exciting these in a sinusoidal pattern phase-separated by 180◦, a bending action is induced in the blade. A schematic of this type of excitation can be seen in Fig. 3.

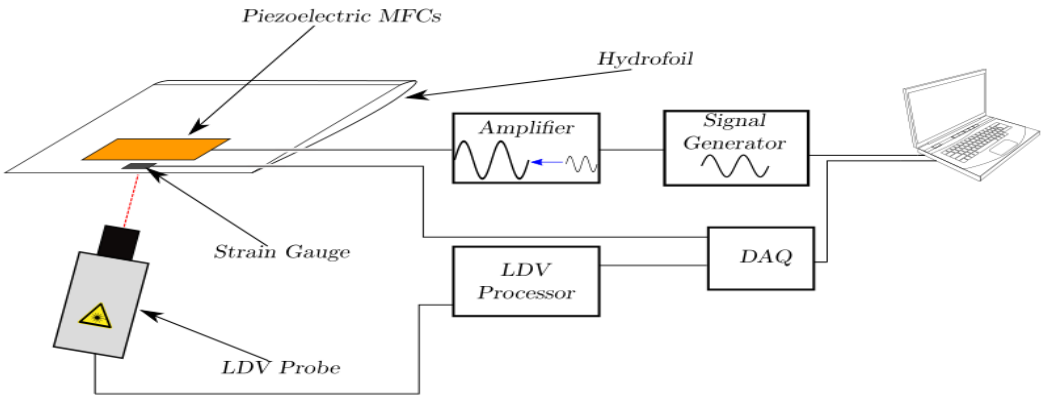

Fig. 3 Schematic of the experimental setup

In order to measure the vibrational amplitude, semiconductor strain gauges from Kulite were mounted on the trailing edge of the hydrofoil, directly downstream the MFCs.

In addition to strain gauges, the vibrational amplitude was measured using Laser Doppler Vibrometry (LDV) equipment from Polytech. LDV is a non-intrusive measurement method that measures vibration using the Doppler-shifted reflection of laser light. The LDV measures vibration in a single spot, along the axis of the laser beam, and the measurement point was located at the trailing edge of the foil.

The tests were performed using a Stepped-Sine excitation, in which a series of constant-frequency excitations are performed in order to avoid transient effects when moving through a resonant region [10].

Each measurement consisted of approx. 60 excited frequencies, and each measurement was repeated 30 times in order to obtain sufficient statistics for an assessment the uncertainty in both damping and natural frequency. The tests were performed with water speeds ranging from 0 to 25 m/s, with steps of 5 m/s. The test rig was pressurized in order to obtain cavitation-free conditions.

3. Results and Discussion

The experiments were successfully conducted with water velocities up to 25 m/s, without cavitation. Frequency analysis using the Welch method, as implemented by MATLAB, was conducted on the excitation signal and on the response of the hydrofoil, in order to generate a frequency response curve around the measured mode. The Welch method is an estimate of the power spectrum, which reduces the power noise by reducing the frequency resolution through averaging. For this experiment, such a trade-off was deemed appropriate, as the damping estimate is sensitive to the estimated amplitudes.

The damping was estimated using the Circle-Fit Method, also known as the Kennedy-Pancu Method. The method yields the damping ratio through a geometric investigation in the complex plane. By plotting the real and imaginary parts of the frequency response data in the complex plane, a resonant peak will appear as a circle, as shown in Fig. 4. It can then be shown that the damping ratio can be calculated through the following geometric relations:

$$\zeta = \frac{\omega_b - \omega_a}{\omega_a \tan(\theta_a/2) + \omega_b \tan(\theta_b/2)} \tag{1}$$

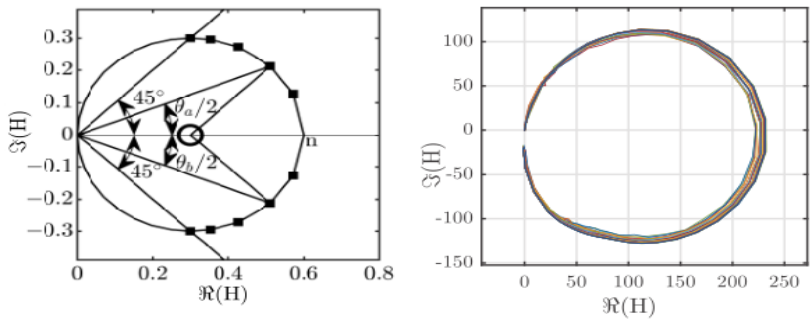

(a)Circle fit (b) Nyquist plot

Fig. 4 Nyquist plot of ideal and real data. In this plot, H is the complex frequency response of the vibrating system

In eq. (1), ωa and ωb denote the frequency at points a and b respectively, and ζ is the damping. The Circle-Fit Method is described in more detail by Craig and Kurdila in Fundamentals of structural dynamics[5]. By repeating the above measurement several times, the uncertainty in the modal parameters can be esti-mated with the student-t distribution.

3.1 Damping and natural frequency

The resulting damping ratios and natural frequencies are shown in Fig. 5.

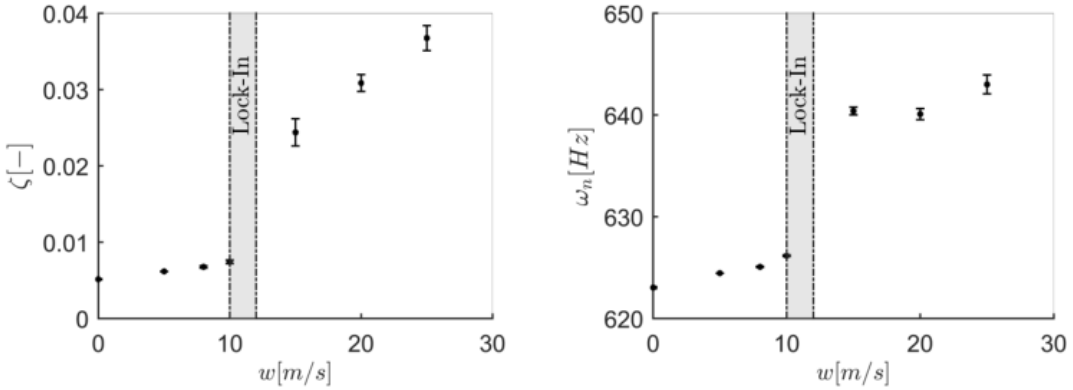

(a)Damping ratio (b) Natural frequency

Fig. 5 Damping and natural frequency

As indicated by Fig. 5(a), there is a clear correlation between the water velocity, and the damping factor of the vibrating system. Furthermore, this correlation seems to undergo some change around 10 to 12 m/s. In fact, this is the velocity where the frequency of the vortex shedding resonates with the natural frequency of the hydrofoil, commonly referred to as ”lock-in”. This change around lock-in was previously observed, for the torsional vibration mode of a cantilever beam [6]. It should be noted that the torsional mode of the cantilever beam is similar to the second bending mode of a fixed beam, and it is expected that the dynamic behavior of the two modes are similar. Although the present work has not investigated the second bending mode, it is thought to behave similarly to the first bending mode. In the vicinity of lock-in, the natural frequency of the foil undergoes an abrupt change, from 625 Hz to 640 Hz. There is no apparent trend above lock-in, and it may.

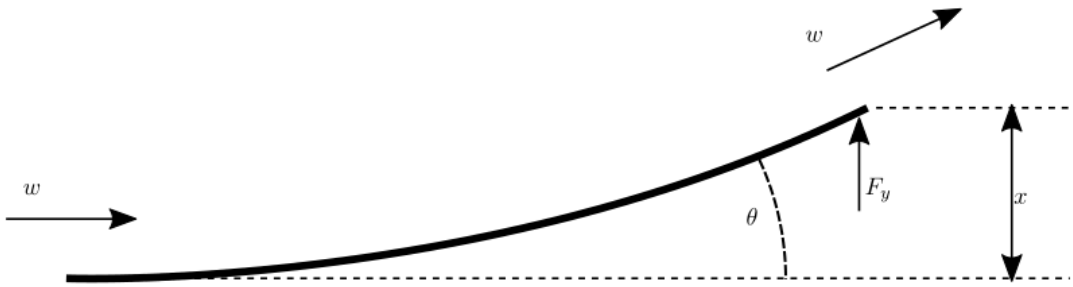

Fig. 6 Force balance on a bent beam.

The water approaching from the left is being deflected by the beam, shown as a thick black line. This in turn exerts a force on the beam, which is proportional to the deflection and to the water velocity squared very well be that the natural frequency is constant in that region. This corresponds with previous findings [3], where the natural frequency was found to be independent of the water velocity.

For velocities well below lock-in, there is a clear linear increase in the natural frequency of the foil. This increasing trend in dampened natural frequency conforms with what may be modeled as a spring with increasing stiffness, due to the water being deflected over the hydrofoil. If we consider a bent plate deflecting water, as shown in Fig. 6, the force on the plate from the water being deflected would be proportional to the deflection according to eq. (2). This is indeed the case in the present measurements, since the deflection was measured at the trailing edge, and the water will therefore also be deflected.

$$F_y \propto w^2 \cdot \sin(\theta) \tag{2}$$

In eq. (2), the proportionality between the force and the velocity will account for a stiffening spring as the water velocity is increased, indicating a higher natural frequency.

Fy $\propto$ sin (θ) will be equivalent to Fy $\propto$ θ for small values of θ, meaning for small deflections at the trailing edge. By considering the geometric deformation of the trailing edge, it is evident that the angle at the trailing edge is proportional to the deflection through the relation shown in eq. (3).

$$\theta \propto \arctan(x) \tag{3}$$

Equation 3 will be equivalent to θ $\propto$ x for small deflections. Hence the force exerted on the blade by the deflected water should be proportional to the deflection and the water velocity squared.

The stiffness of the spring will increase as the water velocity increases, effectively increasing the spring constant acting on the vibrating system. It can be argued that such an increase in stiffness will account for the observed increase in natural frequency. The scale of this effect is, however, rather small, and is quickly dominated by other effects as the damping increases. This could indicate that the effect is only significant below lock-in, as indicated by Fig. 5(b). A more thorough theoretical investigation of the forces working on the hydrofoil above lock-in can be found in [4], where the added stiffness is assumed to be negligible.

3.2 Vortex shedding resonance

During the experiments, the vortex shedding reached resonance with the hydrofoil. The resonance occurred at approx. 11 m/s, which correspond well with the theoretical Von Karman frequency, as described in subsection 3.3. This resonance is particularly problematic, as it is on the same order of magnitude as the excitation amplitude. As such, there is no reliable data available in the range 10 to 12 m/s. In order to quantify the effect from lock-in, a vibration study was carried out without excitation from the MFC patches. Fig. 7 shows the level of vibration across the frequency spectrum both with and without excitation.

As shown in Fig. 7, there is significant excitation from the vortex shedding in the vicinity of the lock-in velocity, but the shedding excitation becomes negligible outside of the range 9 to 12 m/s. Determining the damping ratio in the lock-in region is difficult, due to the added force of the vortex shedding. However, the foil behavior close to lock-in is quite interesting both above and below lock-in.

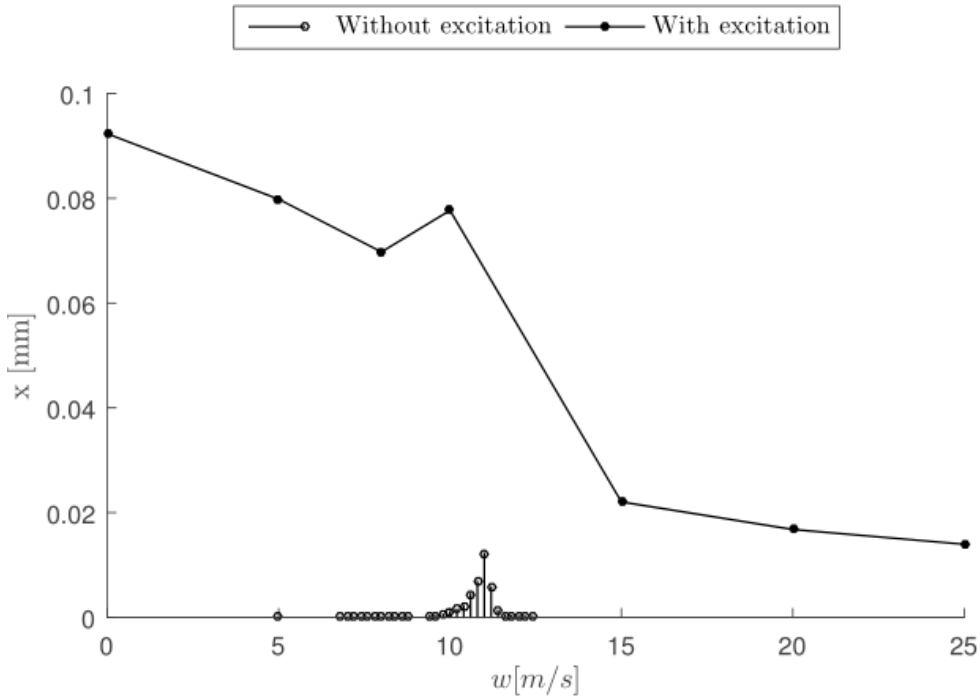

Fig. 7 Measured vibrational amplitudes with and without MFC excitation.

Looking back at Fig. 5(a), the behavior is quite different when comparing results for velocities below and above lock-in. There is a large jump in the natural frequency, and the change in damping ratio takes on a steeper slope.

3.3 Von Karman Damping

Williamson [11] showed that the phase angle between the vortex shedding and the movement of the structure changes through the locking region much like the phase change of a 1 Degree of Freedom (DOF) mass spring system changes through resonance. Using this, one can model the foil and vortex street as a 2 DOF system where eq. (4) is the foil/water system while eq. (5) expresses the vortex shedding:

$$\ddot{x} + 2\zeta\omega_n\dot{x} + \omega_n^2 x = a \cdot C_l \tag{4}$$

$$\ddot{C}_l + 2\zeta_c\omega_c\dot{C}_l + \omega_c^2 C_l = b \cdot \dot{x} \tag{5}$$

In the equations above, Cl is the lift, a and b are constants, x is the foil deflection, ωn is the natural frequency of the foil, ωc is the frequency of the vortex shedding, ζ is the damping of the foil and ζc is the damping of the vortex shedding.

These equations are a simplified version of the van der Pol type oscillator proposed by Bishop and Hassan [12]. Their model contains some non-linear terms which model the hysteresis near lock-in and self exciting phenomena. These are removed in eq. (5) as there are not any reliable measurements in the lock-in region. The eigen frequency of the foil, ωn , is known from the measurements at no velocity, w . The damping of the foil water system ζ without regards for the vortex interaction increase linearly with flow [4] and is thus modelled as $\zeta = \zeta n0 + w \cdot \zeta n1$. Further is the eigen frequency of the vortex shedding modelled after Brekke's [13] formula :

$$\omega_c = 190 \cdot \frac{133}{100} \cdot \frac{w}{(4.5 + 0.56)} \tag{6}$$

The damping of the shedding ζc is assumed to be a constant. Together this leaves four unknown variables: ζc, a , b , and ζn1 which can be found by fitting the solved equations to the measurements using a least squares method.

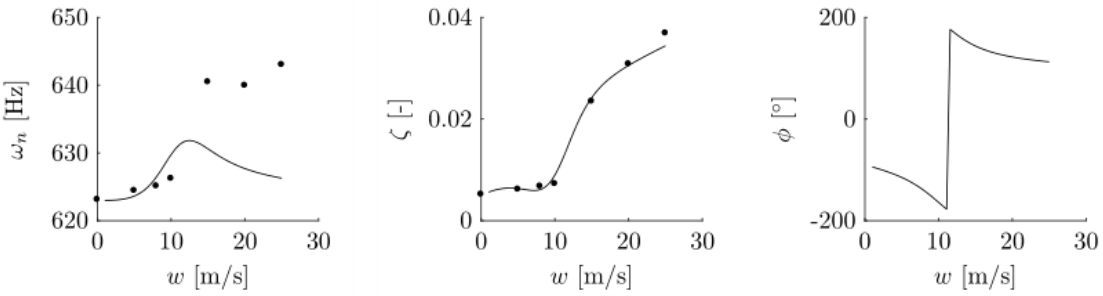

(a) Damping (b) Eigen frequency (c) Phase

Fig. 8 Eigen frequency, Damping and Phase between vortex shedding and foil movement. The dots indicate experimental data, while the line shows the model

Figure 8 shows that the simple model is able to capture the change in damping before and after the lock-in. It does however not capture the entire change in the natural frequency.

3.4 Nonlinear Effects

At this stage, it is appropriate to discuss is whether or not the assumption of linearity that is so often applied in this type of analysis actually holds. A linear system is, by definition, a system which has the following properties: [10]

1. Doubling the magnitude of the excitation force results in a doubling of the response
2. Two or more excitation patterns applied simultaneously results in the sum of the responses, had those forces been applied individually

In order to assess this, future experiments are required. Reese [14] found the experimental setup using a cantilever beam to behave linearly, but only for vibrations in air. There was no test of linearity when the hydrofoil was submerged in water, and exposed to flow.

During our experiment, the frequency response of the foil was found to be somewhat dependent on the excitation amplitude. This is an indicator that the system may not be linear. Two measurements of the frequency response, performed with different excitation amplitudes are shown in Fig. 9.

As Fig. 9 indicates, the FRF is sensitive to variations in excitation amplitude, which could indicate that the system is weakly non-linear. From the FRF, it appears that the damping increases with the excitation amplitude, causing the FRF to peak at a lower amplitude, with a lower natural frequency.

Non-linearities can be unveiled by examination of the inverse frequency response function [10]. For a linear system, the real component of the inverse frequency response function should be linearly proportional to the frequency squared, while the imaginary component of the inverse FRF should be linearly proportional to the frequency. A deviation in this linear relationship to is a strong indicator of a nonlinear system. Such a comparison is shown in Fig. 10.

As shown in Fig. 10, there is some indication that the system may not be strictly linear. It does appear that the non-linearity is more significant at low velocities, where the damping is small, and the vibrational amplitude is large. It is not known how significant the non-linearities are for the measurements, but it is recommended that future measurements investigate whether or not the non-linearities are negligible. In order to investigate this, a constant-response modal analysis is suggested by Ewins, since practically all non-linear behaviour is proportional to response amplitude, and keeping the response amplitude constant should therefore minimize the impact of non-linear behaviour [10].

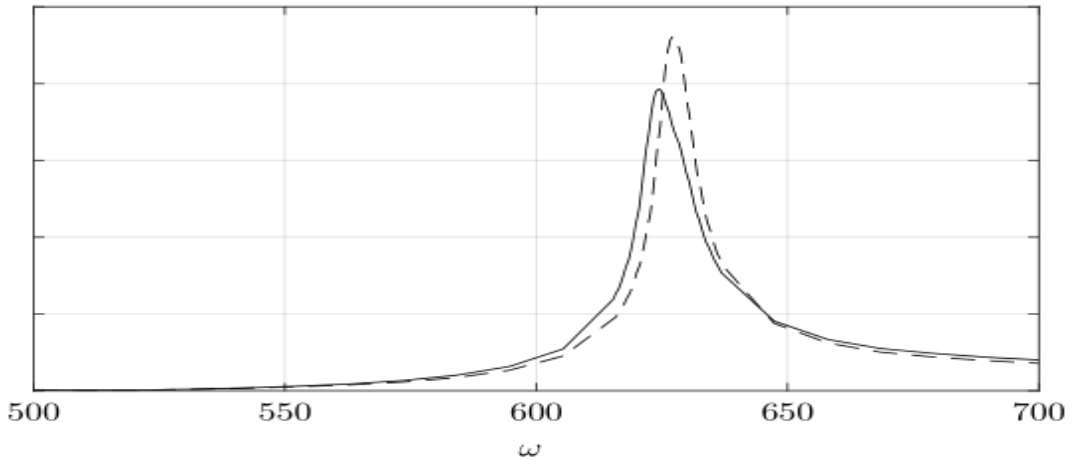

Fig. 9 Frequency response at w = 5 m/s for two different amplitudes of excitation. The dashed line indicates a measurement with a lower excitational amplitude. ω denotes the frequency.

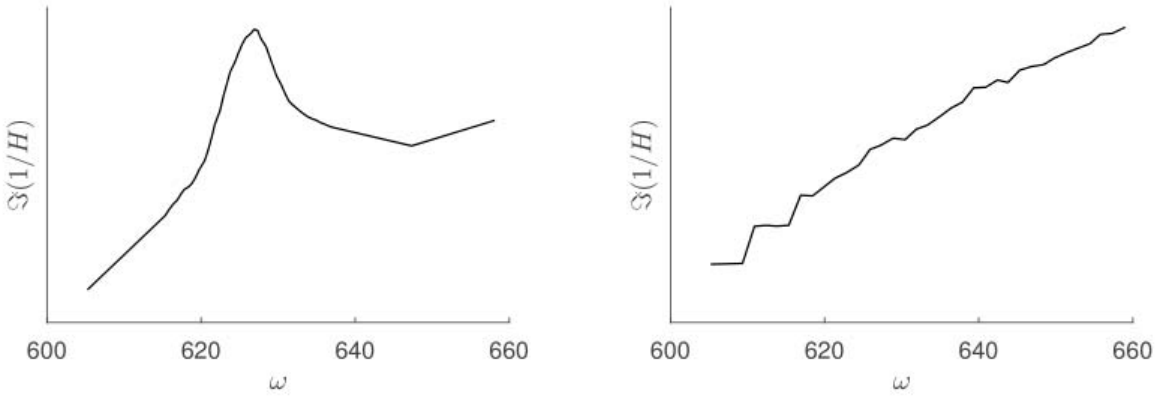

(a) Non-linearity at w =5 m/s

(b) Non-linearity at w =20 m/s

Fig. 10 Imaginary component of the inverse frequency response for the measurement, denoted by 8'(1/H), H being the complex frequency response. Note how the apparent nonlinearity appears to smoothen out as the velocity, and damping, increases.

4. Conclusions

This experiment has shown that there is a linear relationship between the damping ratio and water velocity, thereby confirming previous observations [4, 3, 6]. The natural frequency has been shown to increase linearly for velocities below lock-in, due to the added stiffness of the deflected water. It has also been shown that the dependency on water velocity for both the damping factor and the natural frequency differs for water velocities below and above lock-in, due to the phase shift in vortex shedding when passing through the lock-in region. The damping has been accurately measured through a large number of repetitions for velocities both above and below lock-in. The observed jump in damping and natural frequency when moving through lock in leaves some questions unanswered, such as how the velocity field at the trailing edge changes when moving through lock-in, and how the phase of the pressure on the foil changes with respect to the foil movement. These questions will be further investigated. In addition, there is still some uncertainty in how significant the inherent non-linearity of the experimental setup are, and this will need to be assessed when doing similar experiments in the future.

Nomenclature

a	Mathematical constant	ωn	Natural Frequency of hydrofoil]
b	Mathematical Constant	ζn0	Damping at zero velocity
ζ	Damping	φ	phase shift
Fy	Deflecting force of a bent beam	ζn1	Slope of damping increase
x	Trailing edge deflection	ζc	vortex shedding damping
ω	Frequency	ωc	vortex shedding frequency
ωa	Frequency at point a	H	Transfer Function
ωb	Frequency at point b	w	Water velocity
Cl	hydrofoil lift		

References

[1] M. Gagnon and D. Thibault. “Turbine Dynamic Behaviour and Expected Fatigue Reliability,” In: 6th IAHR International Meeting of the Workgroup on Cavitation and Dynamic Problems in Hydraulic Ma- chinery and Systems. Sept. 11, 2015.

[2] M. Flores, G. Urquiza, and J. M. Rodr´ıguez. “A Fatigue Analysis of a Hydraulic Francis Turbine Runner,” In: World Journal of Mechanics 02 (01 2012), pp. 28–34.

[3] A. Coutu et al. “Damping Measurements in Flowing Water,” In: IOP Conference Series: Earth and Environmental Science. Vol. 15. IOP Publishing, 2012, p. 062060.

[4] C. Monette et al. “Hydro-Dynamic Damping Theory in Flowing Water,” In: IOP Conference Series: Earth and Environmental Science. Vol. 22. IOP Publishing, 2014, pp. 32044–32053.

[5] R. R. Craig, A. Kurdila, and R. R. Craig. Fundamentals of Structural Dynamics. 2nd ed. OCLC: ocm61247316. Hoboken, N.J: John Wiley, 2006. 728 pp.

[6] Z. Yao et al. “Effect of Trailing Edge Shape on Hydrodynamic Damping for a Hydrofoil,” In: Journal of Fluids and Structures 51 (Nov. 2014), pp. 189–198.

[7] S. Roth et al. “Hydrodynamic Damping Identification from an Impulse Response of a Vibrating Blade,” In: Proceedings of the 3rd IAHR International Meeting of the Workgroup on Cavitation and Dynamic Problems in Hydraulic Machinery and Systems. Vol. 1. Brno University of Technology, 2009, pp. 253–260.

[8] P. Ausoni et al. “Cavitation Effects on Fluid Structure Interaction in the Case of a 2d Hydrofoil,” In: ASME 2005 Fluids Engineering Division Summer Meeting. American Society of Mechanical Engineers, 2005, pp. 617–622.

[9] O. de la Torre et al. “The Effect of Cavitation on the Natural Frequencies of a Hydrofoil,” In: (Aug. 13, 2012).

[10] D. J. Ewins. Modal Testing: Theory, Practice and Application. 2. ed. Mechanical engineering research studies Engineering dynamics series 10. OCLC: 247979435. Baldock: Research Studies Press, 2000. 562 pp.

[11] C. H. K. Williamson and A. Roshko. “Vortex Formation in the Wake of an Oscillating Cylinder,” In:

[12] Journal of Fluids and Structures 2 (July 1988), pp. 355–381.

[13] R. E. D. Bishop and A. Y. Hassan. “The Lift and Drag Forces on a Circular Cylinder in a Flowing Fluid,” In: Proceedings of the Royal Society of London A: Mathematical, Physical and Engineering Sciences 277.1368 (1964), pp. 32–50.

[14] H. Brekke. “A Review on Oscillatory Problems in Francis Turbine,” In: New Trends in Technologies: Devices, Computer, Communication and Industrial Systems, Sciyo (2010), pp. 217–232.

[15] M. C. Reese. “Vibration and Damping of Hydrofoils in Uniform Flow,” The Pennsylvania State Univer- sity, 2010

Paper 5

An Experimental Investigation of the Hydroynamic Damping of Vibrating Hydrofoils

Bergan, C. W., Tengs, E. O., Solemslie, B. W., Dahlhaug, O. G.

presented at 29th IAHR Symposium on Hydraulic Machinery and Systems, Kyoto, Japan, September 15-20, 2018. Proceedings to be published 2019

An experimental investigation of the hydrodynamic damping of vibrating hydrofoils

C W Bergan[1], E O Tengs[1,2], B W Solemslie [1], and O G Dahlhaug[1]

[1] NTNU Vannkraftlaboratoriet, 7491 Trondheim

[2] EDR & Medeso AS, NO-1337 Sandvika

E-mail: carl.w.bergan@ntnu.no

Abstract. As Francis turbines are chasing a higher efficiency, while trying to accommodate a wider load region, turbine blade fatigue is becoming a more pronounced problem. Details of the Fluid-Structure Interaction (FSI) between the turbine blades and the passing water is necessary to accurately predict the dynamic behavior of a runner in the design phase. The dynamic behavior of the turbine blades is characterized by three properties: The added mass of the surrounding water, the increased stiffness due to passing water, and the hydrodynamic damping provided by the surrounding water. Of the aforementioned properties, the hydrodynamic damping is not yet fully understood. When the turbine blades are excited close to resonance, the damping of the vibrating system determines the vibrational amplitude, and is therefore important in order to estimate the lifetime of a runner. The hydrodynamic damping of passing water has been investigated in a simplified setup, where the turbine blades are represented by a 2D hydrofoil. Two separate hydrofoil geometries have been tested. The hydrofoils were mounted in a "fixed-beam" configuration, meaning that both the deflection and the angle at the fastening point is zero. This setup was chosen, since it is the way that turbine blades are fastened in a Francis runner, and should therefore give applicable results when performing modal testing. The hydrofoils were mounted without any angle of attack, and exposed to water velocities up to 28 m/s. Modal tests in the entire velocity regime indicates that the damping factor increases linearly with water velocity, but at different rates below an above lock-in. The damping factor is rapidly increasing when the velocity goes beyond that of lock-in. This behavior is observed for both hydrofoils, even if the magnitude of the vortex shedding is of different magnitude for the two. A slight increase in natural frequency was also observed with increasing velocity, due to a combination of a stiffening effect of the water passing over the deflected blade, and a reduced added mass effect, in that the amount of water that vibrates with the hydrofoil is diminished when the water velocity is sufficiently high, i.e. it is blown away. The measurements have been compared with CFD simulations, indicating that the observed trend does indeed continue up to at least 45 m/s, indicating that the results are applicable to the velocity regimes occurring in a prototype Francis runner

1. Introduction

In the current energy market, Francis turbines are expected to deliver power at high efficiency while accommodating a large range of operation [1, 2]. This has caused several high head Francis runners to fail due to blade cracking, caused by Rotor-Stator Interaction (RSI) [3]. Fatigue damage due to vibration is a complex phenomena, with several factors: The static (mean) stress, the amplitude of the vibration, and the frequency of vibration. Within this, the amplitude of vibration, and hence the amplitude of the stress, can determine whether a turbine will withstand

the load, or if it will fail during operation. It is therefore important to understand the underlying mechanics that determine the vibrational amplitudes in the RSI-caused vibrations.

A classic damped vibrating system with a single degree of freedom can be characterized by three key parameters: stiffness, mass and damping. If one considered the oscillating turbine blade as a classic damped vibrating system, these characteristics will be slightly modified, as the presence of flowing water adds to stiffness, mass and damping. These parameters have been extensively investigated, and the impact of water on the stiffness and mass is well understood [4, 5, 6, 7]. The effect on damping has received less attention in the past, but recent studies have been conducted, indicating that the damping is indeed affected by the moving water. The damping is a critical quantity to understand, as the vibration amplitude is sensitive to damping at resonance. Some investigations of this have been performed in recent years, but they are limited in the velocity range investigated. In addition, the behavior of fluid damping in the velocity range where the blade's natural frequency coincides with the shedding frequency, known as lock-in, has not been a point of focus.

This paper presents experimental results on two separate hydrofoils, and a comparison is made between the results and simulation efforts.

2. Materials and Methods

The experimental setup and data analysis methods are described in the following section. The numerical setup is briefly explained, for an in-depth description, see [8].

2.1. Experimental Setup

The experiments were conducted at the Waterpower Laboratory at the Norwegian University of Science and Technology (NTNU). The test set-up consisted of a 150 mm by 150 mm square channel, containing the hydrofoil in a fixed-beam configuration, i.e. fastened in both ends. An image of the test rig is shown in Figure 1

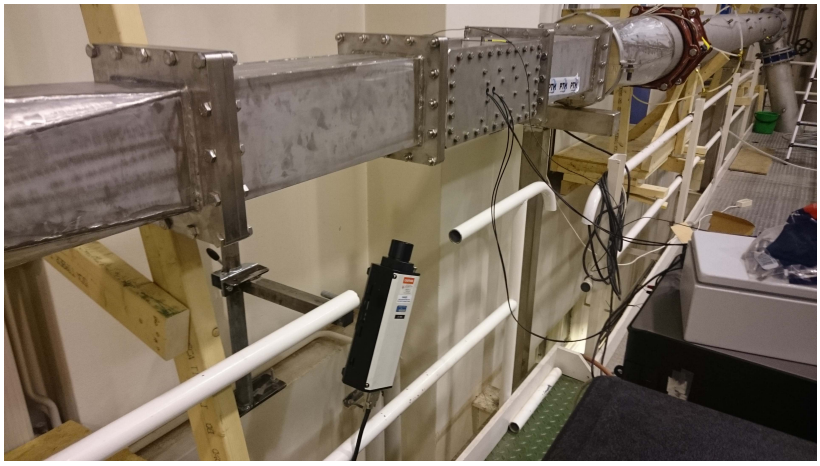

Figure 1. Image of the test rig.

The hydrofoils tested are illustrated in Figure 2. They are of the same width and cord length, but F0 has an asymmetric trailing edge, and a more blunt leading edge than F1 .

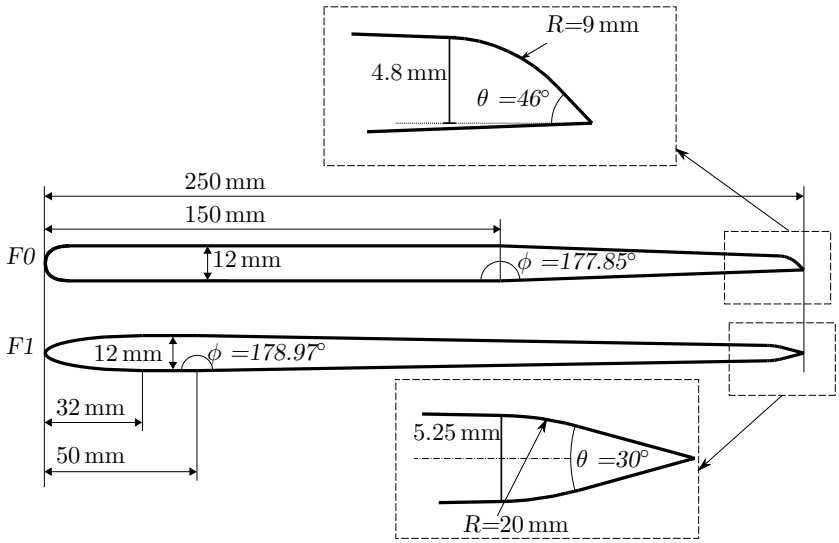

Figure 2. Hydrofoil geometries tested. Note that the tapering is much longer for F1 than for F0 , allowing for a much smoother tapering angle, ϕ . In addition, F0 as an asymmetric trailing edge, while F1 has a symmetric trailing edge. The leading edge of F0 closely resembles a semicircle with diameter equal to the foil thickness, whereas the leading edge of F1 is elliptic with major and minor diameter of 62 mm and 12 mm respectively.

The excitation was performed using Piezoelectric Macrofiber Composites (MFCs), which have the ability to provide excitation at specific frequencies, enabling measurements when the damping is quite large. This procedure is based on the approach previously employed by Coutu et al, Yao et al, and Roth et al [4, 9, 10, 5, 6], and the MFCs are similarly excited 180°out of phase, in order to obtain the maximum excitation force. For a more in-depth explanation on the application of MFCs in conjunction with modal testing of hydrofoils, the reader is referred to the work of Seely et al [10]. The response was measured with a combination of Laser Doppler Vibrometry (LDV) and semiconductor strain gauges from Kulite. A schematic of the test setup is shown in Figure 3. The tests were performed in cavitation-free conditions.

2.1.1. Testing procedure In order to avoid transient effects, a stepped-sine excitation pattern was chosen, as recommended by Ewins [11]. The testing therefore consisted of

(i) performing a continuous sweep, to identify the natural frequency

(ii) generating discrete sine waves around the resonant region

(iii) testing the response of each frequency

This process was repeated approx. 30 times for each velocity in order to estimate the uncertainty in both natural frequency and damping.

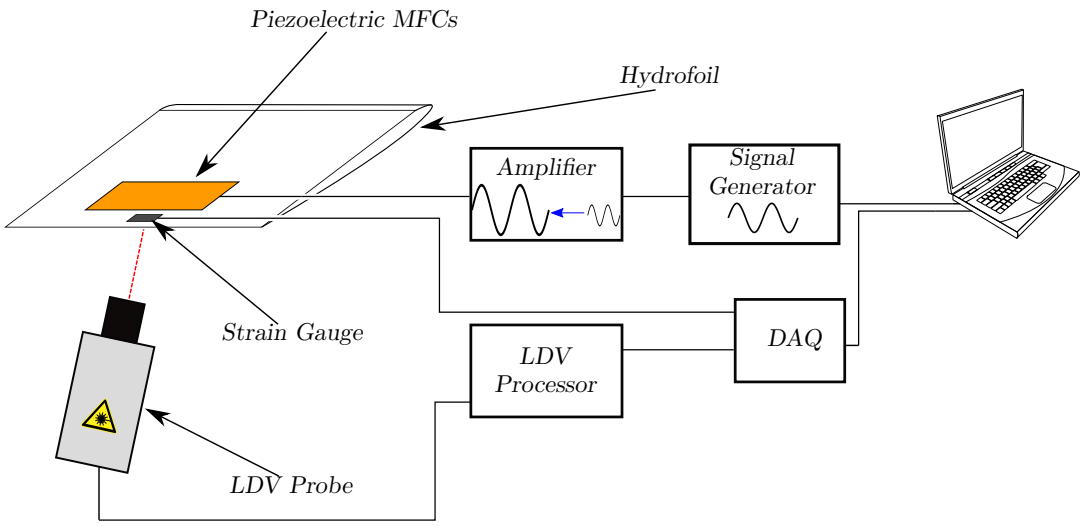

Figure 3. Schematic view of the measurement setup.

2.1.2. Analysis The amplitudes of both the excitation and response were calculated using the Welch method as implemented by MATLAB. The Welch method is an estimate of the power spectrum, which reduces the noise by reducing the frequency resolution through overlapping windows. For the amplitude estimates, the flattop window was chosen. Since the Welch method in MATLAB does not yield phase data, the phase difference between the excitation and response was estimated by calculating the cross-power spectral density. The magnitude ratio between the excitation and response, along with the phase difference was used to recreate the complex Frequency Response Function (FRF), which was used to calculate damping and natural frequency, using the nyquist diagram. By plotting the real part vs. the imaginary part of the FRF, a resonant region will appear as a circle. By curve fitting the data to a circle, geometric properties of the curve fit can be used to accurately estimate modal properties. This method was chosen, since it does not rely on data far away from the resonant region, and is therefore less sensitive to neighbouring modes of vibration. For a detailed explanation of the circle-fit method and the Nyquist diagram, the reader is referred to Ewins [11], and Bergan et al [12].

2.2. Numerical setup
The damping of F1 has been tested numerically using ANSYS CFX. To ensure fully developed flow conditions in the test section, the inlet of the test domain was extended in order to satisfy a common entrance length criterion of $L > 10 \cdot D_h$. Similarly, the test domain was extended downstream to avoid outlet conditions affecting the simulation results. The damping was found using a one-way coupling, but investigating the structural response in advance, and performing CFD on the blade with pre-determined vibration. For a more in-depth explanation of the numerical setup and results, the reader is referred to [8].

3. Results
In Figure 4, the damping factor ζ is shown with respect to the water velocity w . Figure 6 shows the evolution of the natural frequency ω_n of the hydrofoils with respect to w . The slope estimates for the evolution of the damping are summarized in Table 1

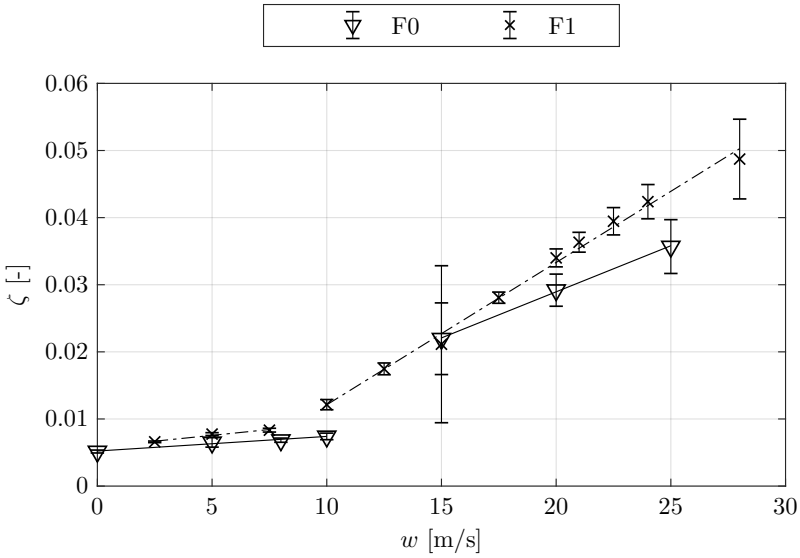

Figure 4. Damping vs velocity. Note that both hydrofoils exhibit a discontinuity in the slope around lock-in, at approx. 11 m/s for F0 , and at approx. 8 m/s for F1 .

Table 1. Slope of damping change vs. velocity

$\zeta/_w$	F0	F1
below lock-in	2.18×10^{-4}	3.48×10^{-4}
above lock-in	1.37×10^{-3}	2.12×10^{-3}

To give an idea of the numbers provided in table 1, the *Half-Amplitude* method is a useful tool [13]: A damping factor, ζ , of 0.01 (or 1%), means that oscillations will half in amplitude after 11 cycles, which for a hydrofoil with a natural frequency of 500 Hz is approx. 0.02 s.

The measurements are closely matched by the numeric simulations, shown in figure 5.

The experiments were limited to 28 m/s due to the onset of cavitation upstream the test section, even with a gauge pressure of 9 bar in the test section. Simulations were therefore conducted at 45 m/s, indicating that the trend obtained above lock-in continues.

As seen in Figure 4, the damping is nearly constant up to lock-in, but with a slightly positive slope. There is a distinct discontinuity, at approx. 11 m/s for F0 and at approx. 8 m/s for F1 . This is the lock-in region for each hydrofoil, the velocity at which the vortex shedding frequency coincides with the hydrofoil's natural frequency. This is detailed in table 2, where the maximum vibrational amplitudes are shown with and without MFC excitation. Vibration measured without MFC excitation is solely due to vortex shedding.

The natural frequency of the hydrofoils, as seen in Figure 6, seem to be relatively unaffected, but a closer investigation reveals a trend, see Figure 7.

Figure 7 shows that the natural frequency is not constant with velocity, it does in fact increase slightly with water velocity. F0 shows a sudden jump in natural frequency around lock-in, a

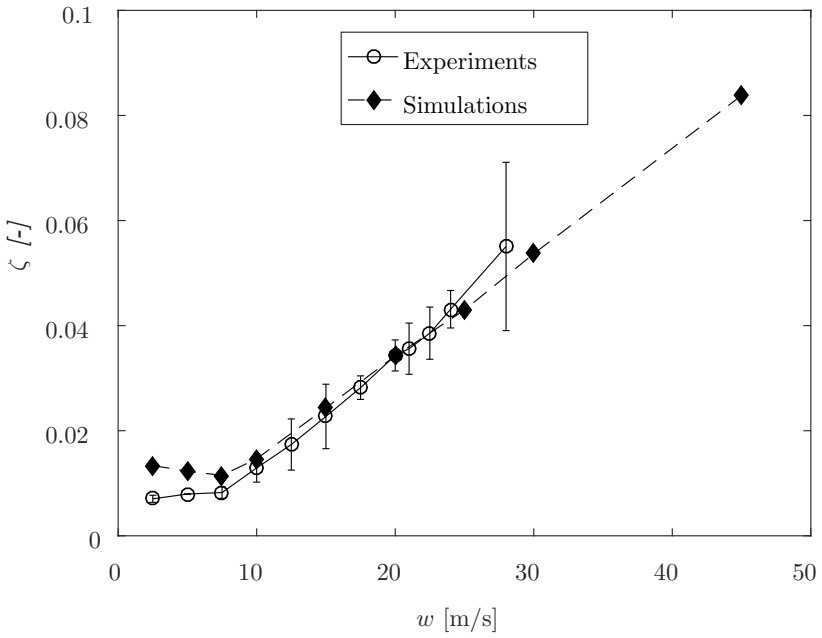

Figure 5. Experimental and numeric results for F1 . Note that both the experimental and numerical results indicate a change around the lock-in region (at 8 m/s), but they differ in the results below lock-in.

Table 2. Maximum Vibrational Amplitudes

Excitation Source	F0	F1
MFC	0.085 mm	0.125 mm
Vortex Shedding	0.013 42 mm	1.4×10^{-9} mm

behaviour that is not reflected in F1 . The order of increase seems to be quite similar as well, around a 0.1% increase for each m/s

The maximum vibrational amplitudes for F0 and F1 are shown in table 2. As the results indicate, the effect of vortex shedding is virtually non-existent for F1 , whereas the shedding-related vibrational amplitude for F0 is at approx. 16% of the maximum excited amplitude.

4. Discussion

The measurements were limited to 28 m/s due to cavitation, but the numerical analysis indicates that the trend is likely to continue at least up to 45 m/s, see figure 5. Given the similarities between the numerical and experimental results at velocities up to 28 m/s, there simulations performed at 45 m/s are most likely accurate.

At this stage, it is relevant to make comparison to other similar measurements, mainly those of Coutu et al [4], where a hydrofoil has been mounted in a fixed-beam configuration, and modal testing was done for velocities up to 25 m/s; and those of Yao et al [6], where the effect of the trailing edge shape was tested on a cantilever beam.

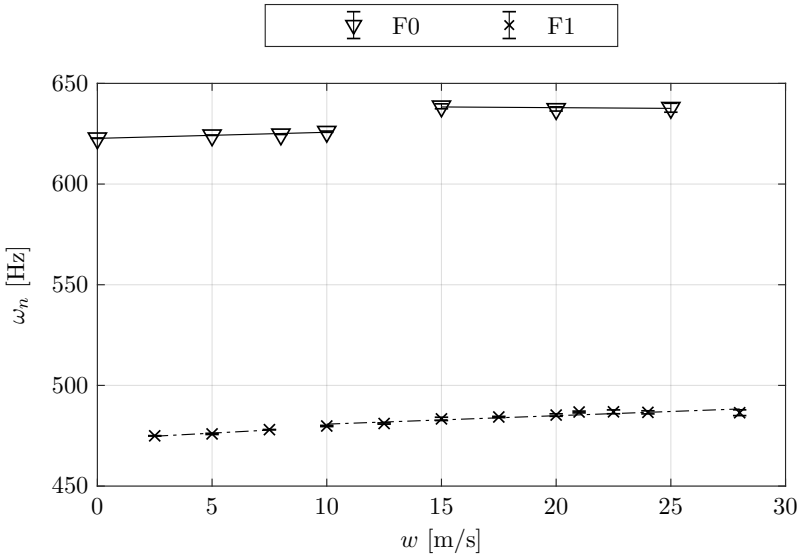

Figure 6. Natural Frequency. Note that there is a slight increase in natural frequency for both F0 and F1 .

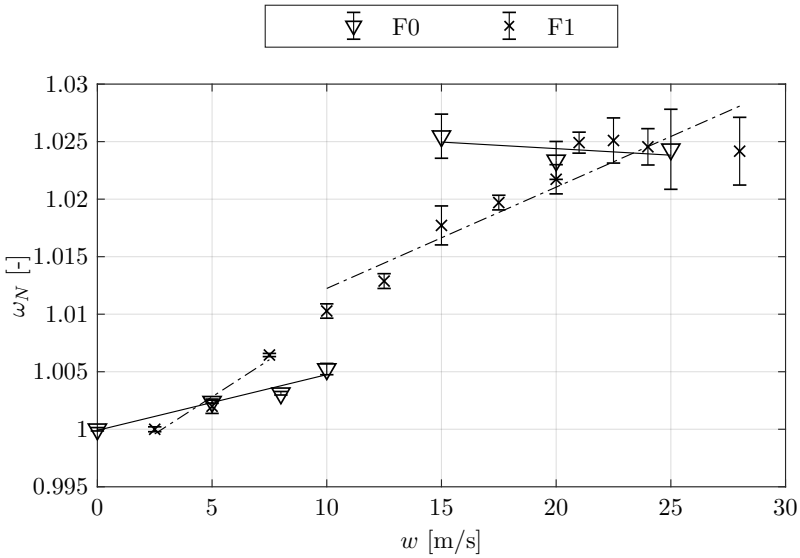

Figure 7. Normalized natural frequency. Note that both F1 and F0 appear to approach a constant value at 1.025.

Coutu et al found that the damping factor was consistently increasing with water velocity, without any discontinuities, but only above lock-in velocity. Comparing with Yao et al, a discontinuity in damping slope was observed at lock-in for the torsional bending mode, which for a cantilever beam is quite similar to the bending mode of a fixed-beam foil. Said discontinuity was observed at lock-in, which agrees very well with the trends observed in the present work.

In order to make a quantitative comparison to the results obtained by Yao et al, consider figure 8. Here, the damping is presented as a function of the *reduced velocity*, C^* , defined by Equation 1.

$$C^* = \frac{w}{L \cdot \omega_n} \tag{1}$$

As Figure 8 shows, the slope of the damping factor change is nearly identical for F0 and F1 when plotted against their reduced velocities. Compared with figure 9, it is clear that the observed damping behavior is similar in scale.

The slope of the damping change measured in the present work agree adequately with the measurements conducted by Yao et al, in which the slope of the damping was approx. 3.9×10^{-3} (when the velocity is expressed in absolute terms), as compared to approx. 2×10^{-3} obtained in this work. In the work of Coutu et al, the damping factor slope was found to be 1.07×10^{-2} to 1.23×10^{-2}, approx. 5 times higher than the results from this work. This result was fairly consistent for all the geometries tested by Coutu. Even if the geometry of the hydrofoils differ within each experiment, the dimensions for the test section remains.

Another key feature in the work of Yao is the apparent jump in natural frequency observed at lock-in, something that was also seen in the present measurements. Coutu et al found that the natural frequency remains constant, but CFD simulations performed by Nenneman et al [14] indicate that the natural frequency does indeed increase with velocity. The present results, and those of Yao, found that the natural frequency does change through the lock-in region, but there is no conclusive experimental evidence of further trends above lock-in. It could very well be the case that it is constant above lock-in.

Previous results have indicated that the phase shift in vortex shedding is the main contributor to the observed discontinuity in the evolution of the damping factor[12], but the present results contradict this. It is difficult to argue that the vortex shedding is the main contributor to the increase in damping when the same behavior is observed for both F0 and F1 , even if the magnitude of the vortex shedding is quite different for the two test specimens.

The divergence in the present results, along with those of Coutu and Yao, raises the question of dimensionlessness: To what degree do we expect the damping factor to be dependent on the geometry and/or scale? Since the geometries in question differ, the proportion between the added mass and the blade stiffness is varying, which could cause different hydrodynamic behavior. It is also interesting to address the validity of the assumption of linearity in the vibrating system. Most theory regarding vibrating structures assume linearity, ie. spring force linearly proportional with displacement, damping force linearly proportional with velocity [13]. This may not be the case when the effects of FSI are prevailing[11]. There is lacking documentation on the effect of non-linearities in turbine blades, but the difference in scale between the prevailing experiments in this field suggest that the relative scale of the hydrofoil could be crucial to the expected rise in damping factor.

5. Conclusion

The present measurements show that the damping factor of a hydrofoil behaves differently above and below lock-in conditions, and the natural frequency is also affected by this. The two different test geometries indicate that a more slender blade might produce a lower natural frequency, having a reduced stiffness with the same oscillating mass, due to the larger relative

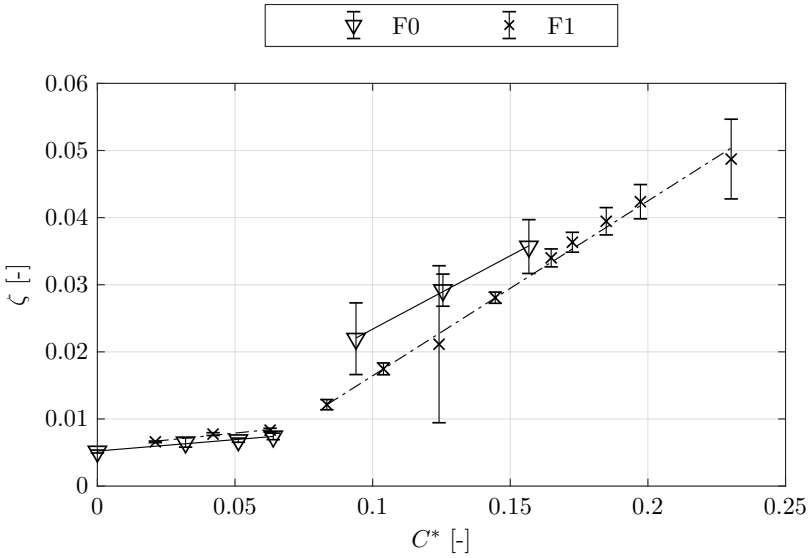

Figure 8. Damping vs reduced velocity.

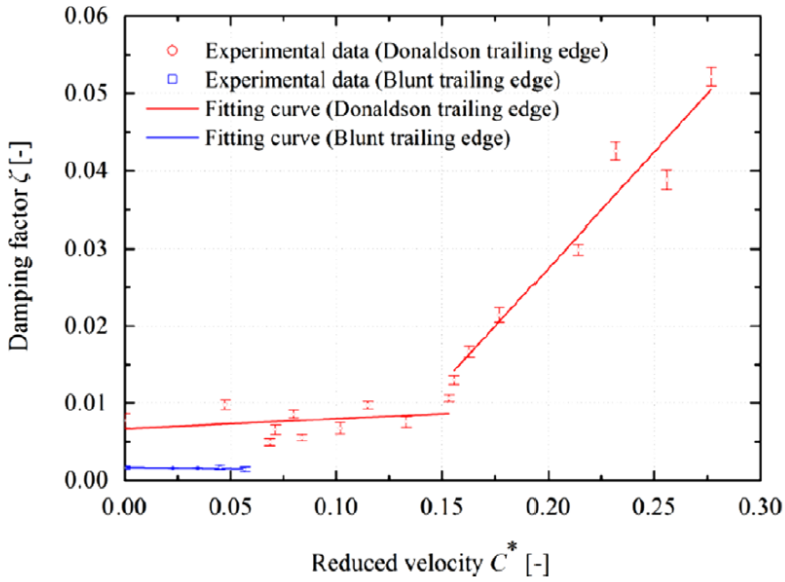

Figure 9. Measurements preformed by Yao et al [6].

contribution from the water. Comparisons with similar experiments indicate that the increase in damping factor will be smaller for a stiffer hydrofoil, due to the reduced relative influence

of the fluid and the inherent non-linearities in a fluid-structure vibration. This could arguably be extended to encompass similar geometries of different scale, meaning that different types of turbines, with different relative blade thickness might have very different damping evolution with respect to the changing water velocities.

6. Further Work

Further investigations of damping behavior in submerged hydrofoils should include a thorough assessment of the linearity of the vibrating system. In addition, focus should be placed upon understanding the behavior of the natural frequency above lock-in, as the present measurements are inconclusive. Additionally, all the work performed on vibrating hydrofoils has focused on a single blade in vibration. Further measurements will encompass a multi-blade cascade, in order to capture influence from neighbouring blades.

7. Acknowledgements

The research was carried out as a part of HiFrancis, a high-head Francis turbine research program supported by the Norwegian Research Council, The Norwegian Hydropower industry, and the Norwegian Center for Hydropower.

[1] Gagnon M and Thibault D 2015 *Proc. 6th IAHR International Meeting of the Workgroup on Cavitation and Dynamic Problems in Hydraulic Machinery and Systems*
[2] Flores M, Urquiza G and Rodríguez J M 2012 *World J. Mech* **2** 28–34
[3] Trivedi C 2017 *Eng. Fail. Anal.* **77** 1 – 22
[4] Coutu A, Seeley C, Monette C, Nennemann B and Marmont H 2012 *IOP Conf. Ser.: Earth Environ. Sci.* **15** 062060
[5] Roth S, Calmon M, Farhat M, Münch C, Bjoern H and Avellan F 2009 *Proc. 3rd IAHR International Meeting of the Workgroup on Cavitation and Dynamic Problems in Hydraulic Machinery and Systems* **1** 253–260
[6] Yao Z, Wang F, Dreyer M and Farhat M 2014 *J. Fluids Struct.* **51** 10. 189–198
[7] Reese M C 2010 *Vibration and Damping of Hydrofoils in Uniform Flows* Master's thesis Pennsylvania State University
[8] Tengs E O, Bergan C W, Jakobsen K R and Storli P T 2018 *Proc. 29th IAHR Symp. on Hydraulic Machinery and Systems (Kyoto) IAHR2018-033* (to be presented)
[9] Monette C, Nennemann B, Seeley C, Coutu A and Marmont H 2014 *IOP Conf. Ser.: Earth Environ. Sci.* **22** 032044
[10] Seeley C, Coutu A, Monette C, Nennemann B and Marmont H 2012 *Smart Mater. Struct.* **21** 035027
[11] Ewins D J 2000 *Modal Testing: Theory, Practice, and Application* 2nd ed (*Mechanical engineering research studies* no 10) (Research Studies Press)
[12] Bergan C W, Solemslie B W, Østby P and Dahlhaug O G 2018 *Int. J. Fluids Mach. Syst.* **11** 146–153
[13] Craig R R, Kurdila A and Craig R R 2006 *Fundamentals of Structural Dynamics* 2nd ed (John Wiley)
[14] Nennemann B, Monette C and Chamberland-Lauzon J 2016 *IOP Conf. Ser.: Earth Environ. Sci.* **49** 072006

Paper 6

PIV Measurements and CFD Simulations of a Hydrofoil at Lock-in
Sagmo, K. F., Tengs, E. O., Bergan, C. W., and Storli, P. T.
presented at 29th IAHR Symposium on Hydraulic Machinery and Systems, Kyoto, Japan, September 15-20, 2018. Proceedings to be published 2019

PIV measurements and CFD simulations of a hydrofoil at lock-in

K F Sagmo[1], E O Tengs[1,2], C W Bergan[1] and P T Storli[1]

[1] Waterpower Laboratory, Norwegian University of Science and Technology, Alfred Getz Vei 4, 7491 Trondheim, Norway

[2] EDR & Medeso AS, Leif Tronstads Plass 4, 1337 Sandvika, Norway

E-mail: kristian.sagmo@ntnu.no

Abstract. As part of an ongoing investigation into the mitigation of vortex induced vibrations of hydrofoils, a combined experimental and numerical study of the fluid-structure interactions and wake of a hydrofoil at lock-in has been conducted at the Waterpower laboratory of the Norwegian University of Science and Technology. The hydrofoil has a blunt trailing edge and Von Karman vortex shedding induces a lock-in effect at a chord based Reynolds number of about $2{,}7{\cdot}10^6$. The present paper presents the initial measurements of vortex shedding frequencies going through lock-in, along with CFD simulations at lock-off conditions as well as some empirical estimates of vortex shedding. Experimentally the hydrofoil wake was studied in detail using particle image velocimetry (PIV). Hydrofoil vibration frequencies were measured by both a strain gauge positioned near the trailing edge of the foil as well as by a laser doppler vibrometer (LD-V). Numerically the phenomena was simulated using ANSYS CFX. Several different turbulence models was tested, from the two-equation standard $k-\epsilon$ model to the scale adaptive SST-SAS model, with considerably different results. It is observed that the vibrations induced at lock-in considerably shifts and reduces the hydrofoil wake velocity deficit. Further, the CFD results suggest that the driving parameter influencing the shedding frequency is the cross flow separation distance at the trailing edge.

1. Introduction

In order to avoid unnecessary fatigue and risk of failure when designing hydraulic turbines, it is an established guideline that the shedding frequency of guide vanes, stay vanes, and runner blades should not overlap with the natural frequencies of the blades in the range of operation [1]. According to Blake et al. [2], the recognition of the link between the trailing edge geometry and vortex shedding became widespread in the 1960's. However, as has been indicated by several researchers, the task of predicting the shedding frequency from a blunt trailing edge strut or hydrofoil can be difficult due to it being highly sensitive to both tip geometry as well the surrounding flow conditions affecting the boundary layers [3]. Nevertheless, for trailing edges with sharp edges and clearly defined separation points modern CFD methods have proven effective [4]. In modern installments of hydraulic turbines limits are constantly being pushed with respect to increasing the performance of components, while at the same time reducing material- and manufacturing costs. Accurate prediction of component behavior becomes more important because safety and expected lifespan must be kept at acceptable levels. For components which objective is to transfer forces to or from fluids, this continuous process might push the components into designs where the structure and fluid are mutually changing the

behavior of each other. This is when prediction of the behavior of the dynamics of the system becomes more involved [5]. In an effort to shed more light on the topic at hand, a combined numerical and experimental investigation is underway at the Norwegian University of Science and Technology (NTNU) for a hydrofoil under lock-in conditions. We present here some initial results.

2. Methods

2.1. Experimental Setup

2.1.1. PIV and frequency measurements setup The general layout of the experimental setup is illustrated in figure 1 a) and b). All measurements were done with the hydrofoil centerline angled parallel to the incoming flow field, i.e. 0 degrees angle of attack. The test section volumetric flow rate was measured by an ABB electromagnetic flow-meter located downstream of the test section. The maximum standard deviation in the mean flow during measurements was approximately 0.11 %, while the average temperature was 20.5±1.5 Celsius, giving an approximate chord based Reynolds number uncertainty of 3.65 %.

The hydrofoil vibration frequencies and amplitudes were measured with a strain-gauge located near the trailing edge at approximately mid-span, as well as with a surface laser doppler vibrometer (LD-V) pointing at the trailing edge. Data acquisition was managed with National Instruments (NI) LabVIEW and NI data acquisition devices (DAQ's). Sensor output voltages were sampled at 10 kHz, giving more than 10 samples per period for the frequencies investigated. For a more detailed explanation of the hydrofoil instrumentation, material properties and natural frequencies see Bergan et. al [6]. The frequency amplitude spectra later presented were obtained by performing a P.D. Welch power spectrum analysis in MATLAB with a Hanning window. As a means of smoothing the amplitude spectra the sensor signal were split into varying lengths relative to the approximate shedding frequencies measured, with a 50 % segment overlap.

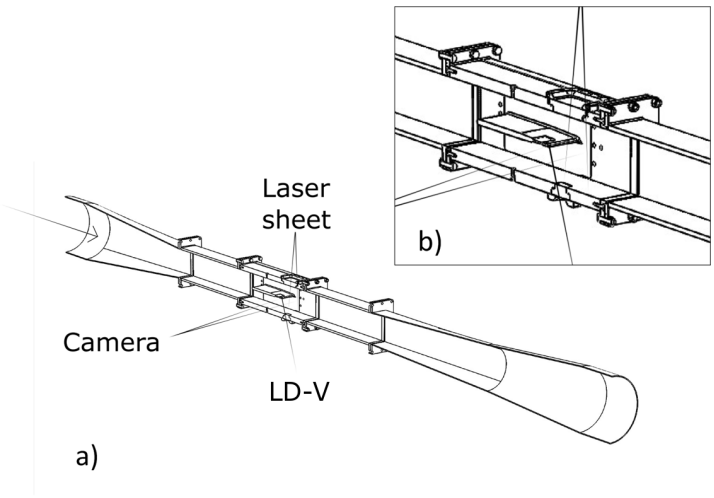

Figure 1: Section view of the experimental test setup. b) gives an enlarged view of the rectangular test section and positioning of the hydrofoil.

The recording of the 2D PIV vector field in the wake of the hydrofoil was conducted with a high speed system provided by LaVision GmBH. Full resolution images of (1284 x 1024) pixels (px) were recorded in double frame mode at a sampling rate 2.4 kHz, with the camera

oriented perpendicular to the illumination plane. The image sampling duration for each recorded image set was about 2 s. Table 1 gives a summary of the recording parameters. The recording parameters were balanced such that the average image size of a tracer particle was about 2.4 px and the estimated particle displacement between each frame was about 5-6 px. Vector fields were evaluated using a multipass method, stepping from a 96 px x 96 px interrogation area (IA) with a 50 % overlap to a 64 px x 64 px IA with a 75 % overlap. This gave an average number of illuminated particle image pairs within each area of roughly 10. According to the synthetic PIV image generation evaluation described by Raffel et. al [7] these are image parameters that should give relatively low root mean square (RMS) random errors in the cross correlation evaluation of the vector fields. The degree of peak locking was investigated and found to be acceptably low. The image scaling calibration RMS error of the 3'rd order polynomial fit was about 0.38 px for the reported measurements.

Table 1: PIV recording parameters for the hydrofoil wake flow measurements

Field of view (FOV) / Area of interest	21.1 mm x 16.9 mm / 1280 px x 1024 px (x-y)
Interrogation volume / Interrogation area	1.06 mm x 1.06 mm x 0.5 mm / 64 px x 64 px (x-y)
Experimental velocity range	(8 - 14) m/s
Observation distance & Lens F-number	215 mm & 5.4
Recording method & Camera sensor	Double frame/Double exposure & CMOS
Exposure time & image acquisition rate	250 μs & 2.4 kHz
Image processing mode	cross-correlation
Mean tracer particle diameter d_p	13 μm
Tracer particle density δ_p	1.1 g/cm^3
Illumination source	Nd:YFL dual cavity laser, 527 nm wavelength

To compute the uncertainty, $\triangle U$ in the time-averaged stream wise velocity U distributions later presented, the following estimate was applied [8];

$$\triangle U = \frac{\sigma_U}{\sqrt{N_{eff}}}, \tag{1}$$

where σ_U denotes the standard deviation in U across all samples during a measurement series and $\sqrt{N_{eff}}$ is the effective number of independent samples of U. $\sqrt{N_{eff}}$ involves the computation of the auto-correlation of the time-series of the instantaneous stream wise velocity vectors $u(x, y, t)$ and approaches the total number of samples N in a signal in the case that the samples of u are completely independent. Finally, the error in U due to uncertainty in the the laser-plane span-wise position was investigated by measuring the hydrofoil wake at a parallel 10 mm offset plane. While the test clearly indicated 3D effects coming from the test section channel walls, the relative uncertainty in the positioning of the laser plane on the scale of 0.5 mm should have negligible impact on the time-averaged wake velocity distributions.

2.1.2. Hydrofoil Profile Geometry and Surface Roughness To facilitate comparison with CFD simulations the hydrofoil surface roughness was measured with a profilometer at different chord-wise positions, giving a maximum arithmetic roughness average R_a of about 5.8 μm near the leading edge. Following Shclichting & Gersten [9], we approximate the technical roughness height by $k_{tech} = 3.5R_a$. For a maximum chord based Reynolds number of approximately $Re_C = 4.5{\cdot}10^6$ this gives for a fully turbulent boundary layer an estimated k^+ value of approximately 11. Hence we assume that the surface roughness height exceeds the viscous sub-layer near the leading edge and may play an important effect in the development of the boundary layer.

Figure 2 shows the blade geometry. The hydrofoil surface position data was measured with a Leitz PMM-C 600 coordinate machine, capable of a repeat-ability range of less than 0.6 μm. These measurements were performed after the foil had been coated with a thin layer of matte black paint, to avoid unnecessary laser reflections in the PIV measurements. Figure 2(b) shows the measured trailing edge along with the numerical grid points along the blade used in the CFD simulations. A noticeable difference is only visible at the steepest part of the trailing edge, where the flow is assumed to be separated. Hence any considerable differences in between the results from the measurements and the simulations are assumed not to stem from differences in the profile geometry.

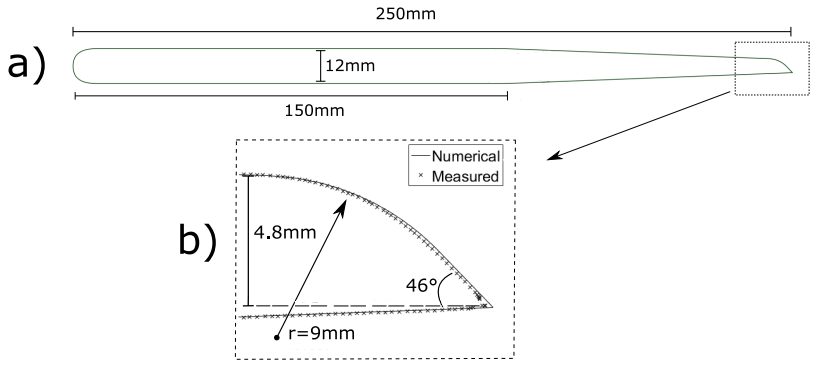

Figure 2: a) Blade geometry. b) Measured trailing edge geometry plotted along the numerical grid wall cells.

2.2. Numerical Setup

A numerical study was performed to investigate how well the shedding phenomena is predicted in the lock-off region. The numerical simulations was purely Computational Fluid Dynamics (CFD), i.e. no structural response. The simulations was performed in ANSYS CFX. The numerical domain and computational grid is illustrated in figure 3. The channel extends $>> 10D_h$ upstream of the blade to ensure that the flow entering the test section is fully developed [10]. The domain was also extended downstream to minimize the risk of back-flow and outlet conditions affecting the blade vortex dynamics. The inlet boundary condition was static pressure, and the outlet condition was a mass flow corresponding to the different flow velocities. The turbulence intensity at the inlet was tested in the range $I \in [0\% - 10\%]$, with no noticeable difference in the turbulence levels in the test section.

The mesh was created in ANSYS ICEM CFD, and contained about 13 million, all hexahedral elements. When refining the mesh, it was observed that the coarser mesh simulations under-predicted the shedding frequency. On the final mesh, for a typical flow velocity tested in this article, U_{ref}=11 m/s, the maximal y^+ value was 1 and ≤ 0.5 at the leading and trailing edge, respectively. As an implicit numerical solver was used the time-step was chosen to be 8e-5 s, giving a corresponding Courant number of 3. Shedding frequencies in the order of $f = 500$ Hz were expected, and the time-step used corresponded to about 25 points per period. For the Reynolds Averaged Navier-Stokes based simulations several different turbulence models have been tested in order to investigate the effects on the predicted shedding dynamics. The standard $k - \epsilon$ model [11, 12], was expected in this case likely to struggle to give an accurate result, due to the known problems with separation and streamline curvature. Another two-

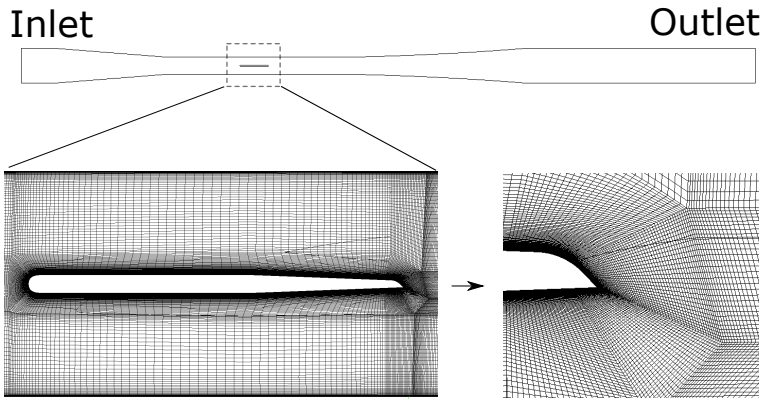

Figure 3: Numerical flow domain and mesh around blade

equation model, the Wilcox $k-\omega$ model [13, 14], was also tested, along with the $k-\omega$ SST [15], a combination of the two. Additionally, the scale-adaptive SAS-SST model [16] was tested. Given an adequate computational grid the SAS model resolves the larger turbulent structures, at increased computational costs. Further, 2-dimensional simulations was performed on a simplified, shortened test section to investigate means of speeding up the simulations.

2.3. Empirical estimates for vortex shedding

It may be interesting to compare the measured and CFD predicted shedding frequencies with some empirical estimates. The first empirical approach utilized in the present study is the traditional Strouhal shedding frequency [17], f_s, here defined as

$$f_s = \frac{St \cdot U_\infty}{D}, \tag{2}$$

where D in this case is approximated as the blade thickness at the trailing edge, St denotes the Strouhal number and U_∞ is the free stream velocity. For the chord based Reynolds number range encountered in this study, the Strouhal number was chosen to be $St = 0.22$, a commonly used value [18]. The thickness of the trailing edge, $D = 4.8$ mm, is measured at the point where the curved surface starts, see figure 2(b).

An empirical formula more specific for the Francis turbine and different trailing edge geometries is described in the paper by Brekke [1], where the frequency of the vortex shedding is approximated by:

$$f_s = 190\frac{B}{100}\frac{U_\infty}{(t+0.56)} \tag{3}$$

Here B is a constant linked to the trailing edge geometry, U_∞ is the free stream velocity, and t is the blade thickness in [mm]. The constant $B = 131$ is chosen from [1], and is related to a trailing edge geometry very close to the one tested here. Note however that in Brekke's considerations, all blade geometries had parallel upper and lower surfaces. This is not the case for the blade geometry in this study which has tapered surfaces toward the trailing edge. Hence, strictly $t \neq D$. Nevertheless equation 3 is used here in its current form.

2.4. Wall effects

The hydrofoil tested in this study has a front section area to test section area blockage ratio of 8 %, and requires a correction for the measured Strouhal number, St_{meas}, due to added wall effects[19, 20]. Following the considerations of Ota et al. [20] for incompressible flow over a 2D-geometry experimental setup, we estimate the correction factor, ϵ, by the following relation for the free stream Strouhal number St,

$$St = St_{meas}(1 - \epsilon\frac{t}{h}). \tag{4}$$

Here t denotes the height of the hydrofoil (12mm) and h the height of the measuring section (150mm), giving $t/h = 8\%$. The observed correction factor ϵ is here estimated by the assumed free stream Strouhal number of 0.22, and the measured Strouhal number outside the range of lock-in. Note that for the rough empirical estimates for the shedding frequencies later presented the free stream velocity is approximated as the average velocity across the undisturbed test section, such that $U_\infty = U_{ref}$, since, to the authors knowledge there is no reliable way to estimate the correction factor a-priori for the geometry tested in this study.

3. Results

Experimental results

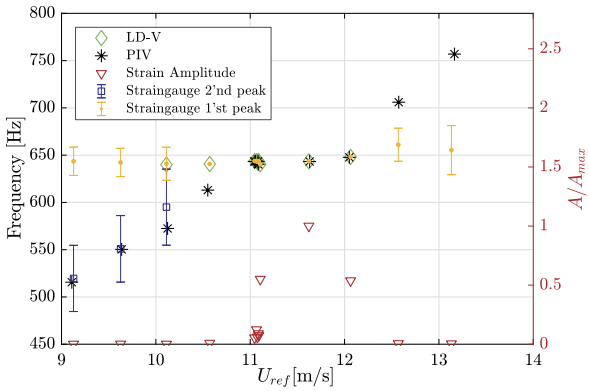

Figure 4: Hydrofoil vibration frequencies and shedding frequencies measured by PIV, strain-gauges and LD-Vibrometer. The relative hydrofoil vibrational amplitude is plotted along the right y-axis.

Figure 4 presents the hydrofoil vibration frequencies and shedding frequencies measured by PIV, strain-gauge and LD-Vibrometer. There is a precise agreement between the measuring techniques in lock-in, with resonance starting to occur at around 11.1 m/s as indicated by the sharp rise in the vibrational amplitude. The first, standing peak found in the strain-gauge frequency amplitude spectrum, presented for some velocities outside lock-in in figure 5, is identified as the hydrofoil natural frequency [6]. The second, broad ranged traveling peak found in the frequency spectrum in the strain measurements can be identified as the shedding frequencies in lock-off conditions, as indicated by the agreement with PIV measurements in the wake. Since the shedding frequency is assumed to be inherently gaussian about it's mean value, the size of the error bars given in figure 4 in the strain-gauge 2'nd peak was estimated by the half width at half maximum (HWHM) for the smoothed frequency distribution curves given in

figure 5. In lock-in, the uncertainty in the hydrofoil vibrational frequency was estimated by the standard deviation in peak frequency from repeated measurements at 11.1 m/s and found to be approximately 1.6 Hz.

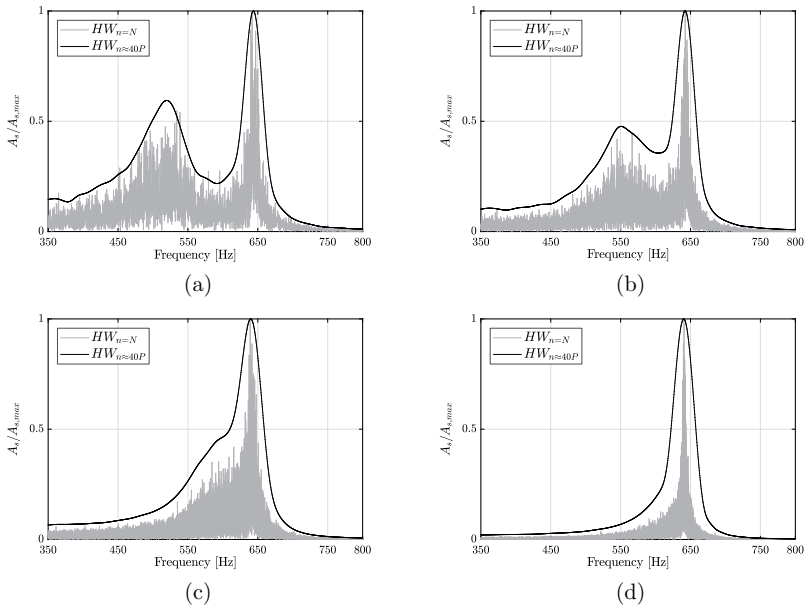

Figure 5: Amplitude frequency spectra for increasing reference velocities from strain-gauge voltage signal, showing the traveling shedding frequency peak (left peak) approaching the natural (standing) frequency peak of the hydrofoil. (a) U_{ref} = 9.1 m/s. (b) U_{ref} = 9.6 m/s. (c) U_{ref} = 10.1 m/s. (d) U_{ref} = 10.6 m/s.

The average observed Strouhal number, as found from frequency estimates by the PIV measurements given in figure 4 for reference velocities between 9.1 m/s and 10.6 m/s, is 0.274, with a standard deviation of about 1.3 %. The ratio between the assumed and the measured Strouhal frequency is ≈0.794, and from equation 4 this gives an average correction factor $\epsilon \approx 2.57$.

Figure 6 gives the normalised time-averaged streamwise velocity distribution in the hydrofoil wake measured by PIV at two downstream positions $x_1 = 9.9D$ and $x_2 = 13.3D$, measured from the trailing edge tip. Sets of varying reference velocities are included, both for lock-off (6(a)-(b)) and lock-in conditions (6(c)-(d)). It is noted that the wake velocity distributions varies considerably more during lock-in.

Numerical results

Figure 7 shows the stream-wise velocity at two vertical lines, $x_1 = 9.9D$ and $x_2 = 13.3D$, downstream of the blade at U_{ref} = 9.1 m/s. The velocities are time averaged over 2 s and ≈ 100 shedding periods in the experiment and simulations, respectively.

Next, the frequency of the shedding is compared in figure 8(a). The uncertainty in the fast Fourier transform of the simulated time-signal is estimated to be $\xi \approx 5$ Hz. We observe that a linear trend is found for all turbulence models, as is reported by most sources e.g. [17, 1], and thus it is assumed that the general vortex shedding phenomena is captured. For ease of comparison figure 8(b) shows the experimental and numerical results from the SAS simulations

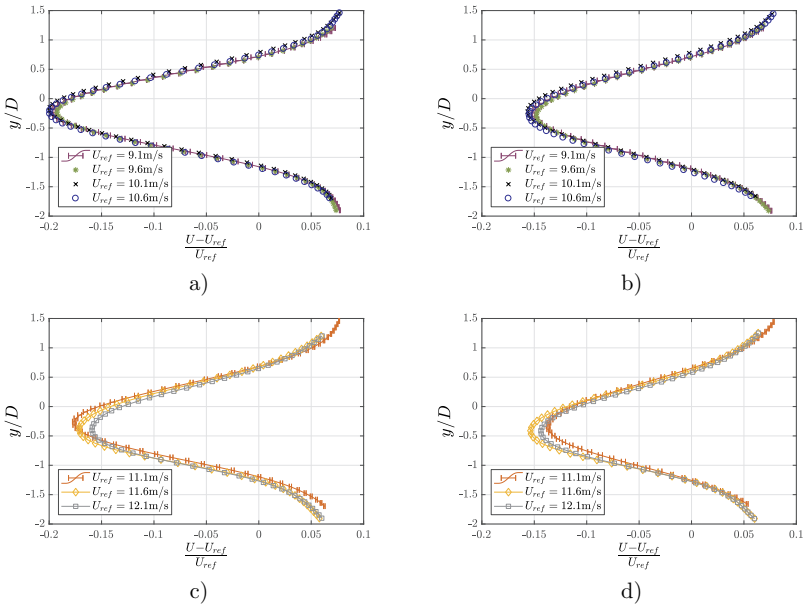

Figure 6: Time-averaged PIV measured velocity distributions normalised with respect to the mean channel velocity for different downstream positions. Height normalised by trailing edge thickness, with $y = 0$ set at the hydrofoil center line. In (a) and (c) x = $9.9D$. In (b) and (d) x = $13.3D$. Uncertainty error bars are only plotted for reference velocities of 9.1 m/s and 11.1 m/s, for clarity.

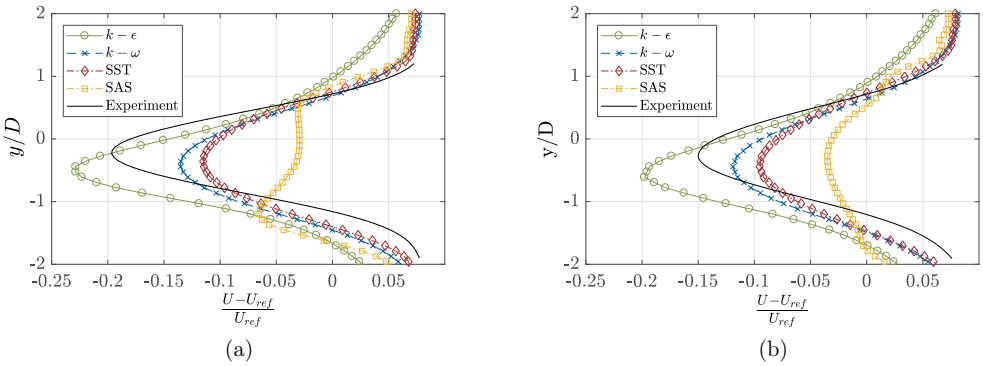

Figure 7: Experimental and numerical comparison of the time-averaged velocity profile downstream of the trailing edge. (a) $x = 9.9D$. (b) $x = 13.3D$.

together, along with empirical estimates for vortex shedding. Finally, figure 9 gives a comparison of the instantaneous velocity fields obtained with the different numerical schemes. The vertical black lines denotes one of the spatial locations of the PIV profile measurements ($x = 9.9D$)

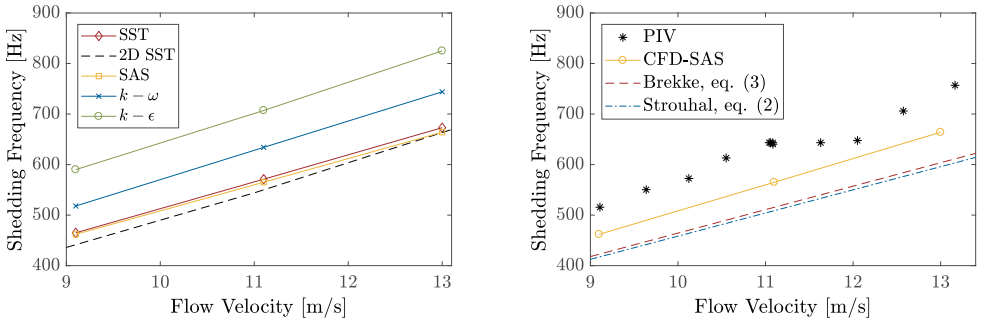

Figure 8: Shedding frequency versus flow velocity. (a) Effect of different turbulence models. (b) Experimental, CFD and empirical estimates.

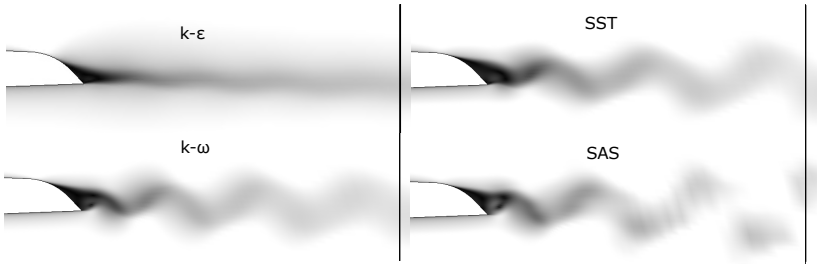

Figure 9: Trailing edge wake comparison using different turbulence models, $U_{ref} = 9.1$ m/s. Coloring according to fluid velocity with $u = 0$ m/s being black and $u = 9.1$ m/s being white.

4. Discussion

From Heskestad and Olberts [3] we note that according to their measurements, 3 geometries all similar in design to the foil under investigation here, gave a relative standard deviation in the shedding frequency Strouhal number of about 12%. This indicates that the trailing edge shedding frequency is quite sensitive to small changes in the geometry. Hence the error in the rough empirical estimates (equation 2 & equation 3) for the shedding frequencies of about 20% and the wall correction factor estimated to $\epsilon = 2.46$ is assumed to contain both wall effects as well as boundary layer separation effects specific to the hydrofoil and trailing edge geometry tested here. The level of the error is sobering, and illustrates the need for either model measurements or accurate case dependent numerical tools in the design phase of hydraulic turbine blade components, even in lock-of conditions.

Comparing experimental and numerical results in figure 7 we observe that the wake center is consistently shifted slightly below the hydrofoil center line, with about $0.2D$ in the experiments at lock-off conditions. It is believed that this is due to the asymmetry of the trailing edge, as the upper separation point is allowed to travel closer to the hydrofoil's centerline due to the relatively gentle curvature, effectively shifting the wake profile. In the simulations points of zero wall shear stress was investigated in order to study the separation points impact on the wake and shedding frequencies obtained. When different flow velocities are compared, the separation occurs later the higher the flow velocity. Correspondingly, the "perceived" thickness of the trailing edge is also thinner at higher speeds. When comparing the results from different

turbulence models at a fixed reference velocity it was also found that a delayed separation point corresponded to an increase in the shedding frequency. This indicates that the differences in the turbulence models lie in the simulated boundary layer and subsequently the numerical prediction of the boundary layer separation points. As an example, comparing results in figure 7-9, the $k-\epsilon$ model separated latest along the trailing edge, resulted in the highest shedding frequency and the most vertically shifted wake.

As an overall trend, the numerical simulations tended to underestimate the velocity deficit, except for the $k-\epsilon$ model, where the deficit was overestimated. The wake is considerably different depending on which turbulence model is used. From figure 9 we can start to understand why the different velocity profiles in figure 7 look like they do. In the SAS model, the wake breaks down into smaller vortexes, and thus the mean flow in the wake is higher and flatter. This corresponds to the lower velocity deficit in figure 7. Similarly, it can seem like the $k-\epsilon$ model have the strongest velocity deficit and widest wake. It is also observed that the oscillations in the $k-\epsilon$ wake are very small. Compared to the PIV measurements, the SAS model performs qualitatively best (not shown), while interestingly, figure 7 indicates that the mean velocity distribution is farthest from the experimental values for this model.

Figure 8 (a) show the trends of the shedding frequency for different turbulence models. A linear best fit is performed and the slopes are used as comparison. The slope is varying with $\approx 22\%$, from $k-\epsilon$ to SAS. The SST and the SAS model perform very similarly. 2-dimensional simulations with the SST turbulence model is also included in figure 8 (a). Clearly, they provide some predictive value while also providing a significant speedup factor, in this case, of $\approx 70\times$. When comparing the numerical and experimental results in figure 8 (b), it is seen that there is a general under prediction of the shedding frequency by the numerical simulations. Based on the slope of the experimental results after a linear best fit the offset between the SST and SAS model compared to the experimental values are $< 4\%$, while the numerically observed Strouhal number is about 10 % lower than the comparatively obtained experimental Strouhal number of 0.274 in lock-off conditions. A closer investigation of the possible reasons for the relative offset between the CFD calculations and the experimentally obtained results are part of future work, along with simulations utilizing a fluid-structure interaction coupling for numerical investigation of the hydrofoil behaviour in lock-in.

5. Conclusion

The wake and shedding frequencies from a hydrofoil with a blunt, asymmetrical trailing edge has been investigated for free-stream velocities where turbulent von-karman vortexes incites a lock-in effect. At lock-in we observe larger stream-wise velocity fluctuations in the hydrofoil wake, than in lock-off conditions, likely due to wandering of the upper separation point at the trailing edge tip. Experimentally obtained shedding frequencies has been compared to numerical simulations as well as empirical estimates. The relative differences between simulations with different turbulence models clearly indicate the difficulties in the modelling of the separation points and subsequent wake characteristics crucial to estimating the risk of lock-in at the design phase for a hydraulic turbine blade component. The numerically obtained results for the trend in the shedding frequencies are in relative agreement with previous studies for similar trailing edge geometries [3], indicating that a delayed separation point leads to increased shedding frequencies.

Acknowledgments

Magne Tveit Bolstad is gratefully acknowledged for his assistance during measurements and help in design of the experimental setup. Thanks also to Prof. Knut Sørby for his assistance in measuring the hydrofoil surface roughness and geometry.

References

[1] Brekke H 1994 *Proceedings of the 17th IAHR Symposium, Beijing, China* pp 15–19
[2] Blake W K 1984 *Journal of Vibration, Acoustics, Stress, and Reliability in Design* **106** 351–363
[3] Heskestad G and Olberts D R 1960 *Journal of Engineering for Power* **82** 103–09
[4] Do T, Chen L and Tu J 2010 *Journal of Fluids and Structures* **26** 1155 – 1173
[5] Liaghat T, Guibault F, Allenbach L and Nennemann B 2014 *ASME 2014 International Mechanical Engineering Congress and Exposition* **4A**
[6] Bergan C, Solemslie B, Østby P and Dahlhaug O G 2018 *International Journal of Fluid Machinery and Systems* Accepted
[7] Raffel M, Willert C E, Wereley S and Kompenhans J 2007 *Particle image velocimetry: a practical guide* 3rd ed (Heidelberg ; New York: Springer) ISBN 978-3-540-72307-3
[8] LaVision GmbH 2017 Lavision software davis 8.4 product-manual, item-number: 1105xxx document name: 1003001 DaVis D84.pdf
[9] Schlichting H and Gersten K 2017 *Boundary-Layer Theory* 9th ed (Berlin Heidelberg: Springer-Verlag)
[10] Yunus A C and Cimbala J M 2006 *Fluid mechanics fundamentals and applications* (International Edition, McGraw Hill Publication)
[11] Launder B E and Spalding D B 1983 *Numerical Prediction of Flow, Heat Transfer, Turbulence and Combustion* (Elsevier) pp 96–116
[12] ANSYS Inc 2017 *ANSYS 18.2 Documentation, The k-epsilon Model in ANSYS CFX*
[13] Wilcox D C 1988 *AIAA journal* **26** 1311–1320
[14] ANSYS Inc 2017 *ANSYS 18.2 Documentation, The k-omega Models in ANSYS CFX*
[15] Menter F R 1994 *AIAA journal* **32** 1598–1605
[16] Menter F and Egorov Y 2005 *43rd AIAA Aerospace Sciences Meeting and Exhibit* p 1095
[17] Strouhal V 1878 *Annalen der Physik* **241** 216–251
[18] Hartog D and Pieter J 1985 *Mechanical vibrations* (Courier Corporation)
[19] West G S and Apelt C J 1982 *Journal of Fluid Mechanics* **114** 361
[20] Ota T, Okamoto Y and Yoshikawa H 1994 *Journal of Fluids Engineering* **116** 414–18

Paper 7

Numerical Simulation of the Hydrodynamic Damping of a Vibrating Hydrofoil

Tengs, E. O., Bergan, C. W., Jakobsen, K-R., and Storli, P. T.

presented at 29th IAHR Symposium on Hydraulic Machinery and Systems, Kyoto, Japan, September 15-20, 2018. Proceedings to be published 2019

Numerical simulation of the hydrodynamic damping of a vibrating hydrofoil

E O Tengs [1,2], C W Bergan [1], K-R Jakobsen [2] and P T Storli [1]

[1] Waterpower Laboratory, Norwegian University of Science and Technology, Alfred Getz Vei 4, 7491 Trondheim, Norway

[2] EDR & Medeso AS, Leif Tronstads Plass 4, 1337 Sandvika, Norway

E-mail: erik.tengs@edrmedeso.com

Abstract. The periodic loads from Rotor-Stator interaction is believed to be the main fatigue contributor in High Head Francis turbines. The calculation of the structural response, and thus fatigue, is heavily reliant on the proper hydrodynamic damping characteristics of the water - structure system. The relationship between the water velocity and the hydrodynamic damping is also of great interest. To investigate this, the hydrodynamic damping characteristics of a submerged hydrofoil is simulated in ANSYS CFX. A one-way coupling is implemented, where the blade is forced to vibrate with the first bending mode at the natural frequency, while the hydrodynamic work is calculated over a vibrational period. The velocity of the flow over the hydrofoil is varied in the range v = 2.5 - 45 m/s. Two distinct damping regimes are observed depending on whether the vortex shedding frequency is below or above the lock-in region. The hydrodynamic damping is approximately constant before, and linearly increasing after this region. Experimental data from the Norwegian University of Science and Technology is available for validation, and shows the same trends. The sensitivity with respect to maximum vibrational amplitude is tested, and shows that the hydrodynamic damping is independent of the amplitude as long as the deflections are small.

1. Introduction

Several high head Francis turbines have had failures in the last decades [1, 2]. The reason is thought to be complex fluid-structure interaction in the runner, a resonance issue originating in the pressure field created from the interaction between the stationary and rotating components, known as Rotor-Stator Interaction (RSI) [3]. When designing a turbine, it is desired that the natural frequencies of the structure is far away from the known RSI frequencies. However, the presence of water, a relatively heavy fluid, severely changes structural response under loading. This complicates the calculations of the structural properties. The added mass effects tend to reduce the natural frequencies of the structure, as well as dampening the amplitude of the excitation [4]. In some rare situations, the different vibration modes may even change order [5]. Many have tried to obtain a rule of thumb with regards to the reduction of the natural frequencies, however this has not been found, and may not even be possible [4, 5, 6]. When solving for the frequency response in a submerged Francis turbine, a coupled acoustic-structural simulation is therefore necessary. A crucial input to such simulations is the hydrodynamic damping. As additional complexity, the water in a turbine is not stationary, in a high head Francis turbine, the relative

velocity between blade and water may reach v > 40 m/s. The effect of the moving water on the damping is therefore of great interest, and has been studied experimentally earlier [7, 8, 9]. The general trend is that the hydrodynamic damping is increasing as the flow velocity increase. A general recommendation as to the slope is however not obtainable. The maximal flow velocity in the abovementioned experiments was v ≈ 20 m/s. As far as numerical approximations, Monette et al. [10] provided a mathematical description of the hydrodynamic damping phenomena, and Liaghat et al. [11] performed a two-way fluid-structure coupled simulation on the same geometry. Similar experiments at the Norwegian University of Science and Technology have lately reached v ≈ 30 m/s over the hydrofoil, and also investigated the effects of the lock in region on the damping [12]. This article will try to replicate these experiments numerically, i.e. obtain the hydrodynamic damping coefficient in a system where water is flowing over a vibrating hydrofoil at different velocities. A one-way coupling of the fluid and structure will be performed to reduce the computational cost. The effects of the lock-in region on the damping will also be investigated.

1.1. Dynamic systems

Second order oscillating systems have the following form;

$$M\ddot{u} + C\dot{u} + Ku = F \tag{1}$$

Where M, C, K is the mass, damping and stiffness matrices respectively, u denotes the structural deflection, and F is the loading. Dot notation denotes a one-time differentiation with respect to time, meaning $\dot{u}$ represents velocity and $\ddot{u}$ represents acceleration. The structural deflection is assumed to be periodic with amplitude $u = u_o$ and frequency ω; $u = u_o sin(\omega t)$. A crucial input to the above equation is the damping. There exist several different types of damping, in the normal damping model there is viscous, frequency-dependent damping, but there is also material, frequency-independent damping [13]. In water, the viscous damping has been found to dominate the material damping [14]. The scope of this paper is therefore limited to obtaining the viscous damping ratio.

2. Methods

2.1. Hydrodynamic damping

In order to obtain the viscous damping ratio, we need to derive an expression for the damping effects of the water surrounding a structure. The damping ratio, ξ, of a second order system described by equation (1) is by definition [13]:

$$\xi = C(2M\omega)^{-1} \tag{2}$$

However, obtaining the mass and the damping coefficients is not as easy as in a classical mass – spring - damper system. We need to develop other parameters which can replace the unknowns in equation (2). In the following we show that the hydrodynamic work extracted from a CFD analysis help us doing this.

Assuming linear behaviour, the structural deformation, u, can be decomposed into a superposition of the different structural modes, Φ_i , where a mode is the oscillating shape of a system vibrating at its natural frequency [13].

$$u = \sum_{i}^{k} \Phi_i q_i \tag{3}$$

Where q_i is a scaling factor. The second order oscillating structural system, equation (1), can be rewritten using the above definition (using only one mode);

$$\Phi^T M \Phi \ddot{q} + \Phi^T C \Phi \dot{q} + \Phi^T K \Phi q = \Phi^T F \tag{4}$$

Let the coefficients still be denoted M, C, K, F for simplicity. The coefficient of $\ddot{q}$ is usually normalized such that $\Phi^T M \Phi = 1$ [15]. The second order system can now be written as;

$$\ddot{q} + C\dot{q} + Kq = F \tag{5}$$

Damping extracts energy from the blade. We are therefore interested in the work, $W = \int F\, dx$, over a period. The scaling factor will be periodic, $q = q_o sin(\omega t)$, as it follows the structural deflection, per equation (3). Integrating the left-hand side of equation (5) shows that only the first order term, $\int C\dot{q} dq$, yields a non-zero result over a vibrational period. The work is therefore as follows;

$$W = \int C\dot{q} dq = \int_0^T C\dot{q}^2 dt = C \int_0^{2\pi/\omega} [q_0 \omega \cos(\omega t)]^2 dt = C\pi\omega q_0^2 \tag{6}$$

Additionally, the hydrodynamic work, the work from the structure to the fluid, can be defined as:

$$W = -\int_0^T \int_A p \cdot \dot{u}_n dA dt \tag{7}$$

Where T is one period, p is the fluid pressure, and $\dot{u}_n$ is the velocity of the surface of the structure in the normal direction. Combining equations (2) and (6) finally leads to the definition of the hydrodynamic damping ratio;

$$\xi = \frac{W}{2\pi M \omega^2 q_0^2} \tag{8}$$

Where W is the hydrodynamic work, equation (7), M = 1 [kgm^2] is the modal mass, ω is the angular velocity [rad/s], and q_0 the scaling factor [-]. The hydrodynamic work is obtained from a CFD simulation, the other parameters are obtained from a modal analysis.

2.1.1. Flutter. Hydrodynamic flutter denotes the possibility of negative damping, an instable vibrational system. If certain requirements are met, the fluid flow could transfer energy to the hydrofoil, rather than absorb energy. The system vibration would in that case be self - magnifying, and violent failure could occur. Starting with equation (7). The work per cycle from the fluid to the blade is as follows follows:

$$W = \int_0^T \int_A p \cdot \dot{u}_n dA dt \tag{9}$$

For simplicity we rewrite $p\int dA = F$ to obtain

$$W = \int_0^T \dot{u}_n F dt \tag{10}$$

Assuming harmonic motion of the blade, $u = u_0 sin(\omega t)$ and thus, blade velocity $\dot{u} = \omega u_0 cos(\omega t)$. Let the force follow a similar harmonic motion, oscillating prior to the displacement with a phase angle $\Delta\phi$, $F = F_0 sin(\omega t + \Delta\phi)$. Solving the above integral for one period:

$$W = \omega u_0 F_0 \int_0^{2\pi/\omega} \cos(\omega t)\sin(\omega t + \Delta\phi)dt = \omega u_0 F_0 \sin(\Delta\phi) \tag{11}$$

We see that the work is purely controlled by the phase difference $\Delta\phi$. A positive phase angle indicates that the structure is absorbing energy, an unstable system. Conversely, a negative phase angle will dampen the vibration. A way of visualizing this is the following; if the blade velocity and force is plotted together (recall the integrand in equation (10)), the areas with equal sign of the two functions will contribute to instability. This is shown in figure 1, where the forcing function lags the vibration by $\Delta\varphi = -0.5$. Both the force and blade velocity are scaled to unity amplitude. As the negative area is largest, there is a net energy loss in the blade, and the vibration is damped. Damping is expected in all the simulation in this article, however a difference in phase angle may provide insight into the damping phenomena.

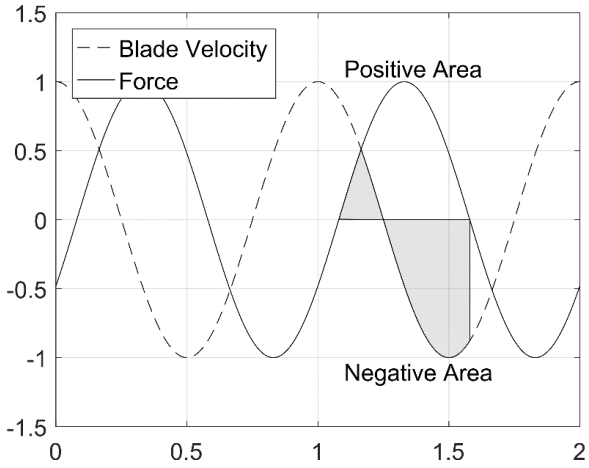

Figure 1. Illustration of phase shift between load and response.

2.2. Experimental setup

The Waterpower Laboratory at The Norwegian University of Science and Technology (NTNU) have performed experiments on both an unsymmetrical hydrofoil (to resemble a Francis turbine blade), and a symmetric hydrofoil. The experimental setup and results from the unsymmetrical test can be found in [12]. The same setup is used for the symmetric hydrofoil tested in this article, some details will be included here.

A symmetric aluminium hydrofoil was excited by electric muscles (Piezoelectric Macrofiber composite actuators from PI Cermaic) to vibrate in a harmonic motion. The hydrofoil was mounted in a stiff 150 mm x 150 mm steel test section, as a part of a longer experimental ⌀ 300 mm pipe system. Several Plexi glass windows were inserted to provide visual access to the blade. Strain gauges and Laser Doppler Vibrometry was used to measure the trailing edge motion. The frequency response was obtained for several different flow velocities and used to calculate the damping characteristics of the system.

Interested readers can find more details in reference [12]. Figure 2 shows a cross-section of the test section, including the placement of the Piezo patches on the aluminum blade. Some global blade dimensions are also included.

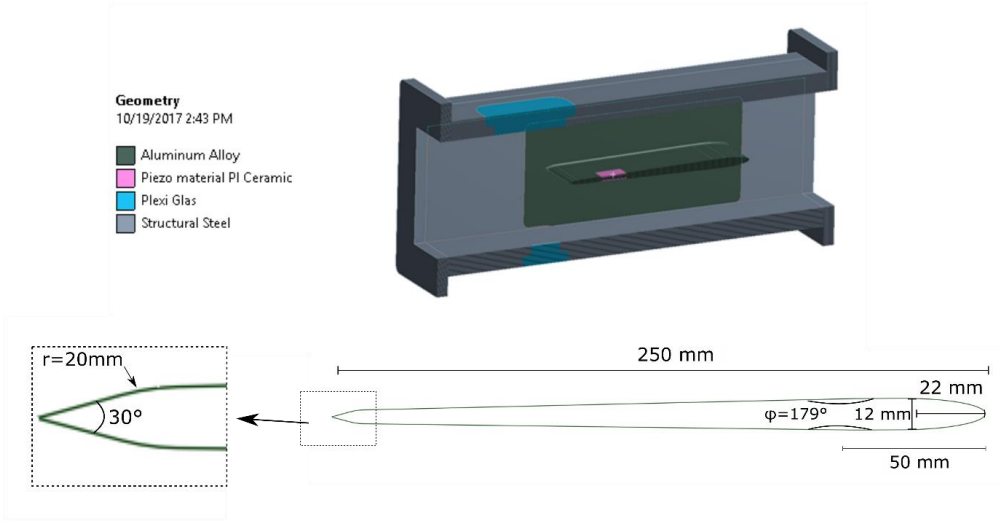

Figure 2. Test section and blade geometry.

2.3. Numerical setup

The work presented in this article tries to replicate the damping characteristics of the symmetric hydrofoil tested at NTNU. Table 1 lists a summary of the most important simulation settings used in this article. The 3 - dimensional numerical domain replicating the experimental rig is shown in figure 3. To ensure that the flow was fully developed before entering the measurement section, the inlet of the domain was extended such that a common entrance length criterion, $> 10D_h$ [16], was satisfied by a large margin. Fully developed flow was verified by testing the inlet turbulence intensity from $0 - 10\%$, with no difference in the levels at the blade. Similarly, the domain was extended downstream to avoid outlet conditions affecting the simulations, and to avoid backflow at the outlet, as the test section is diverging after the blade.

Table 1. Numerical setup.

Software	ANSYS CFX
Turbulence model	$k - \omega$ *SST*
Timestep	7.75e-6 [s] (256 timesteps per period)
Mesh	$5 \cdot 10^6$ elements, all Hexahedral
Deflection amplitude	[2.5, 0.31, 0.05] [mm]
Vibrational frequency	504.37 [Hz]
Boundary conditions	Pressure inlet, mass flow outlet
Flow velocity	2.5 m/s – 45 m/s

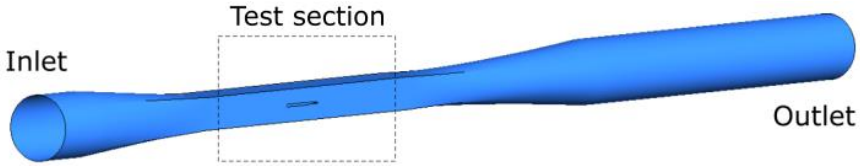

Figure 3. Numerical flow domain.

A one-way coupling was used to obtain the damping. In this case, this means that the structural mode and corresponding natural frequency is calculated in advance. The CFD simulation is then performed with a pre-determined vibrating blade. Constant deflection amplitude is not possible in the experiments, but under the assumption that the damping is primarily dependent on the flow velocity, then it is a reasonable simplification in the numerics. ANSYS CFX was used in the simulations. A specified mass flow was prescribed at the outlet, a zero relative pressure condition at the inlet. The usual no slip condition was prescribed at all walls, and mesh motion forced on the blade surface. A modal analysis was performed in ANSYS Mechanical using the same geometry, with acoustic elements to account for the added mass and stiffness of the water. The first bending mode of the blade corresponds to bending of the trailing edge, and small deflection elsewhere. In a Francis turbine, this is the blade bending mode of interest. This mode shape and corresponding natural frequency was extracted and applied to the blade in CFX. In the simulations, the maximal deflection amplitude was prescribed in advance. The amplitude ranged from 1% to 0.02% of the cord length, i.e 2.5 mm - 0.05 mm as the chord length was 250 mm. A wide range of flow velocities was used, v = [2.5 m/s - 45 m/s] to identify any trends. The hydrodynamic damping was calculated by combining and discretizing equations (7) - (8), meaning that a normalized work was calculated for each timestep and summed over a full vibrational period, see equation (12). Every vibrational period was divided into 256 timesteps. To minimize the effect of the transient start-up on the damping, equation 12 was applied on a periodic solution.

$$\xi = \sum_{k=1}^{256} \frac{-\int_A p \cdot \dot{u}_n dA}{2\pi M \omega^2 q_0^2} \Delta t \tag{12}$$

The mesh consists of hex elements only, created in ANSYS ICEM CFD. The total number of elements was about 5 million, where the damping was found to be independent of element number. Figure 4 shows the mesh in the midplane around the blade, and the same mesh was used in all simulations. The Courant number ($C = u_{local}\Delta t \Delta x^{-1}$) and the y^+ values did therefore change as the free stream velocity was changed, however simulations at v = 30 m/s showed satisfactory values ($C_{rms} = 0.31, y^+_{max} = 2.3$). At the trailing edge, where separation occurs, the y^+ value was well below 1, and verifies the use of the k − ω SST turbulence model [17]. In the mentioned Courant number, u_{local} denotes the local flow velocity, Δt the timestep, and Δx the mesh size. In an explicit solver, this number should be < 1, however this is not necessary in the implicit CFX solver [18].

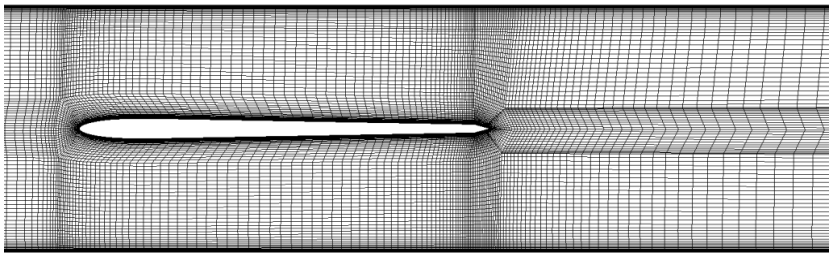

Figure 4. Cross - sectional view of mesh around blade.

3. Results

Figure 5 shows the damping ratio with respect to the flow velocity at three different, fixed amplitudes, $[A_1, A_2, A_3] = [2.5, 0.31, 0.05]$ [mm]. The amplitudes are far apart, $A_1/A_2 = 8$ and $A_2/A_3 = 6.2$, however an almost identical behaviour is seen in the simulations using A_2 and A_3. This may indicate that there exists a range of deflections where the hydrodynamic damping factor is independent of the deflection amplitude.

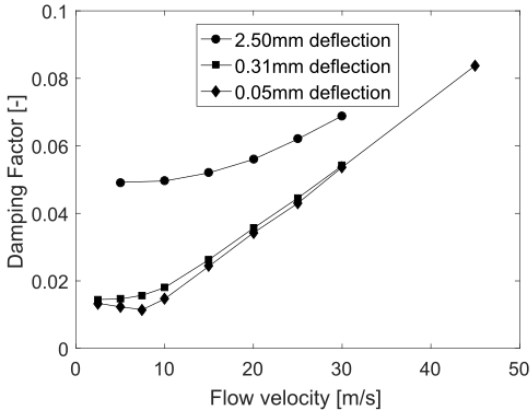

Figure 5. Effect of pre – determined deflection amplitude.

The dependency on the flow velocity however, is not constant or even linear in the whole range. There seems to exist two regions of linear behavior, with different slope. This is supported by experimental results, shown in figure 6. The experimental results are plotted along with an error bar of two standard deviations, and for flow velocities above v = 10 m/s, there is a great match between the experiments and simulations. The large uncertainty at v = 28 m/s in the experiments is due to the onset of cavitation at higher flow velocities. In the experiments, the threshold of v ≈ 6 m/s, marked the lock-in region. Lock-in is the phenomena when the shedding frequency in the flow locks with the natural frequency of the structure over a range of flow velocities, instead of linearly increasing as is reported by i.e. Brekke [19]. A narrow band included in figure 6 for visualization of this region.

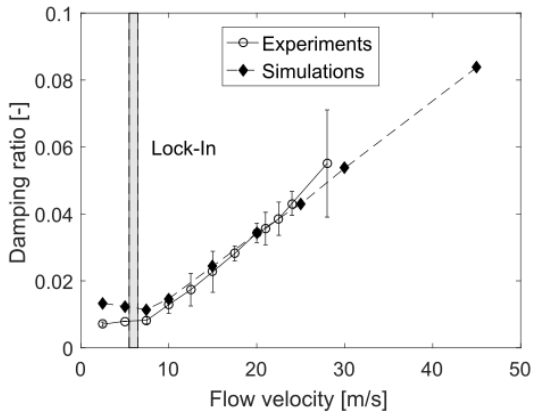

Figure 6. Numerical and experimental damping characteristics.

4. Discussion

Figure 5 indicates that there exists an amplitude range where the damping is independent of the deflection. Moreover, if this range includes the value 0.31 mm, which compared to the blade size is probably unrealistically high, then it can be assumed that the damping is deflection - independent in the whole normal operation range of the turbine. The damping is therefore only a function of the flow velocity, a massive simplification of the system. Similar experiences are seen in the gas turbine industry, however at larger deflections [20]. This result is also supporting the initial assumption of doing a one-way coupled fluid - structure simulation. The second interesting finding is the different damping regions found in figure 6. It is clear that the damping characteristics before and after the lock-in region is different. It should be noted that the simulated and experimental data may not be compared directly, as the deflection amplitude is fixed in the simulations. This is not possible in the experiments. If, however, the assumption of amplitude-independent damping is true, then a comparison could be performed without introducing much error. The phase difference between forcing and vibration, as reviewed in section 2.1.1, is extracted to investigate the damping behaviour more thoroughly by equation (9). Figure 7 (a) shows the phase difference as a function of the flow velocity. The phase difference is obtained by scaling the force on the blade (lift) to unity amplitude and comparing it with the forced vibration (sinusoidal function). The phase is then the spatial difference between the intersection with the x-axis, see small figure in figure 7 (a) or section 2.1.1.

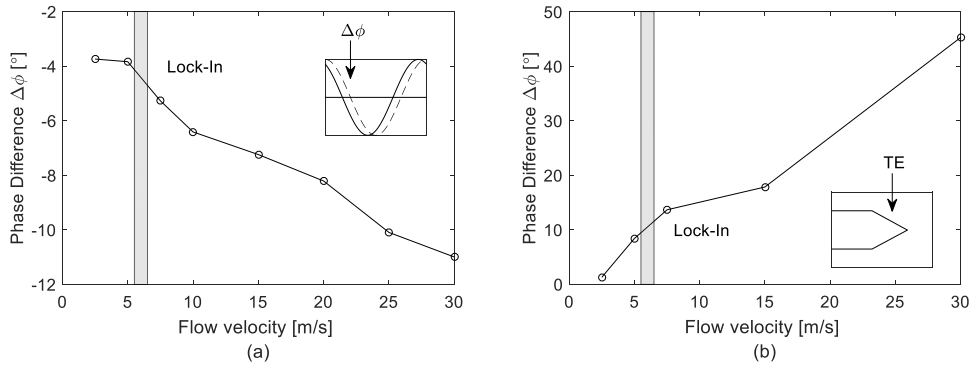

Figure 7. (a) Phase shift, lift whole blade, (b) Phase shift, lift trailing edge only.

We see a change in behaviour before and after the lock-in region here as well, however not as clear as in figure 6. Note that the phase difference is negative for all flow velocities. This indicates that the blade is damped, regardless of flow. An assumption in the derivation of equation (9), is that the velocity of the blade and the pressure on the blade is independent of the location on the hydrofoil. This assumption may not be valid for the mode shape we are studying in this article. To illustrate this, the phase difference using only the lift at the trailing edge (TE in small figure 7 (b)) is extracted and plotted in figure 7 (b). We see that the trailing edge part of the hydrofoil contributes to an unsteady (positive $\Delta\phi$) hydrofoil vibration, although the trend across lock-in is inconclusive.

Looking more closely at the two regions with different damping behaviour. The integrand in the work integral, $(p \cdot \dot{u}_n)$, is composed of two parts. The normal velocity of the blade surface is equal in all simulations, and the pressure is therefore the dimensioning quantity in the integral. The forcing at the trailing edge of the blade is primarily the shedding of vortices. Bergan et al. [12] includes an analytical derivation of the phase shift in the shedding frequency across lock - in, and explains how this may increase the damping at high flow velocities. As was seen in figure 7 (b) the forcing at the trailing edge only was unstable, which actually contradicts this theory. Figure 7 (b) does not indicate that the shedding will dampen the vibration, rather the opposite. However, the assumptions used in deriving equation (9) may be too uncertain to draw any conclusions. Additionally, other factors may dominate the trailing edge shedding, i.e. the development of the pressure field when both the frequency and amplitude is pre-determined in the simulations. A time-consuming two-way coupled simulation may provide further insight. The reason why the damping characteristics changes across the lock-in region is not yet found.

One of the objectives of this numerical and experimental work is to obtain the damping at prototype flow velocities. In a Francis turbine, the relative velocity of the water may easily exceed $v > 40$ m/s. Due to the location of the test rig and the capacity of the pump, the fluid velocity in the experiments was limited to $v \approx 28$ m/s before cavitation occurred. A simulation was therefore run at $v = 45$ m/s, seen in figure 6. We clearly see that the linear trend after the lock-in region is valid even for higher flow velocities. It is therefore reasonable to assume that one can extrapolate the experimental data to higher flow rates.

5. Conclusion

This article shows that a numerical estimation of the hydrodynamic damping of a vibrating hydrofoil is possible. The correspondence with experimental results are very good, especially above the lock-in region. Below this region, the trend is similar, however the absolute values differ somewhat. Two damping regimes are identified; roughly constant before and linearly increasing after the lock-in region. The complete explanation of this phenomena is not known. The hydrodynamic damping is fairly low, $\xi < 0.1$, even for flow velocities realistic to Francis turbines. A one way-coupled simulation was performed, and the vibration amplitude is therefore chosen in advance. This assumption is supported by the result that the damping characteristics are independent of the deflection amplitude, as long as the deflections are small. For larger deflection, a two-way coupling is probably needed.

6. Further Work

The overall goal of the research project is to understand the failure phenomenon in Francis turbines. A key difference from the present geometry and a turbine is the number of blades. In a full turbine, a phase difference in the vibration of two neighboring blades may facilitate negative damping. Therefore, the next iteration of the current study will include several blades to investigate this effect, and increase the similarity to an actual turbine.

Acknowledgments
This work is part of the HiFrancis research project, with financial support from the Research Council of Norway. This support made this work possible.

References

[1] Kobro E 2010 *Measurement of Pressure Pulsations in Francis Turbines* Ph.D. thesis Norwegian University of Science and Technology (http://hdl.handle.net/11250/234140)
[2] Liu X, Luo Y and Wang Z 2016 *Renewable and Sustainable Energy Reviews* **54** 1–14
[3] Seidel U, Hübner B, Löfflad J and Faigle P 2012 *IOP Conf. Series: Earth and Environmental. Science* **15** 052010 ISSN 1755-1315
[4] Dorfler P, Sick M and Coutu A 2012 *Flow-induced pulsation and vibration in hydroelectric machinery* (Springer Science & Business Media)
[5] Liang Q W, Rodrguez C G, Egusquiza E, Escaler X, Farhat M and Avellan F 2007 *Computers & Fluids* **36** 1106–1118 ISSN 0045-7930
[6] Tanaka H 2011 *Int. J. of Fluid Machinery and Systems* **4** 289–306
[7] Coutu A, Seeley C, Monette C, Nennemann B and Marmont H 2012 *IOP Conf. Series: Earth and Environmental. Science* **15** 062060 ISSN 1755-1315
[8] Kaminer A A and Kavitskii B M 1976 *Strength of Materials* **8** 25–27
[9] Roth S, Calmon M, Farhat M, Mnch C, Bjoern H and Avellan F 2009 *Proc. of the 3rd IAHR Int. Meeting of the Workgroup on Cavitation and Dynamic Problems in Hydraulic Machinery and Systems* **1** 253–260
[10] Monette C, Nennemann B, Seeley C, Coutu A and Marmont H 2014 *IOP Conf. Series: Earth and Environmental. Science* **22** 032044 ISSN 1755-1315
[11] Liaghat T, Guibault F, Allenbach L and Nennemann B 2014 *ASME 2014 Int. Mech. Eng. Congress and Exposition* pp V04AT04A073–V04AT04A073
[12] Bergan C W, Solemslie B W, Østby P and Dahlhaug O G 2018 *Int. J. of Fluid Machinery and Systems* **11** 146–153
[13] Craig R R and Kurdila A J 2006 *Fundamentals of structural dynamics* (John Wiley & Sons)
[14] Seeley C 2013 *54th AIAA/ASME/ASCE/AHS/ASC Structures, Structural Dynamics, and Materials Conference* p 1910
[15] ANSYS 2013 *CFX-solver modeling guide* (ANSYS inc)
[16] Yunus A C and Cimbala J M 2006 *Fluid mechanics fundamentals and applications* (McGraw Hill Publication)
[17] Menter F R 1994 *AIAA journal* **32** 1598–1605
[18] Ferziger J H and Peric M 2012 *Computational methods for fluid dynamics* (Springer Science & Business Media)
[19] Brekke H 1994 *Proc. of the 17th IAHR Symp., Beijing, China* pp 15–19
[20] Giersch T, Hnisch P, Beirow B and Khhorn A 2013 *J. of Turbomachinery* **135** 031034

Paper 8

Damping Measurements on a Multi-Blade Cascade with Multiple Degrees of Freedom: a Francis-99 Test Case

Bergan, C. W., Tengs, E. O., Solemslie, B. W., Østby, P., Dahlhaug, O. G.

Submitted to IOP Conference Series: Journal of Physics 2019

This paper is awaiting publication and is not included in NTNU Open